

# Measurement Methods for Investigating the Air Return Ratio of Open Volumetric Receivers at Solar Power Towers

## Messverfahren zur Untersuchung der Luftrückführtrate an offenen volumetrischen Receivern von Solarturmanlagen

Von der Fakultät für  
Maschinenwesen der Rheinisch-Westfälischen Technischen Hochschule Aachen

zur Erlangung des  
akademischen Grades eines Doktors der Ingenieurwissenschaften genehmigte  
Dissertation

vorgelegt von

Arne Tidde Tiddens

Berichter:

Univ.-Prof. Dr.-Ing. Bernhard Hoffschmidt

Univ.-Prof. Dr. rer. nat. Andreas Kemna

Tag der mündlichen Prüfung: 5. Mai 2017

Diese Dissertation ist auf den Internetseiten der Universitätsbibliothek online verfügbar.



---

# Kurzfassung

Kostenreduzierung spielt bei der konzentrierenden Solarthermie eine maßgebliche Rolle. Daher ist es essentiell, alle Faktoren, die den Systemwirkungsgrad einer Solarturmanlage beeinflussen, zu quantifizieren. Die Luftrückführrate ist ein Schlüsselfaktor des offenen volumetrischen Solarreceivers, welche das Verhältnis von zurückgeführter Luft zu eingesaugter Luft beschreibt. Um einen hohen Receiverwirkungsgrad zu erreichen, ist es wichtig, die Luftrückführrate zu erhöhen. Viele Parameter, wie z. B. die Windgeschwindigkeit und -richtung, die Geometrie des Receivers sowie die Betriebsweise, haben einen Einfluss auf die Strömung vor dem Receiver und somit auch auf die Luftrückführrate. Daher ist es essentiell, die Luftrückführrate messtechnisch zu quantifizieren und die Strömung vor dem Receiver zu visualisieren. Bislang wurde dies weder auf einem industriellen Maßstab noch unter dem Einfluss von konzentrierter Solarstrahlung umgesetzt.

Die Entwicklung eines Messverfahrens zur Quantifizierung der Luftrückführrate mit möglichst hoher Präzision stellt den Kern dieser Arbeit dar. Weiterhin wurde erstmalig die Rückführluft vor dem Receiver visualisiert. Diese erlaubt ein besseres Verständnis der auftretenden Strömungsphänomene, welche maßgeblich die Luftrückführung bestimmen. Messverfahren, die dies ermöglichen, wurden in dieser Arbeit im Labormaßstab entwickelt, unter Betriebsbedingungen erprobt und erfolgreich am Solarturm Jülich angewandt.

Um die Luftrückführrate quantitativ zu bestimmen, wurden drei Varianten eines neuartigen, zirkulären Indikatorgasverfahrens entwickelt. Das Indikatorgas wurde hierbei entweder kontinuierlich oder intermittierend dem offenen Luftkreislauf hinzugefügt und über die unvollständige Luftrückführung verdünnt. Der Stoffmengenanteil des zugeführten Edelgases Helium wurde mittels eines Massenspektrometers im Luftkreislauf bestimmt und daraus die Luftrückführrate berechnet. Eine zeitliche Auflösung von 0.5 s wurde erreicht. Eine maximale Luftrückführrate von  $(68.6 \pm 0.7)\%$  mit 95% Konfidenzintervall wurde unter Bestrahlung mit konzentrierter Solarstrahlung am Versuchskraftwerk Jülich gemessen. Dieser Wert ist höher als die bisher angenommene Luftrückführrate von 60%. Dieser Unterschied in der Luftrückführrate entspricht einem 4 – 5% höherem Gesamtsystemwirkungsgrad. Die Visualisierung der Rückführluft wurde erstmalig mit einer zu diesem Zweck entwickelten Induzierten Infrarot Thermographie erzielt. Hierbei wurde die Rückführluft mit Kohlenstoffdioxid angereichert und somit eine erhöhte Strahlung im infraroten Wellenlängenbereich induziert. Die von der Rückführluft abgegebenen Strahlung konnte mittels einer Infrarotkamera visualisiert werden.

# Abstract

Cost reduction plays a significant role in the field of concentrated solar thermal energy. It is therefore essential to quantify all factors that influence the energy conversion efficiency. The air return ratio is a key factor for the overall efficiency of the open volumetric receiver. It is the fraction of the blown out air which is sucked in again through the solar receiver. To achieve a high receiver efficiency it is therefore important to increase the air return ratio. Many variables such as wind speed and direction, geometry of the receiver design and operational mode influence the air flow in front of the receiver. This in turn influences the air return ratio. It is therefore of vital importance to be able to measure the air return ratio and furthermore visualize the air flow in front of the receiver. The air return value was prior to this work unknown on a large scale and under concentrated solar irradiation.

The development of a measurement technique for the quantification of the air return ratio with maximum accuracy is the main objective of this thesis. The second objective lies in the visualization of the returned air. This improves the understanding of the occurring flow phenomena which govern the air return ratio. The measurement methods were developed at a lab scale, tested under operating conditions and successfully demonstrated at the solar tower Jülich.

In order to measure the air return ratio, three variants of a novel circular tracer gas measurement technique have been developed. The tracer gas is injected either continuously or intermittently into the open air system. The tracer gas is diluted by the imperfect air return ratio. The mole fraction of the injected noble gas helium is measured with a mass spectrometer within the air system, from which the air return ratio is determined. A temporal resolution of 0.5 s has been achieved. A maximal air return ratio of  $(68.6 \pm 0.7) \%$  with 95 % confidence interval has been measured during irradiation with concentrated sunlight at the solar tower power plant Jülich. This is higher than the previously assumed air return ratio of 60 %. This difference corresponds to a 4 – 5 % higher overall system efficiency. The return air in front of the receiver was visualized for the first time with the newly developed Induced Infrared Thermography. Hereby, carbon dioxide is added to the return air. This induces a larger amount of radiation being given off in the infrared region. This radiation from the return air is visualized using an infrared camera.

# Contents

<b>1</b>	<b>Motivation and Background</b>	<b>1</b>
1.1	Introduction . . . . .	1
1.2	State of the Art . . . . .	5
1.2.1	Air Return Ratio Measurement . . . . .	5
1.2.2	Computational Fluid Dynamics Simulation . . . . .	8
1.2.3	Tracer Gas Measurement . . . . .	12
1.2.4	Return Air Visualization . . . . .	12
1.2.5	Infrared Thermography of Gases . . . . .	13
1.3	Outlining the Research . . . . .	15
<b>2</b>	<b>Theory</b>	<b>19</b>
2.1	Theory of Air Return Ratio Measurement . . . . .	19
2.1.1	Tracer Gas Method for ARR Measurements . . . . .	19
2.1.2	Static ARR Measurement . . . . .	22
2.1.3	Dynamic ARR Measurement . . . . .	24
2.1.4	Numeric ARR Measurement . . . . .	36
2.1.5	Signal Processing . . . . .	38
2.2	Uncertainty Analysis of ARR Measurements . . . . .	39
2.2.1	Uncertainty Estimation . . . . .	39
2.2.2	Sensitivity Analysis . . . . .	41
2.3	Theory of Return Air Visualization . . . . .	42
2.3.1	Choice of Gas for Induced Infrared Thermography (IIT) . . . . .	42
2.3.2	Signal Processing for Induced Infrared Thermography (IIT) . . . . .	45
2.3.3	Infrared Image Velocimetry (IRIV) . . . . .	50
<b>3</b>	<b>Setup</b>	<b>55</b>
3.1	Receiver Model . . . . .	55
3.2	Solar Tower Juelich . . . . .	57
3.2.1	Research Platform . . . . .	58

---

3.2.2	Main Receiver, Power Block and Storage . . . . .	60
<b>4</b>	<b>Results</b>	<b>67</b>
4.1	Static ARR Measurements . . . . .	67
4.1.1	Static Measurements at the Receiver Model . . . . .	67
4.1.2	Static Measurements at the Solar Tower Juelich . . . . .	71
4.2	Dynamic ARR Measurements . . . . .	72
4.2.1	Dynamic Measurements at the Receiver Model . . . . .	72
4.2.2	Validation of the Dynamic and the Static Method . . . . .	75
4.2.3	Dynamic Measurements at the Solar Tower Juelich . . . . .	77
4.3	Numeric ARR Measurements . . . . .	83
4.3.1	Validation of the Numeric with the Dynamic Method . . . . .	84
4.3.2	Measurements at the Solar Tower Juelich . . . . .	85
4.4	Return Air Visualization . . . . .	88
4.4.1	Visualizations at the Testreceiver . . . . .	88
4.4.2	Visualizations at the Main Receiver . . . . .	92
<b>5</b>	<b>Discussion</b>	<b>95</b>
5.1	ARR Measurement Methods . . . . .	95
5.2	ARR Measurements at the Solar Tower Juelich . . . . .	98
5.3	Influence of Wind on the ARR . . . . .	98
5.4	Flow Field in Front of the Receivers . . . . .	100
5.5	ARR Measurements of the Partial and External Air Return Mechanism	101
5.6	Improvements of the Open Volumetric Receiver Concept . . . . .	102
<b>6</b>	<b>Conclusions</b>	<b>103</b>
<b>7</b>	<b>Outlook</b>	<b>107</b>
	<b>Bibliography</b>	<b>109</b>
	<b>Acknowledgment</b>	<b>116</b>
	<b>Nomenclature</b>	<b>119</b>
	<b>Acronyms</b>	<b>121</b>
	<b>List of Figures</b>	<b>123</b>

# 1 Motivation and Background

## 1.1 Introduction

The United Nations open working group for Sustainable Development Goals has identified the goal to "ensure access to affordable, reliable sustainable energy for all" as well as to "take urgent action to combat climate change and its impacts" as two of the main goals of humanity (Griggs et al., 2013; Rifkin, 2014). A resulting increase in percentage of renewable energies within the energy mix leads to a growing dependency of the electricity markets on fluctuating electricity sources. These sources consist mainly of electricity generated by wind and photovoltaics. A stable renewable electricity generation gains in importance in this scenario, especially since storing electricity is not sufficiently cheap to counteract the longterm fluctuation of the electricity supply-demand deficit (Erlach et al., 2015). Two further needs are the supply of cheap renewable process heat for industry and the production of sustainable fuels (Centi et al., 2013). The latter is so far only fulfilled by biofuel production. Boosting biofuel crop production could however threaten food security (Pimentel et al., 2008; Yang et al., 2009).

All these needs can be addressed with concentrated solar power, since it provides an environmentally friendly and virtually unlimited source of high-temperature heat (Romero and Steinfeld, 2012). This heat can be further converted into electricity, stored or used as process heat for industrial processes for example to produce solar fuels. The fact, that it can be stored in the form of heat, allows concentrated solar power to be considered a stable renewable energy source.

The heat is generated by concentrating the sunlight onto a solar receiver where the radiant energy is absorbed and transformed into thermal energy. This energy can be transported using various heat transfer fluids and can be stored until use. Concentrated solar power systems can be divided into groups according to their concentration method. The sunlight can either be concentrated onto a linear absorber, or in central receiver

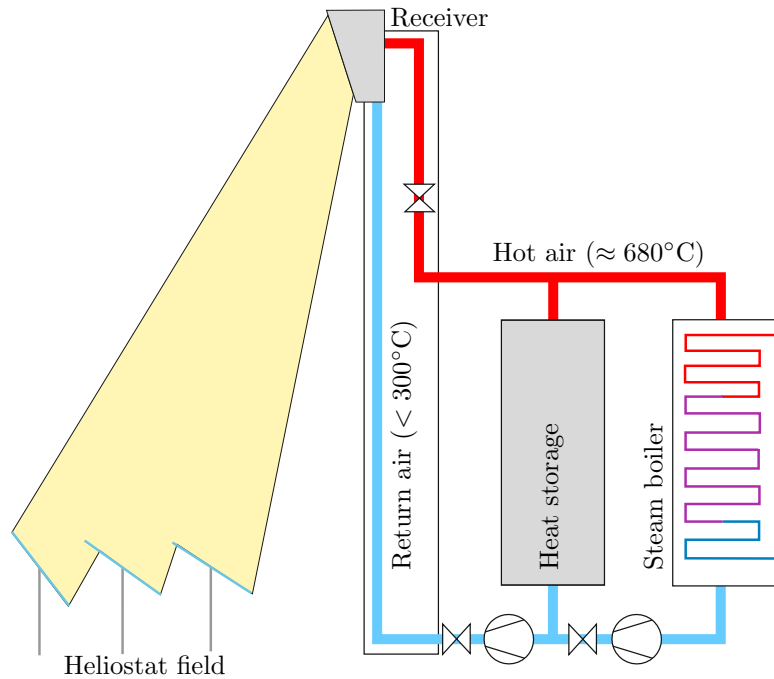


Figure 1.1: Schematic of the STJ. The receiver is heated by a field of heliostats. Air is sucked through the receiver, heating up to about  $680^{\circ}\text{C}$  and used to drive a water steam cycle or is stored in a thermal storage. The still warm air ( $< 300^{\circ}\text{C}$ ) is returned to the receiver for efficiency purposes. Based on Funken (2013).

systems it can be bundled in a focal point on an absorber plane. This allows an even higher concentration of sunlight. Although parabolic through systems are by far the most mature technology with over two decades in established commercial projects, central receiver systems have a high potential due to an increase in the achieved temperature (Romero and Steinfeld, 2012). Additionally, central receiver plants are the most resource-efficient ones. Their consumption of abiotic materials is only half that of parabolic trough plants (Samus et al., 2013). Typical thermal fluids used in the receiver are saturated or superheated steam and nitrate-based molten salts. Air is used in receiver concepts based on volumetric absorption of directly irradiated porous structures, which promise more efficient solar energy capture and conversion. (Romero and Steinfeld, 2012)

The concept is implemented at the solar tower Juelich (STJ) in 2008, which shown in Fig.1.1 and is described more detail in Section 3.2. Hereby a field of 2153 heliostats reflect and concentrate the sunlight onto an open volumetric receiver at the top of the 60 meter high solar tower power plant. The receiver consists of a porous ceramic structure



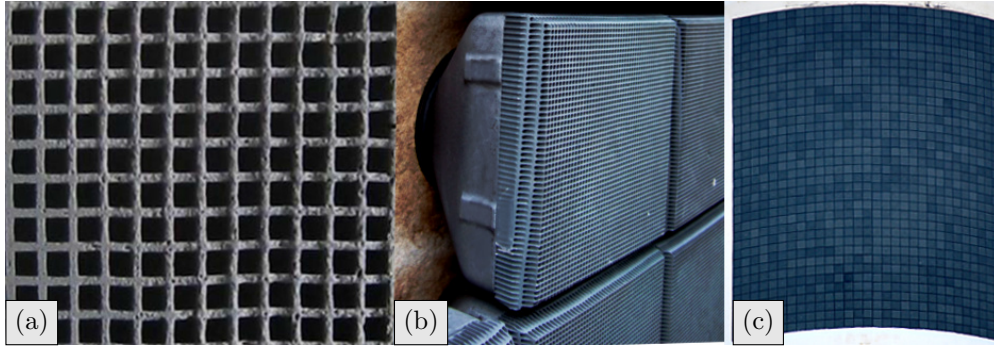


Figure 1.2: Photos of the receiver of the solar tower Juelich, showing its modularity. (a) shows a close up of the absorber structure of the Hitrec-II absorber module, (b) individual absorber modules during maintenance which make up the main receiver of the solar tower Juelich (c). Based on Tiddens et al. (2017b).

of modular design to allow for scalability. It comprises of 1080 absorber modules (see Fig. 1.2b) which are grouped into so-called subreceivers, which in turn make up the receiver (see Fig. 1.2c). The receiver is heated by absorbing the sunlight, creating surface temperatures of up to  $1000^{\circ}\text{C}$  (Andlauer, 2015). Air is sucked through the absorber modules to transfer the thermal energy to a heat exchanger or storage unit. Due to the low heat capacity of air, high air mass flows are required.

The fraction of the blown out air which is sucked in again, is called the substantial air return ratio (ARR). It is defined by Ahlbrink et al. (2013) as

$$ARR = \frac{\dot{m}_{\text{return}}}{\dot{m}_{\text{out}}} \quad (1.1)$$

whereby  $\dot{m}_{\text{out}}$  is the air mass flow leaving the receiver towards the ambient, and  $\dot{m}_{\text{return}}$  is the part of this air which is sucked in again into the air circuit. Additionally to the substantial ARR a thermal ARR can be defined according to Maldonado Quinto (2016) at the receiver surface as

$$ARR_{\text{thermal}} = \frac{\dot{m}_{\text{in,rec}} \cdot (h_{\text{in,rec}} - h_{\text{amb}})}{\dot{m}_{\text{out,rec}} \cdot (h_{\text{out,rec}} - h_{\text{amb}})}, \quad (1.2)$$

with the specific enthalpy for the blown out air  $h_{\text{out,rec}}$ , the sucked in air  $h_{\text{in,rec}}$  and the ambient air  $h_{\text{amb}}$ . A schematic of the air flow within the receiver is shown in Fig. 1.3. The points at which the above used enthalpies are defined, are indicated. All the mass flows and specific enthalpies in Eq. 1.2 are defined at the surface of the receiver. The reason of defining  $ARR_{\text{thermal}}$  is to use it for the calculation of the overall efficiency of

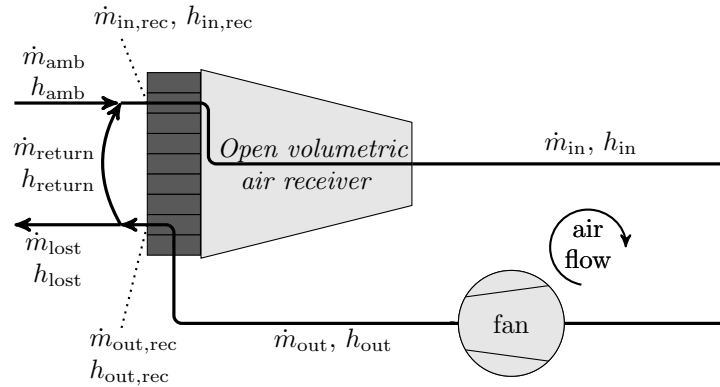


Figure 1.3: A schematic of the air flow of the open volumetric receiver is shown. The air mass flows  $\dot{m}$  and specific enthalpies  $h$  are indicated. Based on Tiddens et al. (2016b).

the power plant. Neglecting the minor losses of the return air enthalpy due to conduction and gas emission of air, the thermal ARR turns into the substantial ARR (Eq. 1.1) which is measured within this thesis. (Maldonado Quinto, 2016)

To achieve a high receiver efficiency it is important to increase the ARR and therefore minimize the occurring leak in the air circuit. This can be seen in Fig. 1.4, where the normalized system efficiency is shown for different ARRs as well as return air temperatures. The system efficiency is hereby the product of the efficiency of the open volumetric receiver and the power plant efficiency. With increasing air return temperature the power plant efficiency increases and the open volumetric receiver efficiency decreases. Therefore a system efficiency optimum can be found depending on the ARR, which is indicated in red. The receiver output temperature was chosen to be  $650\text{ }^\circ\text{C}$ . It can be seen that an improvement from  $ARR = 60\%$  to  $ARR = 80\%$  leads to an increase in 8 percentage points of the normalized system efficiency. (Maldonado Quinto, 2016) The ARR depends on many variables such as wind speed and direction, geometry of the receiver design and operational mode. Its value is so far unknown on a large scale and under solar irradiation. Since it can be influenced by a multitude of measures, it is of vital importance to be able to measure it (von Storch et al., 2015; Vogel and Kalb, 2010). To additionally understand the origins of measured variations in the ARR, the flow of the blown out return air in front of the receiver should also be visualized. Measuring the ARR and visualizing the return air is the goal of this thesis (see 1.3).

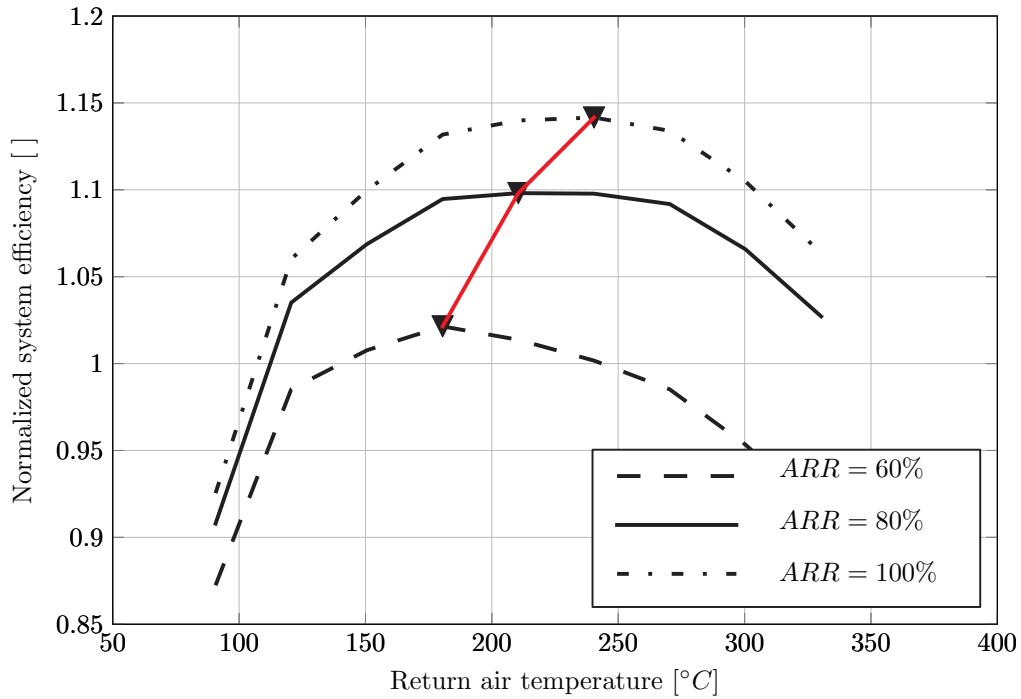


Figure 1.4: The normalized system efficiency for different air return temperatures and ARR is shown. It can be seen that an improvement from  $ARR = 60\%$  to  $ARR = 80\%$  leads to an increase in 8 percentage points of the normalized system efficiency. (Maldonado Quinto, 2016)

## 1.2 State of the Art

### 1.2.1 Air Return Ratio Measurement

An overview on the development of open volumetric receivers and the measured ARR was given by Ávila-Marín (2011). ARR measurements can generally be approached by either measuring at the receiver front, or by measuring within the air system. The different input parameters of the different existing ARR measurements are shown in a schematic of the air flow within the receiver in Fig. 1.5.

The most useful ARR measurement would be the direct measurement of the thermal  $ARR_{\text{thermal}}$  which is defined in Eq. 1.2 as

$$ARR_{\text{thermal}} = \frac{\dot{m}_{\text{in,rec}} \cdot (h_{\text{in,rec}} - h_{\text{amb}})}{\dot{m}_{\text{out,rec}} \cdot (h_{\text{out,rec}} - h_{\text{amb}})}$$

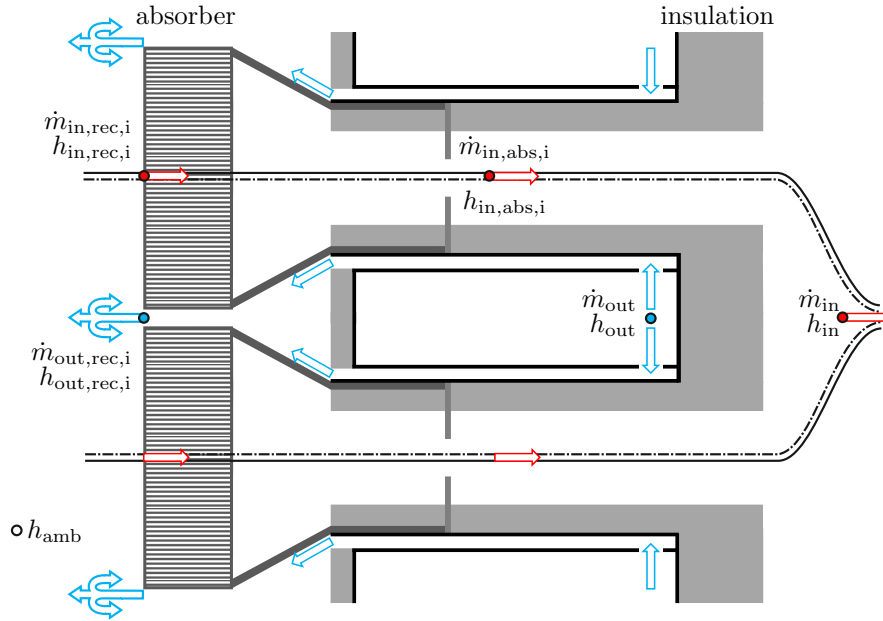


Figure 1.5: A schematic of the air flow within the open volumetric air receiver is shown. Based on Ahlbrink et al. (2013).

To be able to determine  $ARR_{\text{thermal}}$  directly, it would be necessary to measure the flow field of all  $i$  receiver modules in front of the receiver ( $\dot{m}_{out,rec,i}$ ,  $\dot{m}_{in,rec,i}$ ) as well as the temperatures of the air flows at the receiver front to determine  $h_{out,rec,i}$  and  $h_{in,rec,i}$  for all receiver modules.

To measure the air flow field in front of the receiver the measurement technique needs to be applicable with very high precision. However, most flow measurement techniques are not employable on the large-scale of solar tower power plants or do not yield quantitative results. An existing and possibly the most feasible flow measurement technique is the laser based Particle Image Velocimetry (PIV). It would be applicable on such a scale. The resulting measurement uncertainties of the ARR would however be too large, rendering the ARR results useless. A direct ARR measurement on the outside of the receiver is therefore not feasible, since for a measurement of the air flows and their temperature thousands of thermocouples and mass flow measurements would be needed.

A further option would be the measurement of the air mass flows and temperatures within the air circuit, instead of at the receiver front. Under the assumption that  $h_{in,rec} = h_{in}$ ,  $h_{out,rec} = h_{out}$ , a constant specific heat capacity of air and that  $\dot{m}_{in} = \dot{m}_{out}$  Eq. 1.2

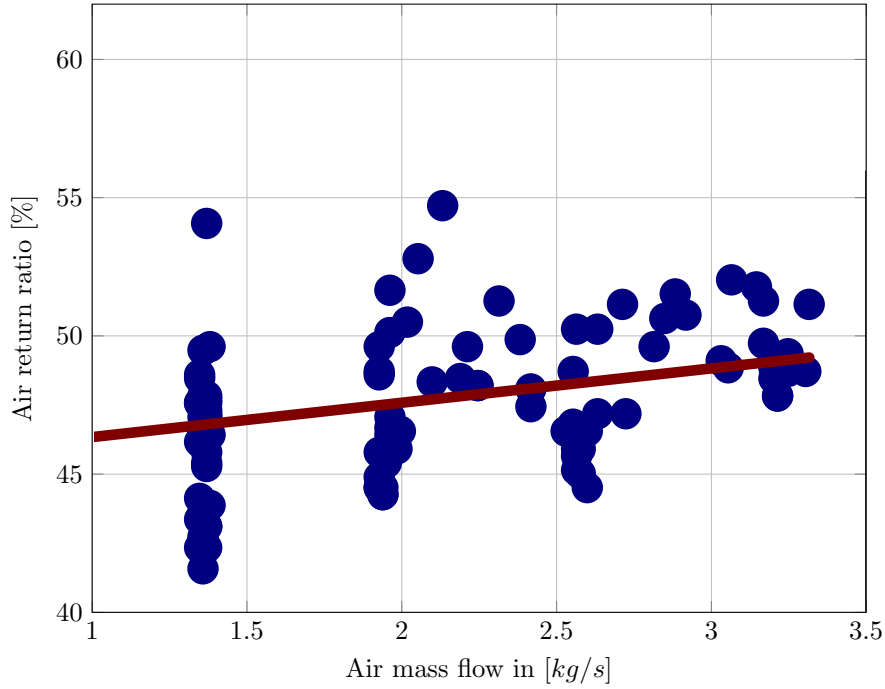


Figure 1.6: Measurements of the ARR at the SOLAIR 3000 receiver. Due to the heat flow between the return air and the outsides of the receiver modules (see Fig. 1.7), these measurements can only be seen as a rough estimate (see Eq. 1.4). (Télez et al., 2004)

would become

$$ARR_{\text{thermal}} = \frac{T_{\text{in,rec}} - T_{\text{amb}}}{T_{\text{out,rec}} - T_{\text{amb}}}, \quad (1.3)$$

which stands in accordance with Hoffschmidt et al. (2003). A corresponding measurement in the airflow before and after the receiver has been conducted by Télez et al. (2004) at the SOLAIR 3000 receiver without solar radiation. The resulting ARR for different air mass flows are shown in Fig. 1.6. This however does not lead to correct results, since  $h_{\text{in,rec},i} \neq h_{\text{in,abs},i} \neq h_{\text{in}}$ , which is caused by heat transfer between the sucked in and blown out air within the receiver shown in Fig. 1.7.

This results in

$$ARR_{\text{thermal}} = \frac{\dot{m}_{\text{in,rec}} \cdot (h_{\text{in,rec}} - h_{\text{amb}})}{\dot{m}_{\text{out,rec}} \cdot (h_{\text{out,rec}} - h_{\text{amb}})} \neq \frac{\dot{m}_{\text{in}} \cdot (h_{\text{in}} - h_{\text{amb}})}{\dot{m}_{\text{out}} \cdot (h_{\text{out}} - h_{\text{amb}})}. \quad (1.4)$$

Therefore all temperature and flow measurements would have to be conducted at the surface of the receiver with a high spatial resolution. Since this is not feasible, direct

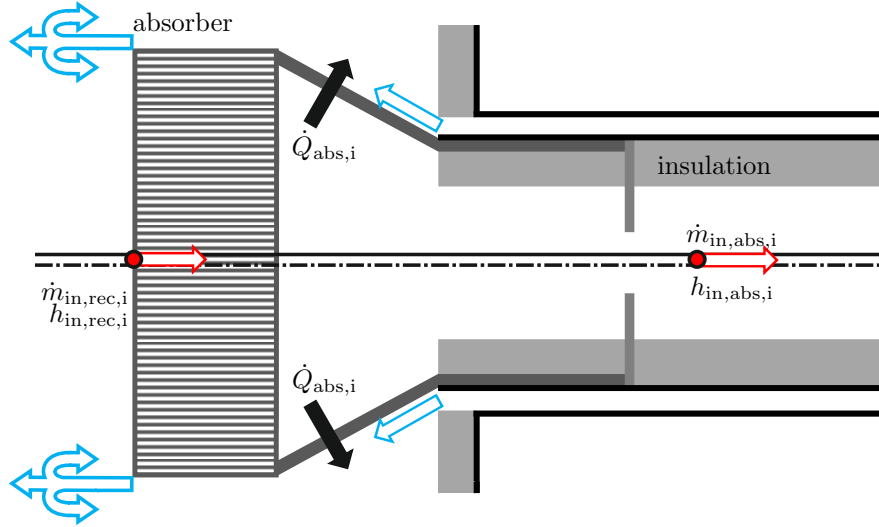


Figure 1.7: A schematic of the air flow within the open volumetric air receiver is shown. The rate of flow of heat  $\dot{Q}_{abs,i}$  between the sucked in and blown out air is indicated. Based on Ahlbrink et al. (2013).

measurements of  $ARR_{thermal}$  are not possible. The heat transfer between the sucked in and blown out air within the receiver becomes even more prominent under irradiation. Téllez et al. (2004) additionally calculate  $h_{in}$  using a weighted average of  $h_{in,abs,i}$  without measuring the air mass flows  $\dot{m}_{in,rec,i}$ . Hence the results shown in Fig. 1.6 are considered to be only a very rough estimate.

Neither a direct  $ARR_{thermal}$  measurement nor a measurement of the substantial ARR (Eq. 1.1), has been covered in literature.

## 1.2.2 Computational Fluid Dynamics Simulation

Due to the lack of reliable reference ARR measurements, computational fluid dynamics (CFD) simulations are the most important reference. CFD simulations have been conducted and validated using PIV for a model containing one absorber module by Maldonado Quinto (2016). Using the developed CFD model, an ARR was calculated for various scenarios. Fig. 1.8 shows the dependence of the ARR on the mass flow of the system. The simulated absorber module is irradiated and considered undisturbed by neighboring models and wind. The remaining simulation boundary conditions are described in (Maldonado Quinto, 2016). It was found that for the examined system of

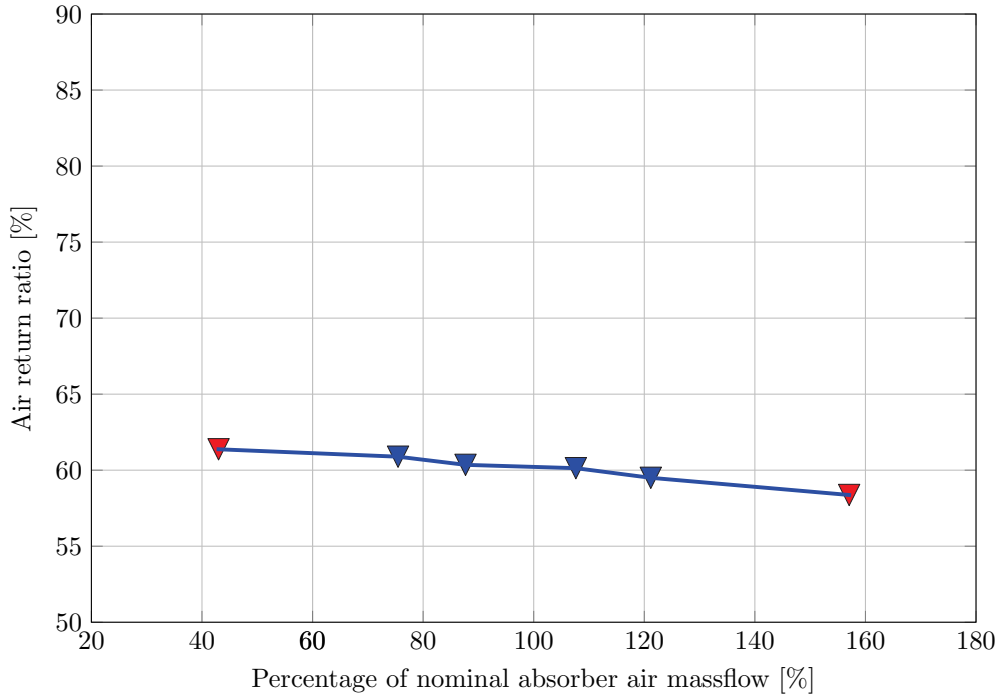


Figure 1.8: Simulated ARR of one absorber module for different percentages of the nominal mass flux. The simulated absorber module is irradiated and considered undisturbed by neighboring models and wind. The ARR decreases only very slightly with increasing mass flow of the system. Maldonado Quinto (2016)

one absorber module the ARR decreases only very slightly with increasing mass flow of the system. The dependence on the temperature in the range from 120 °C to 400 °C was found to be smaller than 1.5 % and lies therefore within the discretization error of the simulation. (Maldonado Quinto, 2016)

A further aspect which is examined is the effect of a partial air return system. Hereby a part of the return air  $\dot{m}_{out}$  is not returned through the structure of the receiver, but is separated ( $\dot{m}_{out} = \dot{m}_{out,main} + \dot{m}_{out,sep}$ ). This separated air ( $\dot{m}_{out,sep}$ ) is then blown away through a vent. The partial air return is hereby defined as the relationship between the air mass flow of the return air and the main air mass flow

$$\Psi = \frac{\dot{m}_{out,main}}{\dot{m}_{out}}. \quad (1.5)$$

A partial air return ( $\Psi < 1$ ) could be favorable, since the power consumption of the fans make up a large part of the parasitic losses in the open volumetric air receiver concept. The cooling of the absorber modules by the return air (see Fig. 1.7) could also

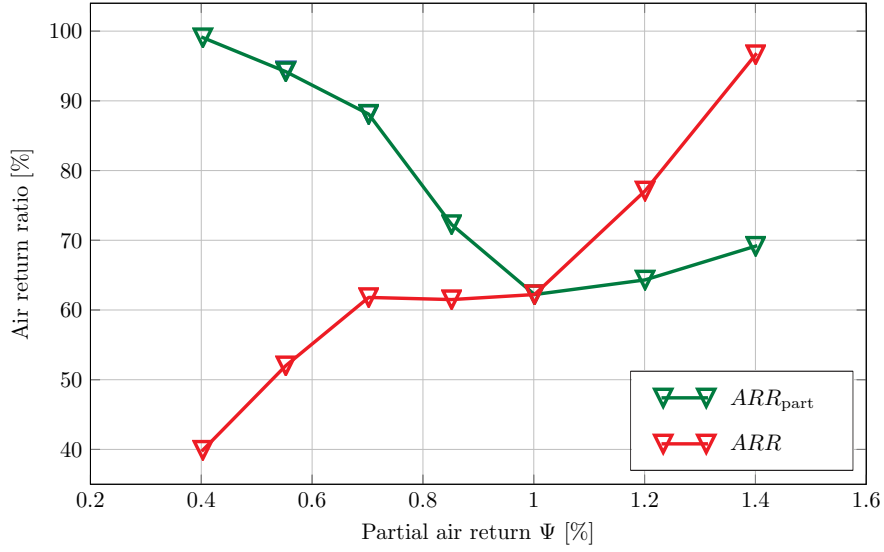


Figure 1.9: The simulated ARR for different percentages of partial air return  $\Psi$  for one absorber module. The partial air return can be greater than one, since it is examined here on an absorber level. The simulations were conducted for one module. Based on Maldonado Quinto (2016).

be reduced to a necessary minimum, since the air mass flow in between the absorber modules is reduced. Fig. 1.9 shows the simulated ARR results of a partial air return mechanism. The green curve shows the ARR of the air which is returned to the receiver, being defined as

$$ARR_{part} = \frac{\dot{m}_{out,main,return}}{\dot{m}_{out,main}}. \quad (1.6)$$

The red curve shows this ARR in respect to the total blow out air mass flow

$$ARR = \frac{\dot{m}_{out,main,return}}{\dot{m}_{out}} = ARR_{part} \cdot \Psi. \quad (1.7)$$

In Fig. 1.9 it can be seen, that the ARR for  $\Psi = 0.7$  is roughly the same as the ARR of  $\Psi = 1$ . Due to the lower parasitic losses a partial air return of  $\Psi = 0.7$  should be preferable if this phenomenon indeed follows this pattern.

An extension to the partial air return is the external air return mechanism. Hereby the fraction of return air which is not blown out in between the absorbers of the receiver ( $\dot{m}_{out,sep}$ ) is brought in front of the receiver from the sides and / or from the bottom of the receiver. A partial and external air return mechanism exist at the STJ, and were examined in respect to the ARR within this thesis.



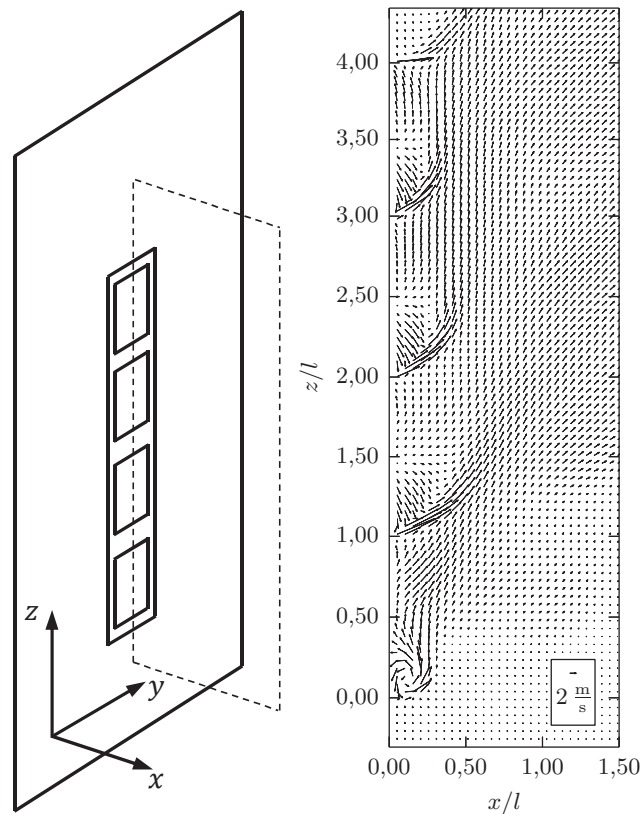


Figure 1.10: The simulated air flow in front of four absorber modules is shown. The axis are hereby normalized by the absorber edge length  $l$ . It can be observed, that for  $x/l > 0,5$  the return air only moves further away from the receiver and upwards. The simulated ARR of the four modules was found to be 58 %, compared to the higher 63 % the for one absorber module. Based on Maldonado Quinto (2016).

To further examine the flow in front of the receiver, a CFD analysis has been conducted by Maldonado Quinto (2016) with four absorber modules. This is shown schematically on the left hand side in Fig. 1.10. The resulting simulated flow at the dashed plane, is shown on the right. It can be observed, that for  $x/l > 0,5$  the return air only moves further away from the receiver and upwards. The simulated ARR of the four modules was found to be 58 %, compared to the higher 63 % the for one absorber module.

### 1.2.3 Tracer Gas Measurement

Due to the previously mentioned difficulties measuring  $ARR_{\text{thermal}}$  a tracer gas method was used to measure the substantial  $ARR$ . Hereby a tracer gas is injected and measured in the air flow. This is the only possibility, since all other measurable intrinsic properties of the air are correlated to the temperature. Tracer gas measurements are widely used in medicine, in ventilation experiments for buildings and air conditioning systems. Inert tracer gas washout tests are for example used to perform extended lung function tests (Robinson et al., 2013). In contamination experiments Tang et al. (2011) use a tracer gas to simulate the spreading of diseases in hospitals. Contaminations in sewers are investigated by Lepot et al. (2014) using a Rhodamine tracer. Similarly, the spreading of hot or cold air is quantified in buildings (ISO12569, 2012). For example Ghazi and Marshall (2014) use a carbon dioxide tracer gas to determine and characterize leaks across windows, Cui et al. (2015) use a decay rate method to determine the air change rate of buildings. These measurements however are not transferable to the described measurement environment, due to the harsh conditions at the STJ. High circular air mass flows with large leak rates occur which are caused by an  $ARR$  of smaller than 100 %. The high mass flows do not allow for any gases already present in air with concentrations greater 0.1 %, since these would lead to a strong background signal. The openness of the air circuit prevents the use of environmentally harmful gases. The occurring surface temperatures further limit the possible tracer gas candidates. The commonly used  $SF_6$  can only be heated without decomposition up to  $500^\circ\text{C}$  in the absence of catalytic metals and has furthermore the highest global warming potential of all gases (Koch, 2003; Forster et al., 2007). Goldsworthy et al. (1990) use a helium tracer to measure the flow rate of large ducted gas flows under harsh conditions. These measurements are however not conducted for leaks ( $ARR < 1$ ) or to examine circular flows.

### 1.2.4 Return Air Visualization

In addition to measuring the  $ARR$  it is important to visualize the return air. This improves the understanding of the causes of  $ARR$  changes. The examined return air flow consists of hot air flows with temperatures of up to  $200^\circ\text{C}$  at the STJ and is surrounded by ambient air. The ambient air flow can not be seen, since it is too cold. The examined return air flow is large ( $10\text{ kg/s}$ ) and open to the environment. The area of interest is subjected to highly concentrated solar radiation, making any installation of direct flow

measurement instrumentation impossible. Therefore only optical based measurement methods remain.

One possible method would be the qualitative use of PIV. This is not to be confused with the previously covered quantitative approach of measuring the ARR using PIV. To visualize the return air, particles or disco fog could be added to the air circuit. These could be qualitatively processed using PIV algorithms to determine the movement of the return air flow. However, a particle dotted flow is difficult to produce on this scale. To be able to use reasonable particle concentrations, the examined plane would additionally have to be illuminated with a high powered laser, leading to further difficulties in its realization. Particles are furthermore unwanted in the system and in the environment. Therefore particle-based techniques were not further considered. Disco fog can be used in a cold environment but it disintegrates under the occurring high temperatures.

A possible approach would be to make use of the fact that air at different temperatures has a different refractive index. This is used in Schlieren measurements. Since the background cannot be altered easily on such a scale, the only possible method would be the natural background oriented Schlieren method as described by Raffel (2015). Here the change of the background is used to calculate the refractive properties of the air between the background and the camera. The examined solar receivers are generally located at the top of a solar tower. Therefore high constructional effort would be required to be able to observe the receiver in front of a non homogeneous background (i.e. the ground). The suitability of the different measurement techniques including the newly developed Induced Infrared Thermography (IIT) are shown in Table 1.1. The different measurement techniques are grouped according to the underlying type of measurement. Point measurements are not suitable since the examined return air flow occurs on a large area.

### 1.2.5 Infrared Thermography of Gases

Infrared measurements are a well-known approach to measure heat transfer or for spectroscopic analysis of gases. Direct visualization of gas flows using infrared radiation has however hardly been used at all for visualization and measurement of gas flows. Gordge and Page (1993) use infrared imaging to investigate a subsonic, non-isoenergetic air/carbon dioxide axisymmetric jet. Yoon et al. (2006) use pure heated carbon dioxide

Table 1.1: Different measurement techniques and their suitability for a return air visualization. Based on Risthaus (2015).

<b>Type of measurement</b>		
Measurement technique	Suitability	Reason for suitability
<b>Velocity</b>		
Pressure Probes	unsuitable	Point measurement
Hot-Wire Anemometer	unsuitable	Point measurement
Pulsed Hot-Wire Anemometer	unsuitable	Point measurement
<b>Tracer</b>		
Laser Doppler Anemometry (LDA)	unsuitable	Point measurement
Laser Flash Analysis (LFA)	unsuitable	Point measurement
Particle Image Velocimetry (PIV)	unsuitable	Particles unwanted
Particle Tracking Velocimetry (PTV)	unsuitable	Particles unwanted
Laser Surface Velocimetry (LSV)	unsuitable	Particles unwanted
Droplet Tracking Velocimetry (DTV)	unsuitable	Point measurement
Molecular Tagging Velocimetry (MTV)	unsuitable	High laser output
<b>Refractive Index</b>		
Background Oriented Schlieren (BOS)	hardly suitable	High construction effort
Laser Speckle Photometry (LSP)	unsuitable	High construction effort
Schlieren PIV	hardly suitable	High construction effort
Shadowgraph	hardly suitable	High construction effort
Interferometry	unsuitable	Line measurement
<b>Infrared Radiation</b>		
IR-Thermography	unsuitable	Air is hardly IR-active
Induced Infrared Thermography (IIT)	suitable	$CO_2$ is IR-active

to visualize the flow from nozzles used in walk-through portal detection systems to screen passengers for the presence of explosives.

To visualize a poorly infrared-active gas, an infrared-active gas can be introduced into the air flow which is to be examined. The infrared-active gas flow can be visualized using an infrared camera. Although this technique existed beforehand on a lab scale, the technique was developed independently at the DLR. It was first described by (Narayanan et al., 2003) and will henceforth be called Induced Infrared Thermography (IIT). Narayanan et al. (2003) used sulfur hexafluoride ( $\text{SF}_6$ ) to visualize the air flow of a free impinging and reattachment subsonic air jets in the range of  $8 - 13 \mu\text{m}$ . The application of IIT outside the laboratory is not yet covered in literature.

## 1.3 Outlining the Research

The presented thesis is motivated by following research objectives and was conducted according to the displayed course of investigation.

### Research Objectives

The focus of this thesis lies on the development of measurement techniques for the analysis of the open volumetric receiver concept in respect to the ARR. The first objective is the development of a measurement technique for the quantification of the ARR with maximum accuracy. Moreover, it has to be applicable without and with the presence of solar irradiation. A minimum measurement uncertainty of  $\pm 5\%$  is aimed for to utilize the ARR measurements for evaluation purposes. The second objective lies in the visualization of the returned air. This improves the understanding of the occurring flow phenomena which govern the ARR.

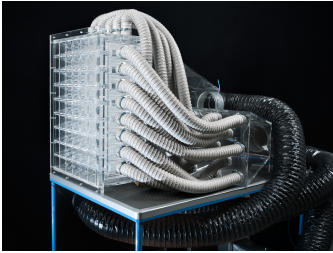




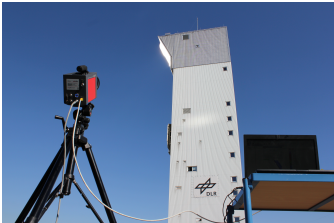
### Course of Investigation

The ARR measurement as well as the measurement technique to visualize the return air are both first developed on a laboratory scale, then tested on an intermediate scale

and finally applied to the STJ. The ARR measurement has been realized by developing a tracer gas method. To achieve this, as well as for the validation of the tracer gas measurement technique, a 1:2 scale model of a subreceiver (54 absorber modules) with the corresponding air circuit of the STJ (1080 absorber modules) was constructed. To gain further understanding and improve the application of the measurement methods, both measurement methods are tested under environmental conditions. For the ARR measurement, this was realized at the Testreceiver of the STJ with 9x6 absorber modules. The feasibility stage of the return air visualization was successfully conducted at a single volumetric absorber module mounted on a solar dish at the *Plataforma Solar de Almería*, Spain. For the measurement phase the main receiver of the STJ was chosen for both measurement techniques. Additionally, the return air flow in front of the Testreceiver was visualized. Table 1.2 shows an overview of the different development stages which were used.

Within this thesis, the emphasis lies on the measurement stages of both air return measurement and return air visualization. Additionally the development stage of the ARR measurements at the receiver model is covered, since used for validation purposes. The remaining stages are not covered for the sake of brevity.

Table 1.2: The measurement environments which were used to develop the measurement techniques are shown. Of the different development stages both the measurement stages and the model stage of the ARR measurement are covered within this thesis.

Stage of development	Air return ratio measurement	Return air visualization
Model Stage	 <p>Model receiver</p>	 <p>Model receiver</p>
Feasibility Stage	 <p>Testreceiver STJ</p>	 <p>Solar dish Almería</p>
Measurement Stage	 <p>Main receiver STJ</p>	 <p>Main/Testreceiver STJ</p>





## 2 Theory

*"It doesn't matter how beautiful your theory is, it doesn't matter how smart you are. If it doesn't agree with experiment, it's wrong."*

— Richard P. Feynman

This chapter covers the theory behind the developed ARR measurement (Section 2.1) as well as the corresponding uncertainty analysis in Section 2.2. The theory of the return air visualization is described in the last section of the current chapter 2.3.

### 2.1 Theory of Air Return Ratio Measurement

Due to the lack of alternatives, as described in Section 1.2, it was decided to devise and apply a tracer gas method to precisely measure the ARR.

#### 2.1.1 Tracer Gas Method for ARR Measurements

As a first step on the way to an ARR measurement system a suitable tracer gas must be found. The high temperatures, high air mass flows, openness and presence of concentrated solar radiation at the STJ pose requirements on the choice of the tracer gas. It must hence be environmentally friendly, stable under high temperatures and its natural concentration in air must be low. This reduces the choice of tracer gases down to the noble gases. In Table 2.1 the different traces gases are compared according to the mentioned properties and the price. Due to economic reasons helium was chosen as tracer gas.

The amount of injected helium is small compared to the airflow. The maximum molar fraction which was achieved at the STJ was  $\chi_{\text{He,in}} < 0.2\%$ . This allows the assumption

Table 2.1: The table shows different tracer gas candidates and their suitability according to different aspects. H\* stands for forming gas, which is a mixture of 95 % nitrogen and 5 % hydrogen. (+:excellent, ++:good, o:fair, -:poor, - -:very poor) Based on Tiddens et al. (2016b).

Property	Tracer gas candidate					
	Ar	CO <sub>2</sub>	He	H*	SF <sub>6</sub>	Ne
low natural concentration in air	- -	- -	+	++	++	++
harmless to the environment	++	o	++	+	- -	++
high thermal stability	++	++	++	- -	- -	++
low price	+	++	-	++	-	- -

that the molar mass of all examined air flows can be considered the equal ( $M_{\text{return}} \approx M_{\text{out}} \approx M_{\text{amb}}$ ). The ARR of the system in Eq. 1.1 can therefore be transformed into

$$ARR = \frac{\dot{n}_{\text{return}}}{\dot{n}_{\text{out}}} = \frac{\dot{n}_{\text{return}}}{\dot{n}_{\text{out}}} \cdot \underbrace{\frac{M_{\text{return}}}{M_{\text{out}}}}_{\approx 1}, \quad (2.1)$$

whereby  $\dot{n}_{\text{return}}$  and  $\dot{n}_{\text{out}}$  represent the molar mass flow of the return air and blown out air, respectively.

Furthermore, it can be approximated that  $\dot{n}_{\text{out}} = \dot{n}_{\text{in}}$ . For this to be true, the mass of air which is stored within the air system is not allowed to change significantly in comparison to the examined air mass flow, within the examined time frame. In our scenario this could only occur due to a reduced density of hot air. This would have to be considered, if the stored air mass would change at more than one percent of the examined air mass flow. This is not the case at the examined measurement environments. Since furthermore the added helium is negligible, the approximation is considered justified.

In Fig. 2.1 a schematic of the air circuit of an open volumetric air receiver is depicted with the occurring molar mass flows and molar fractions. A mole balance as indicated in Fig. 2.1 combined with  $\dot{n}_{\text{out}} = \dot{n}_{\text{in}}$  results in

$$\dot{n}_{\text{return}} + \dot{n}_{\text{amb}} = \dot{n}_{\text{in}} = \dot{n}_{\text{out}}. \quad (2.2)$$

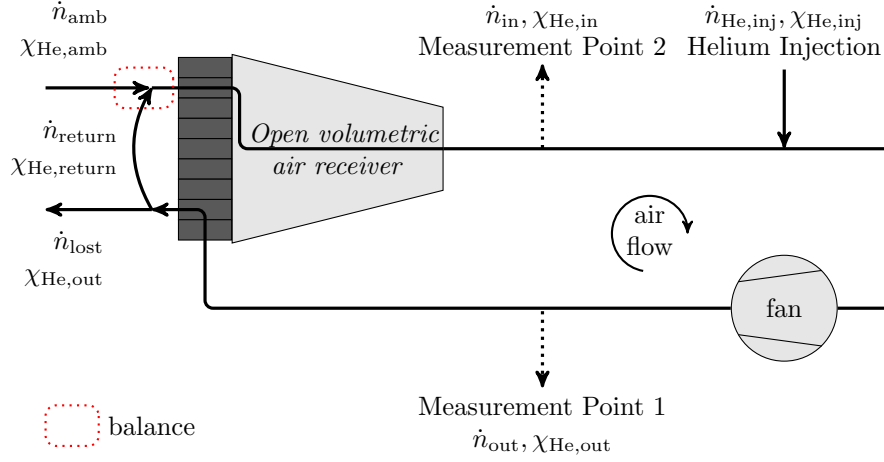


Figure 2.1: Schematic diagram of the air circuit of open volumetric air receiver. Based on Tiddens et al. (2016b).

A helium mole balance at the same location and as indicated in Fig. 2.1 results in

$$\dot{n}_{\text{return}} \cdot \chi_{\text{He,return}} + \dot{n}_{\text{amb}} \cdot \chi_{\text{He,amb}} = \dot{n}_{\text{in}} \cdot \chi_{\text{He,in}} \quad (2.3)$$

whereby  $\chi_{\text{He}}$  is the helium mole fraction at different locations in the air circuit as shown in Fig. 2.1. To determine the ARR from helium mole fractions, the helium mole fraction  $\chi_{\text{He,out}}$ , must be the same as  $\chi_{\text{He,return}}$  (see Fig. 2.1). The only way this could not be the case would occur if the helium would mix faster with the ambient air than the blown out return air. The helium tracer would therefore no longer represent the return air. That this is not the case can be assumed since in front of the receiver the blown out air  $\chi_{\text{He,return}}$  is mixed with ambient air  $\dot{n}_{\text{amb}}$  by dispersion as well as diffusion. Since the mixing that occurs is turbulent, the dispersion is much faster than the diffusion. This arises from the different origin of dispersion and diffusion in turbulent flow. Whereas diffusion is caused by the small-scale Brownian motion, the turbulent dispersion is caused by gusts and eddies. (Cussler, 2009) Therefore dispersion is the dominant cause of mixing and has no effect on  $\chi_{\text{He,return}}$  but only on the mixing of  $\dot{n}_{\text{return}}$  and  $\dot{n}_{\text{amb}}$ . The effect of diffusion can therefore be neglected, causing  $\chi_{\text{He,return}} = \chi_{\text{He,out}}$ . With Eqs. 2.2, 2.3 this leads to

$$\underbrace{\frac{\dot{n}_{\text{return}}}{\dot{n}_{\text{out}}}}_{=ARR} \cdot \chi_{\text{He,out}} + \left(1 - \underbrace{\frac{\dot{n}_{\text{return}}}{\dot{n}_{\text{out}}}}_{=ARR}\right) \cdot \chi_{\text{He,amb}} = \chi_{\text{He,in}} \cdot \quad (2.4)$$

Table 2.2: The table shows the number of gas bottles (50l, 300 bar) needed to achieve a static helium mole fraction of  $100 \cdot \chi_{\text{He,amb}}$  for one hour for different air mass flows ( $\dot{m}_{in}$ ) and ARR within an air circuit. Based on Tiddens et al. (2016b).

Corresponding receiver	Air mass flow $\dot{m}_{in}$ [kg/s]	Air return ratio [%]			
		99	90	50	0
Model	0.1	0.0001	0.0011	0.0054	0.0109
Testreceiver	1	0.001	0.011	0.054	0.109
STJ	10	0.01	0.11	0.54	1.09
	100	0.1	1.1	5.4	10.9

Combining this with Eq. 2.1, the ARR can be expressed as

$$ARR = \frac{\chi_{\text{He,in}} - \chi_{\text{He,amb}}}{\chi_{\text{He,out}} - \chi_{\text{He,amb}}}. \quad (2.5)$$

This shows, that the ARR can be determined measuring only  $\chi_{\text{He,in}}$ ,  $\chi_{\text{He,out}}$  and  $\chi_{\text{He,amb}}$ , as long as  $\chi_{\text{He,out}} \neq \chi_{\text{He,amb}}$ . To achieve this, helium must be injected into the system. The locations of the helium injection and the mole fraction measurement are chosen to be suitable for the application of the different measurement techniques which are described within the following sections. The injection location furthermore ensures that the injected helium is mixed by the fan before the next measurement location (see Fig. 2.1). The helium injection time was minimized to reduce consumption, reduce measurement time and increase temporal resolution without lowering measurement result quality. The amount of added helium is small resulting in a low helium mole fraction of around ( $1\text{‰} \approx 200 \cdot \chi_{\text{He,amb}}$ ) in the system. This is a mole fraction that can be realistically achieved at the STJ. Table 2.2 shows the amount of helium needed for different mass flow scenarios to achieve a helium mole fraction of  $100 \cdot \chi_{\text{He,amb}}$  for one hour. This is a realistic time frame for one day of measurements.

### 2.1.2 Static ARR Measurement

The simplest way to determine the ARR via a tracer gas measurement is to inject the tracer gas as indicated in Fig. 2.1. The tracer mole fraction of blown out air is measured at measuring point 1 ( $\chi_{\text{He,out}}$ ) and the sucked in air at measuring point 2

( $\chi_{\text{He,in}}$ ). When additionally the ambient helium mole fraction  $\chi_{\text{He,amb}}$  is known, the ARR can be determined directly by using Eq. 2.5. Since measuring at equilibrium no helium flow occurs due to diffusion of helium into the contact material. Therefore no need arises for a diffusion background correction. Furthermore, no dynamic error correction has to be conducted, due to the static nature of the measurement.

Before determining the ARR, two further prerequisites have to be examined: The distribution of helium at the measuring points' cross sections as well as peripheral leaks outside of the receiver.

### **Mixing**

The helium mole fraction has to be measured across the cross section of the piping at both measuring points. At these points the helium mole fraction must be homogeneously distributed to allow single point sampling. Custom made gas extraction probes had to be designed for the measurements at different defined locations. These are described in Section 3.2.2.

### **Peripheral Leakage Measurement**

To measure the ARR of the receiver, it must be assured that the rest of the air circuit is leak-tight. This is only possible at the receiver model and is not feasible at the STJ. The air circuit is filled with helium, and the leak rate is measured per circulation period. A qualitative helium leak and sniffing inspection from the outside of the system as well as countermeasures are conducted to minimize the leakage of the system.

During measurements at the STJ the mole fraction inside of the building has to be monitored. If no significant increase in the helium mole fraction is detected, the peripheral leakage can be neglected. This is expected for the STJ, since the air circuit is sealed very well to prevent energy losses.

### 2.1.3 Dynamic ARR Measurement

For the previously described static measurement two measuring points are needed. This causes additional problems since the homogeneity of the tracer within the air circuit at these points is uncertain. Therefore a dynamic ARR measurement was developed. Since dealing with a circular air system, the ARR can be measured using one measuring point when measuring dynamically. The measurement is conducted by injecting helium with a fixed flow rate and duration into the system and measuring the resulting mole fraction response over time. In contrast to the static measurement, the transient mole fraction curves are relevant and the complete mole fraction curve is fitted instead of measuring at equilibrium.

The measuring point is chosen to be directly behind the blower, since the mole fraction of helium across the cross section of the piping is most likely homogeneous there in all measurement environments. The disadvantage of the dynamic measuring method is that its measurement procedure and the evaluation of the data is more complex compared to the static measurement.

In Fig. 2.2 the theoretical mole fraction response is shown if dispersion of helium is ignored. The leading edge shows an increase of mole fraction until the mole fraction reaches its maximum at equilibrium. As soon as the helium injection is stopped, the helium mole fraction decreases every cycle with a period length of  $T_{\text{circ}}$ , by the factor  $ARR$ . The distinguished mole fraction steps in Fig. 2.2 disappear due to dispersion. The trailing curve can now be described by

$$\chi_{\text{He,trailing,norm}}(t) = ARR^{t/T_{\text{circ}}}, \quad (2.6)$$

because every circulation period, the mole fraction is reduced by the factor  $ARR$ . This is also true if the data is not normalized

$$\chi_{\text{He,trailing}}(t) = A \cdot (ARR^{t/T_{\text{circ}}}). \quad (2.7)$$

The leading edge must have the same final amplitude  $A$  as the trailing edge and the molar fraction is increasing with the same  $ARR$  as the trailing edge. Therefore the mole fraction response of the leading edge can be described by the following exponential growth function

$$\chi_{\text{He,leading}}(t) = A(1 - (ARR)^{t/T_{\text{circ}}}). \quad (2.8)$$

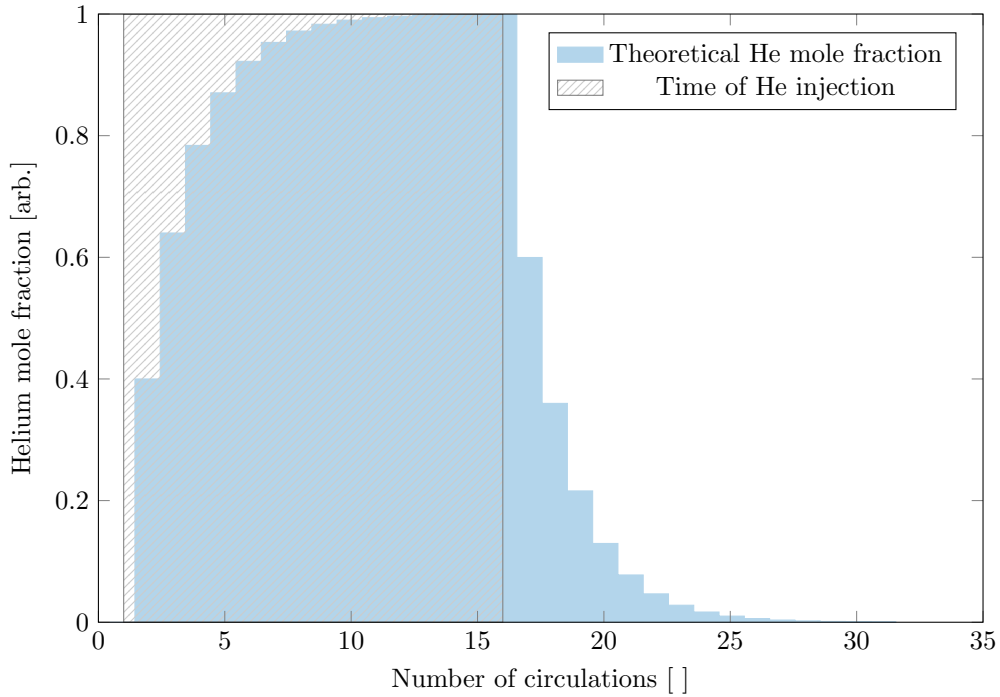


Figure 2.2: The theoretical helium mole fraction response of a circular air circuit with an  $ARR = 0.6$ , ignoring the dispersion of helium in the system. Based on Tiddens et al. (2016b).

Since the goal is to determine the  $ARR$ , these functions must be fitted to the helium mole fraction data, with the  $ARR$  as the only unknown parameter in Eqs. 2.8 and 2.7. In order to achieve this, the circulation period  $T_{\text{circ}}$  must be measured and  $A$  is normalized.

### Circulation Period Measurement

The period  $T_{\text{circ}}$  can be measured by injecting helium with the shortest duration possible into the system and measuring the mole fraction response. By measuring the time between two measured mole fraction peaks caused by the same injected helium, the circulation period is determined. The theoretical helium mole fraction within a circulation period measurement is shown in Fig. 2.3, ignoring the dispersion of helium in the system. Due to dispersion, the peaks shown in Fig. 2.3 can overlap. If the overlap becomes too strong, the maximums of the peaks shift. This does not occur for the examined measurement environments.

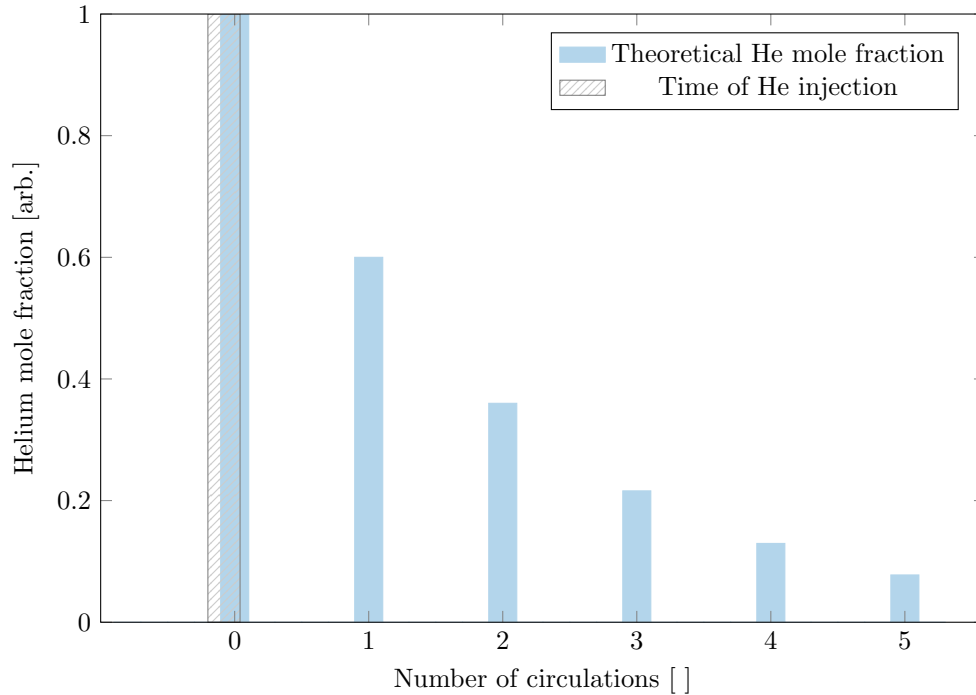


Figure 2.3: The theoretical helium mole fraction response of a circulation measurement of an air circuit with  $ARR = 0.6$ , ignoring the dispersion of helium in the system. A circulation measurement can be seen in Fig. 4.4.

### Correction of the Helium Diffusion within the Air Circuit

The diffusion of helium into and away from the materials surrounding the flowing air changes the measured helium mole fraction. Since all measurements at the STJ are conducted using the thermal storage, the involved surface area is very large. The helium flow due to diffusion of helium into and away from the surrounding material is significant and needs to be corrected. The decay rate of this diffusion helium flow is slower than that of the helium flow within the air circuit, when the helium injection is stopped. This arises from the fact that the helium flow due to diffusion is caused by a difference in helium mole fraction between the air circuit and its contact surfaces.

At the receiver model a helium flow due to diffusion within the air circuit was not expected due to the small occurring contact surface area. This was confirmed experimentally, eliminating the need for a correction at the receiver model.

At the STJ the diffusion of helium into and away from the materials surrounding the air



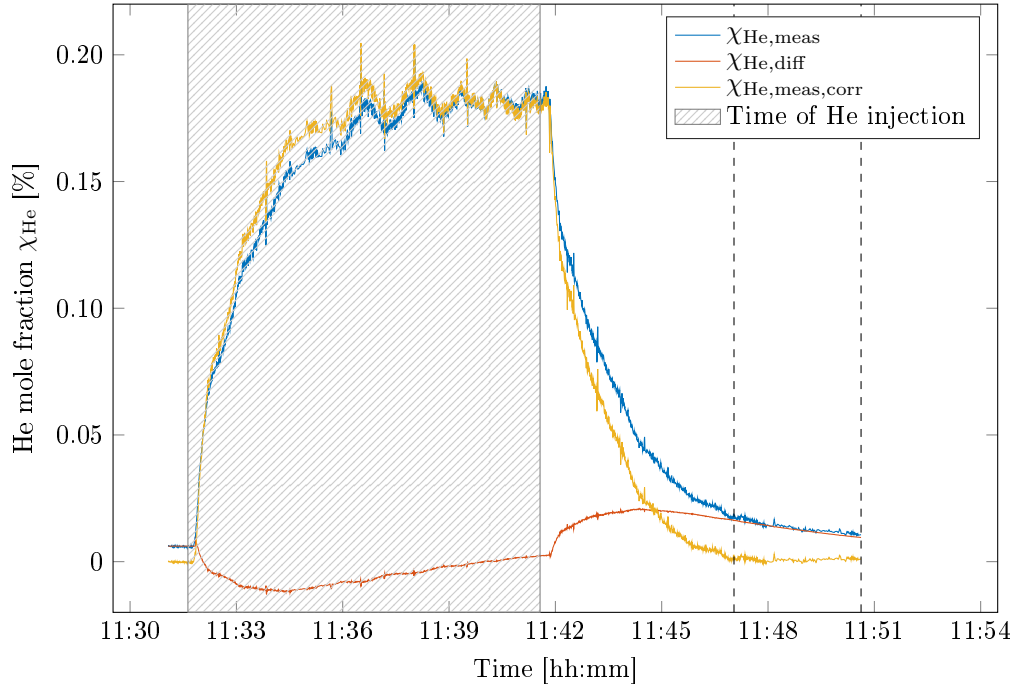


Figure 2.4: The correction due to diffusion of helium into the contact surface area is shown for a typical dynamic measurement. The measurement was conducted without irradiation with an air mass flow of  $(9.96 \pm 0.04)$  kg/s.

flow, changes the measured helium mole fraction. This needs to be corrected. At the receiver model this helium flow was neglected, and therefore also not corrected. Since all measurements at the STJ were conducted using the thermal storage, the involved contact surface area is very large. This makes it necessary to correct the diffusion background. A typical diffusion correction is shown in Fig. 2.4. First the helium flow due to diffusion  $\chi_{\text{He,diff}}$  is determined. Therefore, the far end of the depleting signal, indicated with dashed lines in Fig. 2.4, was fitted to find the decay time of the slow component of the signal. This signal was extrapolated backwards and multiplied with the normalized amplitude of the signal  $\chi_{\text{He,meas}}$ . This resulting helium flow due to diffusion  $\chi_{\text{He,diff}}$  can simply be removed from the signal according to

$$\chi_{\text{He,meas,corr}} = \chi_{\text{He,meas}} - \chi_{\text{He,diff}} \cdot \quad (2.9)$$

That this method is appropriate is underpinned by the successful validation of dynamic and numeric method in Section 4.3.1. A further indication is  $\chi_{\text{He,meas,corr}}$  becomes constant from 11h:39m to the end of injection as well as after 11h:48m.

## Transfer Function Measurement

In contrast to the static method, the temporal information of the signal is crucial for the dynamic measurement. Therefore it is important to remove the distortion due to the measurement apparatus from the signal. Thus the mass spectrometer measurement of the dynamic mole fraction must be corrected for its response characteristics. To achieve this, the transfer function of the measurement set up must be known. This allows us to correct the resulting dynamic error. Since dealing with a complicated measurement system the transfer function can not be determined analytically. It is determined by conducting a black box system analysis of the setup. By introducing a step function into the system and measuring the step response  $\chi_{\text{He,step}}$ , the transfer function  $G(s)$  can be measured since

$$\mathcal{L}(\chi_{\text{He,step}}(t)) = G(s)/s. \quad (2.10)$$

Hereby  $\mathcal{L}(\chi_{\text{He,step}}(t))$  is the Laplace transformed of the step response  $\chi_{\text{He,step}}(t)$  and the parameter  $s$  is the complex number frequency. The step function is realized experimentally by filling a flask with a well defined helium-air mixture and covering the flask with a rubber seal. By attaching a plug and needle to the end of the measuring probe, the rubber seal is pierced, the probe enters the flask which is immediately sealed again by the plug (see Fig. 2.5). As shown in Fig. 2.6, the transmission element PT<sub>2</sub> response is a very good fit for the mole fraction step response, since the normalized root-mean-square deviation is very close to zero. The transmission element PT<sub>3</sub> doesn't yield more accuracy but introduces an unnecessary variable. Therefore the PT<sub>2</sub> model is chosen, resulting in a step response in the time domain of

$$\chi_{\text{He,step,norm}}(t) = 1 - \frac{T_1 e^{-\frac{t}{T_1}}}{T_1 - T_2} + \frac{T_2 e^{-\frac{t}{T_2}}}{T_1 - T_2}, \quad (2.11)$$

with  $T_1, T_2$  as fitting parameters. Since the measurement setup is treated as a black box, the form of the transfer function was checked at 42 randomly chosen different mole fraction levels of helium  $\chi_{\text{He,const}}$  in the flask (see Fig. 2.5). The time delay of the measurement setup was ignored. This is possible, since it is not relevant for the ARR measurement. The transfer function in frequency domain, corresponding to the PT<sub>2</sub> transmission element, is found to be

$$G(s) = \frac{1}{(s \cdot T_1 + 1)(s \cdot T_2 + 1)}. \quad (2.12)$$

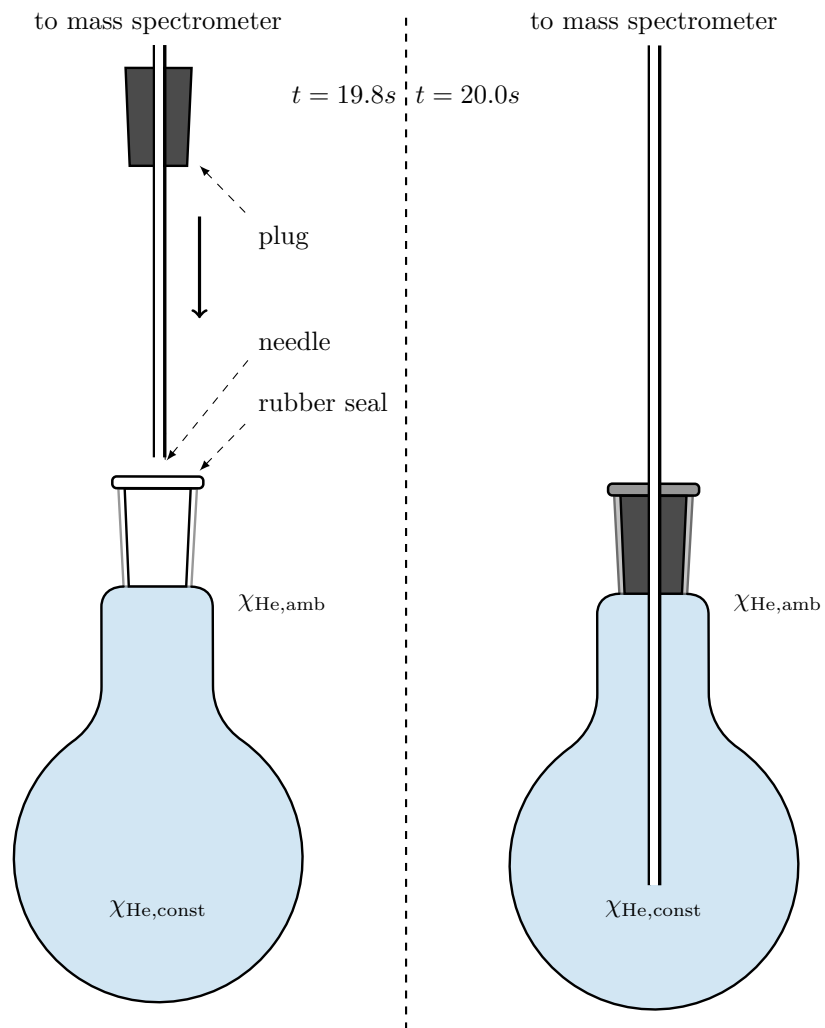


Figure 2.5: The figure shows schematically the creation of a helium mole fraction step function at the inlet of the measuring probe. The indicated time corresponds to the time in Fig. 2.6. (Tiddens et al., 2016b)

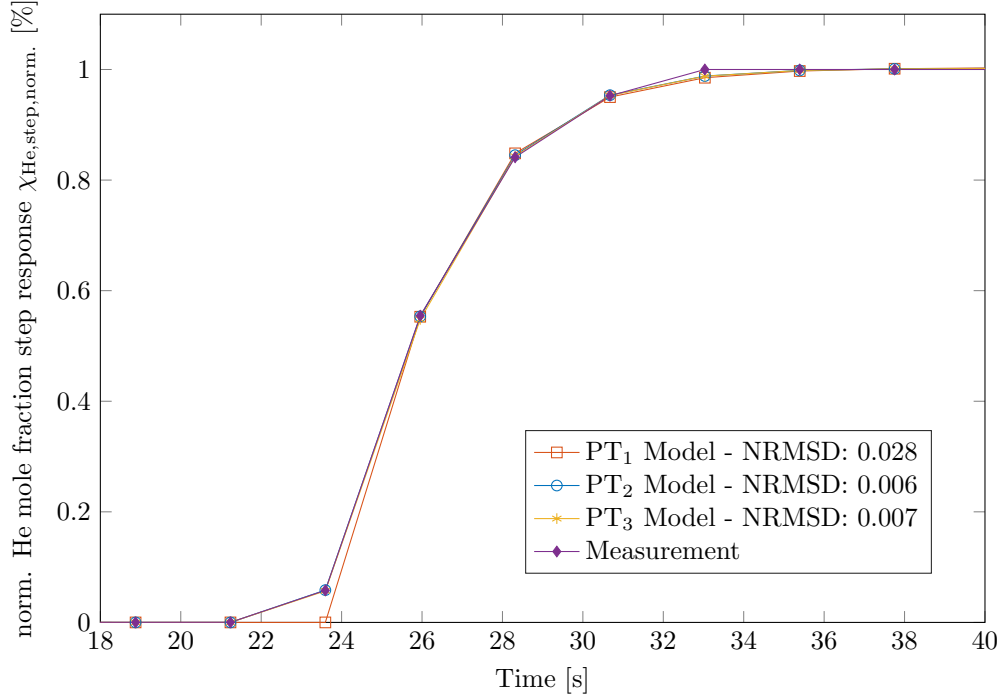


Figure 2.6: The figure shows an exemplary step response of the measurement setup compared to model responses of a  $PT_1$ ,  $PT_2$  and  $PT_3$  transmission element response. The normalized root-mean-square deviation (NRMSD) of the models are given. Based on Tiddens et al. (2016b).

For the setup at the Testreceiver the transfer function measurement resulted in  $T_1 = 0.12s$ ,  $T_2 = 0.39s$  and for the setup at the STJ  $T_1 = 0.42s$ ,  $T_2 = 0.19s$ . These measurement results in very similar correction functions, which are covered in the next section.

### Compensation of Dynamic Measurement Error

Having found the transfer function of the measurement setup, the dynamic measurement error can be compensated as following. First the effect of the non ideal transfer function on the true mole fraction data must be determined before being compensated. The following derivation of the dynamic error correction is shown exemplary for the leading edge.

The normalized true mole fraction of the leading edge  $\chi_{\text{He,true,leading}}(t)$  can be described

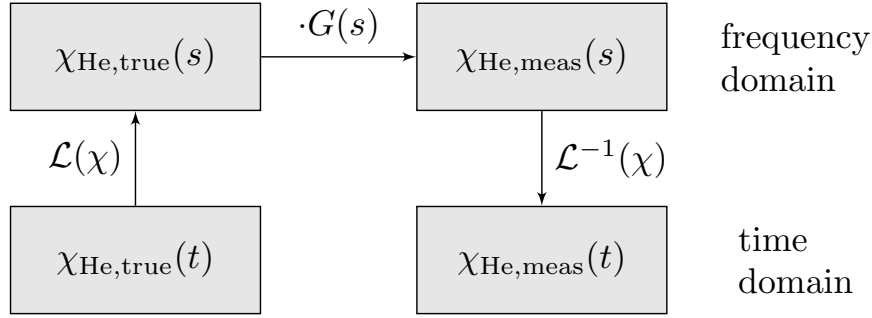


Figure 2.7: The figure shows the general outline of the derivation measured mole fraction function  $\chi_{\text{He,meas}}(t)$ . Whereby  $\mathcal{L}$  is the Laplace transformation.

according to Eq. 2.8 as

$$\chi_{\text{He,true,leading}}(t) = 1 - (\text{ARR}_{\text{true}})^{t/T_{\text{circ}}}. \quad (2.13)$$

This true mole fraction is unmeasurable since all measuring apparatus have a non ideal transfer function. Because the transfer function of the setup is known, the measurable mole fraction function  $\chi_{\text{He,meas}}(t)$  can be calculated. The general outline of the derivation of this measured mole fraction function is shown in Fig. 2.7. The Laplace transformed of Eq. 2.13

$$\chi_{\text{He,true,leading}}(s) = \mathcal{L}(\chi_{\text{He,true,leading}}(t)) = \frac{\ln(\text{ARR}_{\text{true}})}{s(\ln(\text{ARR}_{\text{true}}) - s \cdot T_{\text{circ}})} \quad (2.14)$$

can be multiplied by the transfer function  $G(s)$  (Eq. 2.12) to yield

$$\chi_{\text{He,meas,leading}}(s) = \chi_{\text{He,true,leading}}(s) \cdot G(s) = \frac{\ln(\text{ARR}_{\text{true}})}{s(\ln(\text{ARR}_{\text{true}}) - s \cdot T_{\text{circ}})} \cdot \frac{1}{(s \cdot T_1 + 1)(s \cdot T_2 + 1)}. \quad (2.15)$$

Transferred back to the time domain using the inverse Laplace transformation

$\mathcal{L}^{-1}(\chi_{\text{He,meas,leading}}(s)) = \chi_{\text{He,meas,leading}}(t)$  yields

$$\begin{aligned} \chi_{\text{He,meas,leading}}(t) = & 1 - \frac{\text{ARR}_{\text{true}}^{t/T} \cdot T_{\text{circ}}^2}{(T_1 \cdot \ln(\text{ARR}_{\text{true}}) + T_{\text{circ}}) \cdot (T_2 \cdot \ln(\text{ARR}_{\text{true}}) + T_{\text{circ}})} \\ & - \frac{T_1^2 \cdot \ln(\text{ARR}_{\text{true}}) e^{-\frac{t}{T_1}}}{(T_1 - T_2) \cdot (T_1 \cdot \ln(\text{ARR}_{\text{true}}) + T_{\text{circ}})} \\ & + \frac{T_2^2 \cdot \ln(\text{ARR}_{\text{true}}) e^{-\frac{t}{T_2}}}{(T_1 - T_2) \cdot (T_2 \cdot \ln(\text{ARR}_{\text{true}}) + T_{\text{circ}})}. \end{aligned} \quad (2.16)$$

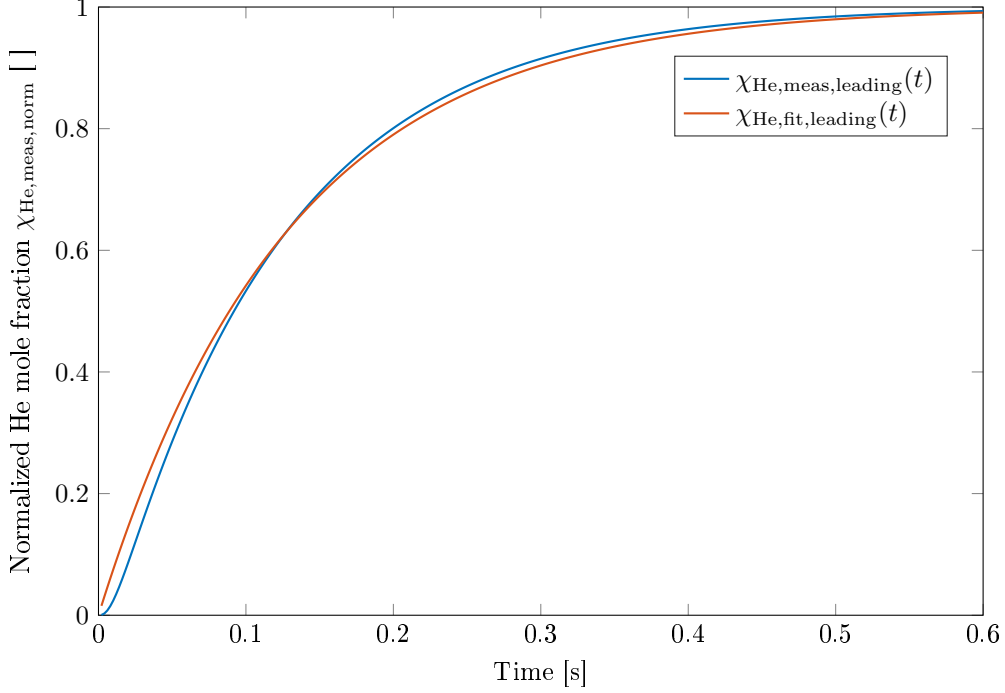


Figure 2.8: The measured mole fraction function  $\chi_{\text{He, meas, leading}}(t)$  is plotted for  $T_1 = 0.12$  s,  $T_2 = 0.39$  s,  $ARR_{\text{true}} = 0.6$ ,  $T_{\text{circ}} = 3$  s. The fit (Eq. 2.17) results in  $ARR_{\text{fit}} = 0.6259$  and in  $cor_{\text{dyn}} = 0.9586$ .

To now determine the true ARR, one must fit this curve to the measured mole fraction data. This would be possible, since all parameters except the ARR are known. With the formula that needs to be fitted it is difficult to achieve a robust fitting due to numerical reasons. Therefore a different approach has been chosen. It can be seen in Fig. 2.8 that for a given  $T_{\text{circ}} = 3$  s and  $ARR_{\text{true}} = 60\%$  equation 2.16 can be fitted very well using

$$\chi_{\text{He, fit, leading}}(t) = 1 - (ARR_{\text{fit}})^{t/T_{\text{circ}}}, \quad (2.17)$$

resulting in only a small difference between the fitted  $ARR_{\text{fit}}$  and  $ARR_{\text{true}}$ . A dynamic correction  $cor_{\text{dyn}}$  can now be defined as a function of  $ARR_{\text{true}}$  and the circulation period  $T_{\text{circ}}$  as following

$$cor_{\text{dyn}}(ARR_{\text{true}}, T_{\text{circ}}) = \frac{ARR_{\text{true}}}{ARR_{\text{fit}}}, \quad (2.18)$$

and determined numerically. In order to do so, first  $T_1$  and  $T_2$  are determined as previously shown in Fig. 2.5. Then for a likely range of circulation periods  $T_{\text{circ}}$  and  $ARR_{\text{true}}$ , the measured helium mole fraction  $\chi_{\text{He, meas, leading}}$  is calculated according to Eq. 2.16 numerically.  $ARR_{\text{fit}}$  is found by fitting Eq. 2.17 to  $\chi_{\text{He, meas, leading}}(t)$ . The dynamic

correction  $cor_{\text{dyn}}(ARR_{\text{true}}, T_{\text{circ}})$  is determined numerically for 2500 combinations of  $T_{\text{circ}}$  and  $ARR_{\text{true}}$  values using the described method. This correction is conducted for each measurement environment separately. The correction function ( $cor_{\text{dyn}}(ARR_{\text{true}}, T_{\text{circ}})$ ) is then interpolated to increase accuracy and allow  $cor_{\text{dyn}}(ARR_{\text{fit}}, T_{\text{circ}})$  to be found. The fitted ARR for the trailing edge can be determined by fitting

$$\chi_{\text{He,fit,trailing}}(t) = (ARR_{\text{fit}})^{t/T_{\text{circ}}} \quad (2.19)$$

to the measured helium mole fraction  $\chi_{\text{He,meas,trailing}}$ . The corrected ARR can be expressed as

$$ARR_{\text{true}} = ARR_{\text{fit}} \cdot cor_{\text{dyn}}(ARR_{\text{fit}}, T_{\text{circ}}). \quad (2.20)$$

For all measurements, the same mass spectrometer is used. This leads to a measured transfer function with similar  $T_1$  and  $T_2$ . The only difference arises from the length of tubing connecting the measurement probes with the mass spectrometer. The length of tubing between the measuring point 1 and the mass spectrometer at the receiver model was about 30 meter. At the STJ only about 12 meter tubing had to be used. This leads to a dynamic correction  $cor_{\text{dyn}}(ARR_{\text{fit}}, T_{\text{circ}})$  which is similar for all measurement environments.

The larger the observed helium mole fraction gradients, the larger the dynamic error correction. The gradients depend on the circulation period as well as the ARR. At the receiver model the circulation period is small. Thus the dynamic error is important. This can be seen from the correction factor, which is shown in Fig. 2.9. With short circulation periods and small ARR the correction becomes more important.

Fig. 2.10 shows the dynamic correction  $cor_{\text{dyn}}(ARR_{\text{fit}}, T_{\text{circ}})$  for the measurement at the STJ. Due to the long circulation periods at the STJ dynamic correction at the STJ is smaller than at the receiver model experiments and lies between 0.5% and 2%. The same trends of the dynamic error correction  $cor_{\text{dyn}}$  can be observed as in Fig. 2.9. The correction function is however displayed for a different region of circulation periods.

### Peripheral Leakage Measurement

A further measurement that must be conducted, is the determination of the peripheral leak in the air system of a full circulation. By closing the receiver with a lid, this

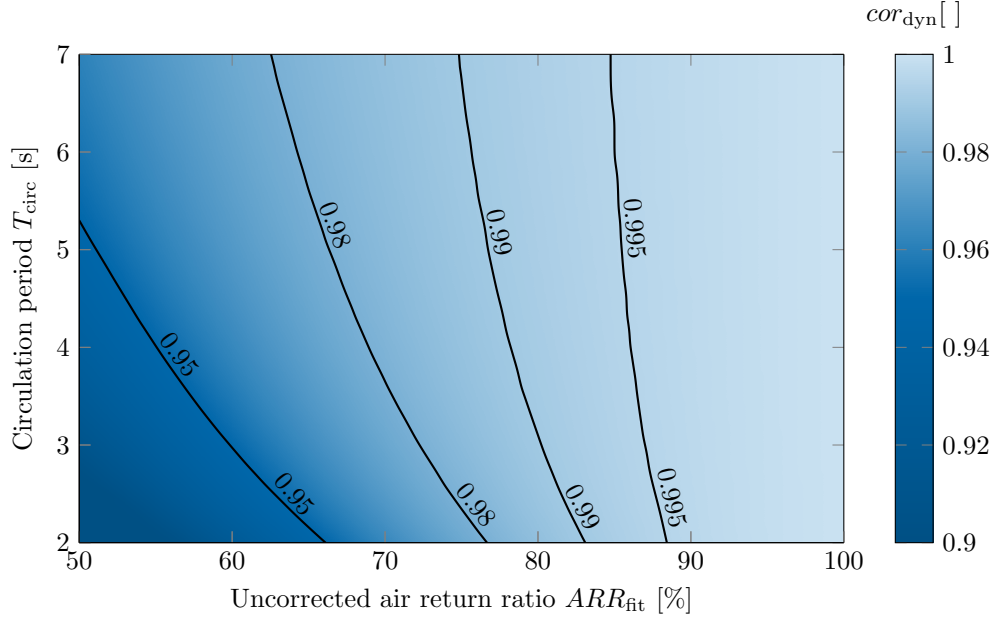


Figure 2.9: The figure shows the dynamic correction  $cor_{dyn}$  at the receiver model for different circulation periods  $T_{circ}$  and  $ARR_{fit}$  for a fixed time constant of the transfer function  $T_1 = 0.12$  s,  $T_2 = 0.39$  s.

peripheral leak rate can be measured with the dynamic method. For the determination of this leakage, the trailing side of the mole fraction curve (Eq. 2.7) is used. Therefore when injecting a small amount of helium, the formula shows that the mole fraction should stay constant if  $ARR = 1$ :

$$\lim_{ARR \rightarrow 1} (A \cdot ARR^{\frac{t}{T_{circ}}}) = A \cdot 1^{\frac{t}{T_{circ}}} = A. \quad (2.21)$$

Since this is not the case, the  $ARR_{true}$  can be broken into two parts. An ARR which occurs due to the leak of the peripheral system  $ARR_{peri}$  and the to be measured  $ARR_{meas}$  which occurs due to the open receiver:

$$ARR_{meas} = ARR_{true} \cdot ARR_{peri}. \quad (2.22)$$

When the receiver is closed  $ARR_{meas} = 1$ . Therefore  $ARR_{peri}$  can be measured according to Eq. 2.20. The compensation of the dynamic measurement is not considered, since the correction is not significant. To be able to correct the peripheral leak a correction factor  $cor_{peri}$  is defined as

$$cor_{peri} = 1/ARR_{peri}. \quad (2.23)$$



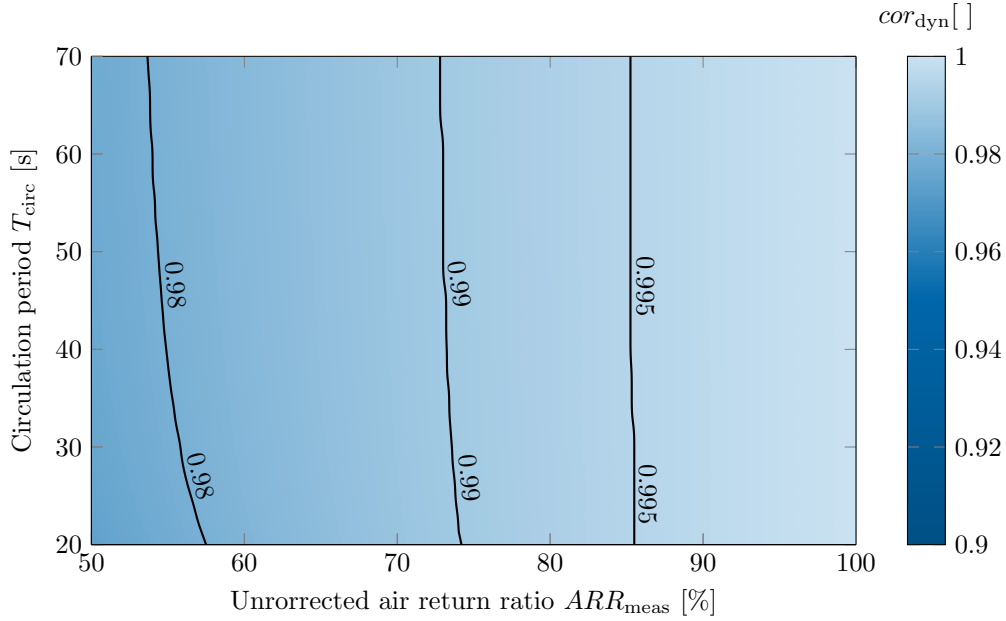


Figure 2.10: The dynamic correction  $cor_{dyn}$  at the STJ is shown for different circulation periods  $T_{circ}$  and measured  $ARR_{meas}$  for a fixed time constant of the transfer function  $T_1 = 0.42\text{ s}$ ,  $T_2 = 0.19\text{ s}$ . The scale of  $cor_{dyn}$  is the same as in Fig. 2.9, for comparison.  $ARR_{meas}$  and  $T$  are chosen according to their occurrence at the STJ.

The  $ARR_{meas}$  can hence be found by fitting the helium molar fraction data and applying the corrections  $cor_{dyn}$  and  $cor_{peri}$ :

$$\begin{aligned} ARR_{meas} &= ARR_{true} \cdot cor_{peri} \\ &= ARR_{fit} \cdot cor_{dyn}(ARR_{fit}, T_{circ}) \cdot cor_{peri}. \end{aligned} \quad (2.24)$$

At the receiver model the peripheral leak correction has been determined to be  $cor_{peri} = (1.025 \pm 0.003)\%$ . This leak is mainly caused by the blower, which has been confirmed by leak sniffing. At the STJ the helium mole fraction within the building outside of the piping was monitored regularly to check for leaks in the air circuit. No significant difference to the natural helium mole fraction could be detected. From this was concluded that no significant peripheral leak exist. Therefore no peripheral leakage correction is needed at the STJ.

### 2.1.4 Numeric ARR Measurement

For the dynamic and static measurement method a constant ARR is assumed for the duration of the leading as well as the trailing edge of the signal. This is the case for the model environment since the ambient conditions in the laboratory are fairly protected. However, at the main receiver of the solar tower the receiver is exposed to the environment and is therefore no longer protected. With the dynamic method fluctuations of the ARR during the measurement are not detectable. To achieve this, a greater temporal resolution is required. This was the goal in the development of the following numeric approach.

The numeric method is based on the fact that the mole fraction at a point in time  $\chi_{\text{He,meas}}(t + T_{\text{circ}})$  can be expressed by a mole fraction  $\chi_{\text{He,meas}}(t)$  and the  $ARR(t + \Delta t_1)$  as following,

$$\chi_{\text{He,meas}}(t + T_{\text{circ}}) = \chi_{\text{He,meas}}(t) \cdot \underbrace{ARR(t + \Delta t_1)}_{\text{at the receiver}}, \quad (2.25)$$

with  $\Delta t_1$  being the time an average air molecule needs, to cover the distance between the measuring point 1 and the receiver. This  $\Delta t_1$  is only a very small fraction of the overall circulation period. Furthermore not considered are the dispersion of the helium within the piping of the system and the natural helium background.

Helium must be injected into the system to measure the ARR. When injecting helium into the system from  $t_{\text{start}} = 0$  to  $t_{\text{end}}$ ,  $\chi_{\text{He,meas}}(t + T_{\text{circ}})$  can be expressed  $\forall t \in [0, t_{\text{end}} - T_{\text{circ}}]$  by

$$\begin{aligned} \chi_{\text{He,meas}}(t + T_{\text{circ}}) = & \chi_{\text{He,meas}}(t) \cdot ARR(t + \Delta t_1) \cdot \underbrace{\left(1 - \frac{\dot{n}_{\text{He,in}}}{\dot{n}_{\text{out}}}\right)}_{\substack{\text{less air is sucked in} \\ \approx 1}} \\ & + \frac{\dot{n}_{\text{He,in}}}{\dot{n}_{\text{out}}} \cdot \chi_{\text{He,in}}(t + \Delta t_2), \end{aligned} \quad (2.26)$$

whereby  $\Delta t_2$  is the time delay from  $t_{\text{start}}$  to the measurement of the injected helium. The difference between Eq. 2.25 and 2.26 is caused by the injection of helium. Less air is sucked into the receiver because helium is added at the injection point. Since the helium molar flow is small compared to the molar flow of air, this term can be considered to be 1. The second term can be found by measuring  $\chi_{\text{He,meas}}$  with  $ARR = 0$ . This is realized by a separate measurement at the same measuring point 1 by blowing the return air

away through a vent at the same air mass flow. This results in

$$\chi_{\text{He,meas,ARR}=0}(t + T_{\text{circ}}) = \underbrace{\chi_{\text{He,meas}}(t) \cdot \text{ARR}(t + \Delta t_1)}_{=0} + \chi_{\text{He,meas,ARR}=0}(t + \Delta t_2). \quad (2.27)$$

Combining this with Eq. 2.26 leads to

$$\chi_{\text{He,meas}}(t + T_{\text{circ}}) = \chi_{\text{He,meas}}(t) \cdot \text{ARR}(t + \Delta t_1) + \chi_{\text{He,meas,ARR}=0}(t + T_{\text{circ}}). \quad (2.28)$$

The  $\text{ARR}_{\text{meas,num}}$  can therefore be calculated  $\forall t \in [t_{\text{start}}, t_{\text{end}} - T_{\text{circ}}]$  with

$$\text{ARR}_{\text{meas,num}}(t + \Delta t_1) = \frac{\overbrace{\chi_{\text{He,meas}}(t + T_{\text{circ}}) - \chi_{\text{He,meas,ARR}=0}(t)}^{\text{sucked in through the receiver}(\chi_{\text{He,in}})}}{\underbrace{\chi_{\text{He,meas}}(t)}_{\text{blown out through the receiver}(\chi_{\text{He,out}})}}. \quad (2.29)$$

The mole fraction without using the air return mechanism  $\chi_{\text{He,meas,ARR}=0}$  can be measured. For the numeric method only one measuring point is needed.

It was so far assumed that no dispersion occurs and therefore the fluctuations of the mole fraction  $\chi_{\text{He,meas}}(t + \Delta t_1)$  do not change significantly from the receiver to the measuring point 1. The mole fraction curve  $\chi_{\text{He,meas}}$  at measuring point 1 will however be smoother over time. This results in a slightly smoother  $\text{ARR}_{\text{meas,num}}$  over time than actually present at the receiver front. This error cannot be compensated, however is considered to be small and is henceforth regarded to be negligible.

The numeric measurement of the measured helium mole fraction  $\chi_{\text{He,meas}}(t)$  does not need a dynamic error correction. This arises from the small effect of the dynamic error on the measurement, since the occurring gradients in measured helium mole fraction data are a lot smaller than using the dynamic method. Additionally, the numeric measurement is only deployed at the main receiver of the STJ where the dynamic error is small, due to large circulation periods ( $> 20$  s). A correction of the helium flow due to the diffusion within the air circuit, as described in Section 2.1.3, has to be applied to both mole fraction measurements ( $\chi_{\text{He,meas}}, \chi_{\text{He,meas,ARR}=0}$ ).

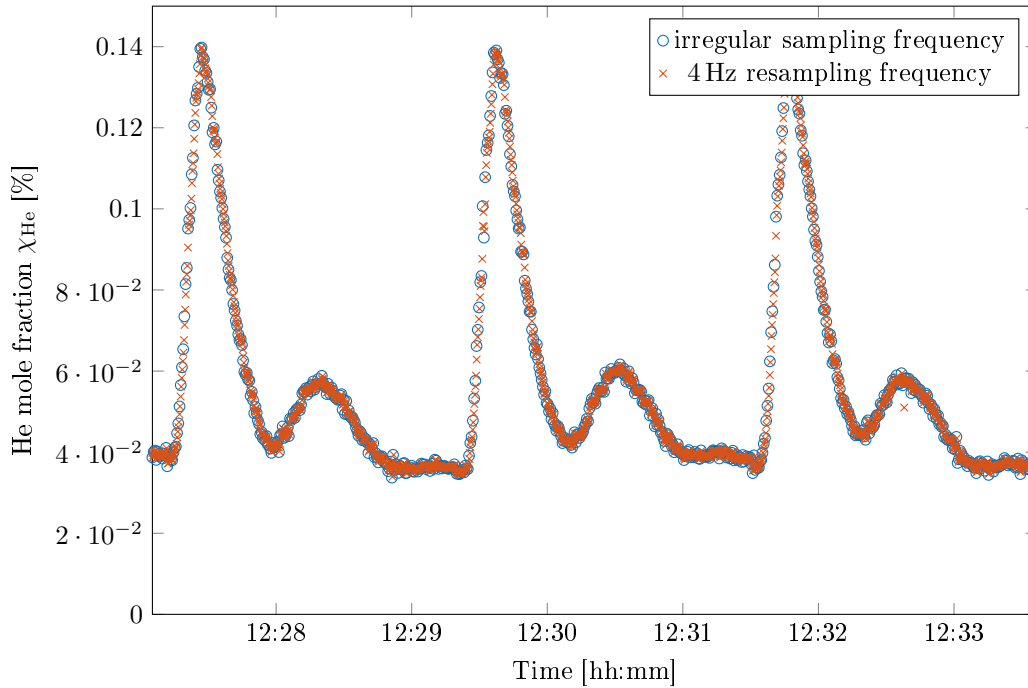


Figure 2.11: The helium mole fraction over time of a typical measurement is shown in the original irregular sampling frequency and compared to its resampled signal.

### 2.1.5 Signal Processing

To preserve the uncertainty information of the measurement data, filtering and especially smoothing of the data is not conducted. This applies also for the mass spectrometer mole fraction data which contains fluctuations due to small mole fraction fluctuations in the test chamber and detector noise.

Since the mass spectrometer data is measured at a frequency of about 2 Hz with varying length between measurements, resampling of the signal is required to handle the large data sets efficiently. Resampling must be conducted with care to prevent filtering the data. Therefore the mass spectrometer data was first examined using a Fourier transform to examine the occurring frequencies. It was found that no significant frequency components above 1 Hz exist in the data. The resampling was conducted with a linear interpolation method and a resampling frequency of 4 Hz to ensure a fair representation of the original data. A comparison between the original and resampled data is shown for a circulation period measurement in (Fig. 2.11). It can be seen that the resampled data is a very

good representation of the original mass spectrometer data.

To simplify the comparison between different measurands (mass flow, wind, etc.), data from all sources is upsampled to the same frequency of 4 Hz. This is possible because all data from other data sources has been acquired with a lower uniform sampling frequency ( $< 2$  Hz), allowing the data to be considered unchanged by upsampling.

Since the data was recorded with several different data acquisition systems with unsynchronized clocks, the data was furthermore synchronized to a uniform data acquisition time.

## 2.2 Uncertainty Analysis of ARR Measurements

Uncertainty analysis is very important to assess the significance of the results. The uncertainties are estimated according to the “Guide to the Expression of Uncertainty in Measurement” (des Poids et Mesures et al., 1995) using (Kirkup and Frenkel, 2006). Kirkup and Frenkel (2006) also give a detailed explanation of type A and B measurement uncertainties. All presented uncertainties in this thesis are displayed with a 95 % level of confidence. A sensitivity analysis is conducted to screen for relevant variables.

### 2.2.1 Uncertainty Estimation

First the uncertainty analysis of the mole fraction data  $\chi$  is conducted since this is required for all measurement methods. This is followed by the uncertainty analysis of the static method, the dynamic and the numeric method. An overview over the type of uncertainties can be seen in Table 2.3.

Due to the measurement with the mass spectrometer a type B measurement uncertainty of the measured helium mole fraction and time of these measurements has to be considered. The type B uncertainty is reduced by calibrating the mass spectrometer before each measurement campaign. To reduce the uncertainty even further, the mass spectrometer has been serviced just before the measurements at the STJ were conducted.

To calculate the type A measurement uncertainty of the static tracer gas method

Table 2.3: The table shows the types of measurement uncertainty of the three used methods for the necessary variables.

Variables	Uncertainty type of the		
	Static Method	Dynamic Method	Numeric Method
$ARR_{\text{fit}}$	-	A/B	-
$T_{\text{circ}}$	-	A	A
$cor_{\text{peri}}$	-	A/B	-
$cor_{\text{dyn}}$	-	A	-
$ARR_{\text{meas}}$	A/B	A/B	A/B

(Eq. 2.5) of  $ARR_{\text{meas,stat}}$ , the standard deviation of the mole fraction measurements at both measuring points are calculated and the result is propagated using Gaussian error propagation. The static measurement is independent in time. Therefore no type B measurement error in time has to be considered. This leaves the type B measurement uncertainty of the helium mole fraction.

For the dynamic measurement (Eqs. 2.7, 2.8) both type A and B uncertainty must be examined for the factors in Eq. 2.24

$$ARR_{\text{meas}} = ARR_{\text{fit}} \cdot cor_{\text{dyn}} \cdot cor_{\text{peri}}. \quad (2.30)$$

To calculate the type A measurement uncertainty of  $ARR_{\text{fit}}$  of the dynamic measurement, first the type A uncertainty of the leading as well as the trailing edge is determined by the goodness of their fits. Since this ARR determination is independent of the maximum helium mole fraction but dependent on time, the only type B measurement uncertainty which has to be considered is the timing uncertainty.

Since the time in Eqs. 2.7, 2.8 is divided by the circulation period a linear clock drift would be canceled out. An offset is not relevant, due to the arbitrary starting point of the fit. Because fitting is furthermore robust against small fluctuations in time, the type B measurement uncertainty of the mass spectrometer is not introduced.

The circulation period  $T_{\text{circ}}$  is additionally needed to find  $ARR_{\text{fit,dyn}}$ . The uncertainty in the circulation period  $T_{\text{circ}}$  has only a very small type A measurement error due to large statistics made possible by the automated measurement setup and fitting. At

the receiver model the short circulation period allows for a large number of repeated measurement, each with a large uncertainty. At the STJ, the circulation period  $T_{\text{circ}}$  is large, reducing the need of a high number of repetitions for a precise measurement. Here five circulation period measurements were conducted for each ARR measurement.

The uncertainty estimation of the correction term  $cor_{\text{peri}}$  is conducted in the same way as that of  $ARR_{\text{fit,dyn}}$ . This is justified, since the correction term  $cor_{\text{peri}}$  is determined in the same way as  $ARR_{\text{fit,dyn}}$ .

The correction term  $cor_{\text{dyn}}$  requires besides  $ARR_{\text{fit,dyn}}$  and the circulation period  $T_{\text{circ}}$ , the measurement of the transfer function. Here a further uncertainty occurs due to the determination of  $T_1$  and  $T_2$  of the transfer function. It arises due to the nature of the flask experiment (Fig. 2.5). The better this experiment is performed, the smaller the deviation from the ideal step function. Not introducing a perfect step function into the system results in a larger deviation from the ideal step function. This leads to an overestimation of the effect of the transfer function on the mole fraction data. Therefore the type A uncertainty is determined using the standard deviation of the ten smallest correction values, to compensate this effect. This uncertainty and that of the other required variables ( $ARR_{\text{fit,dyn}}$ ,  $T_{\text{circ}}$ ) are calculated by error propagation. This results in the uncertainty of  $ARR_{\text{meas,dyn}}$ .

The type A uncertainty of the numeric measurement is composed of the previously described type B measurement uncertainty of all mole fraction measurements, the already discussed small type A measurement uncertainty of the circulation period. Since the dynamic correction is not necessary, this uncertainty has not to be considered.

To compare  $ARR_{\text{meas,num}}$  with  $ARR_{\text{meas,dyn}}$ , the mean value of  $ARR_{\text{meas,num}}$  is required for a certain period of time. The uncertainty of this mean is chosen to be the standard deviation of the data. It is multiplied by the coverage factor to be displayed with a level of confidence of 95%.

### 2.2.2 Sensitivity Analysis

A sensitivity analysis is conducted to get a better understanding of the most important factors on the ARR and on its type A measurement error. In order to examine the

influence of a maximum of variables with a reasonable effort, an experiment using a D-optimized experiment plan has been conducted (Wember, 2008). The amount of injected helium was hereby examined in great detail, since a significant discrepancy between the measured ARRr at different helium injection rates would be an indication for a diffusion related error. It would furthermore mean that the method of measurement would influence the outcome of the measurement, hence rendering the method of measurement useless. Further examined variables are the ambient temperature, ambient air pressure and small variations in the air mass flow.

## 2.3 Theory of Return Air Visualization

As can be seen in Table 1.1 currently no measurement technique exists to visualize the return air without considerable costs and construction effort. Therefore, the Induced Infrared Thermography (IIT) was developed, whose theory and methodology is described in this chapter.

The return air itself is a poorly infrared active gas, meaning that the emissivity in the infrared region is not significant. Hence, to visualize the return air an infrared active tracer is introduced into the examined air flow. This infrared activated gas flow can be visualized using an infrared camera. The sensitivity of the camera must cover the range of emitted wavelengths of the infrared active region of the tracer.

### 2.3.1 Choice of Gas for Induced Infrared Thermography (IIT)

The examined return air flows at the STJ are large (around  $10 \text{ kg/s}$ ) and hot (around  $500 \text{ K}$ ). The measurements are furthermore exposed to the environment and concentrated solar irradiation. From these conditions, requirements on the choice of infrared active gas can be drawn. The requirements on the infrared active gas for the described application can be summarized as following.

1. It must be sufficiently active at  $500 \text{ K}$ .
2. It must be active in an infrared region which is not present in the sunlight's spectrum at the earth's surface.



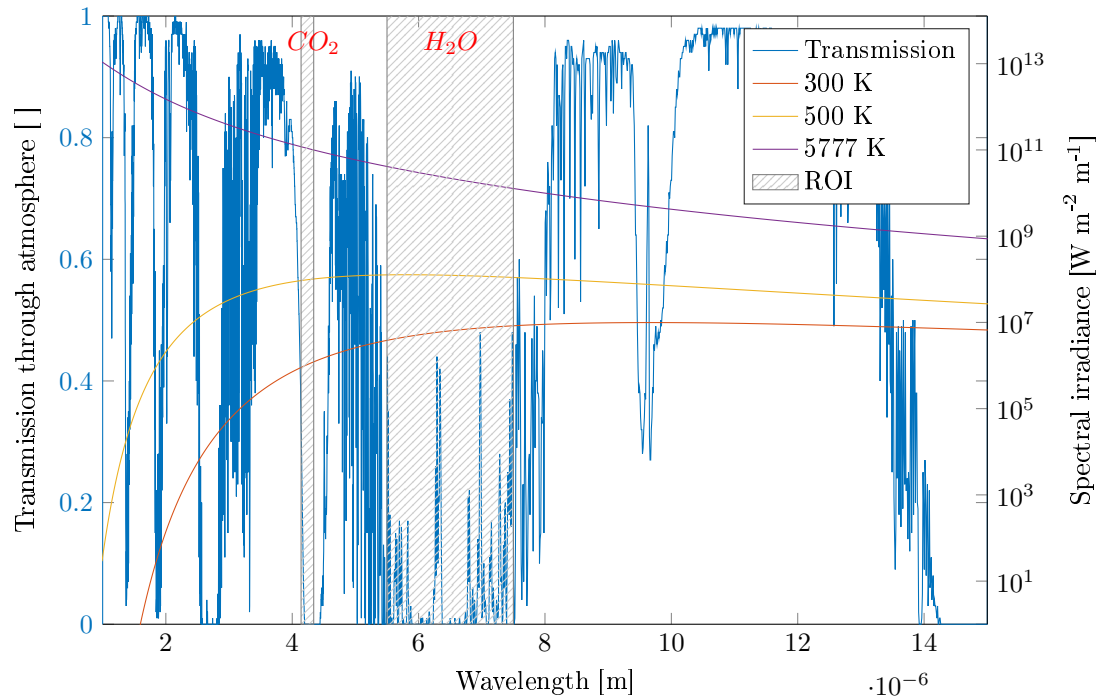


Figure 2.12: Transmission spectrum of the earth's atmosphere is shown. The spectral irradiance of a blackbody according to Planck's law is shown for three different temperatures. When examining concentrated solar radiation it can be seen that the sun's radiation dominates for all shown wavelengths when the transmission of the atmosphere is not close to zero. The region of interest (ROI) marks the carbon dioxide as well as the water vapor absorption band. Based on Tiddens et al. (2017a).

3. It must be active in an infrared region which can be detected by infrared cameras.
4. It must not be exclusively active in a region which is absorbed to quickly in the atmosphere.
5. It must not be present in high concentrations in the environment.
6. It must not be toxic and must be environmentally friendly.
7. It must be thermally stable.
8. It should be cheap.

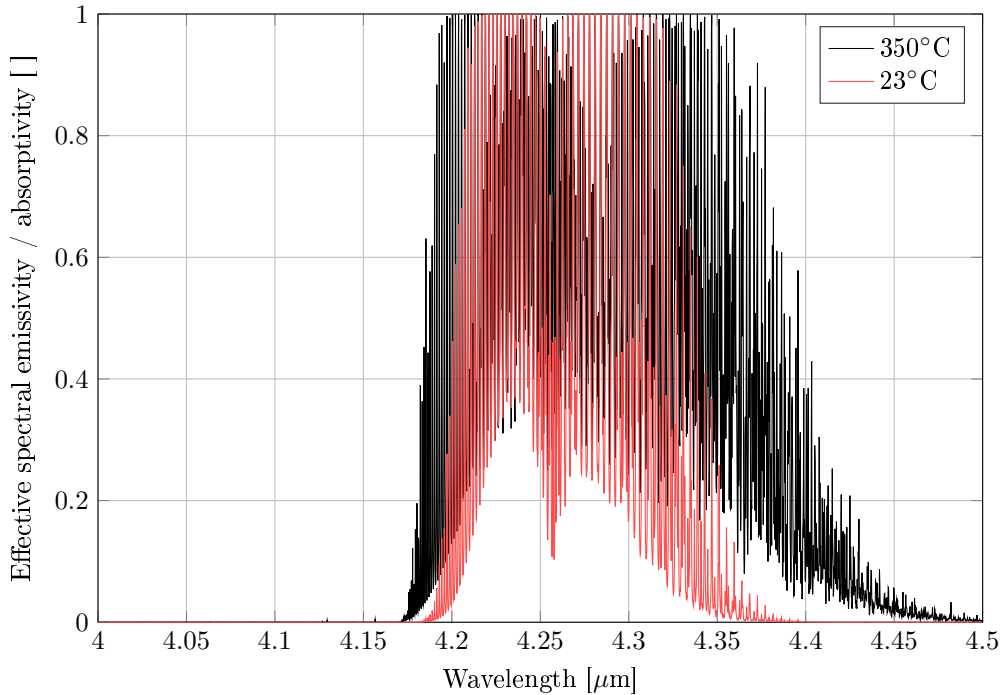


Figure 2.13: The effective spectral emissivity of carbon dioxide is shown for two different temperatures. The radiant flux is assumed to be emitted over a length of one meter by carbon dioxide at a mole fraction of 1500 ppm. It can be seen that the effective spectral emissivity peak is broader for higher temperatures. Based on Risthaus (2015).

The first two points limit the region of interest to the broad negative peak of water vapor absorption from  $5.5 \mu\text{m}$  to  $7.5 \mu\text{m}$  and the narrow negative peak caused by carbon dioxide at  $4.24 \mu\text{m}$ . These regions of interest are highlighted within the in the transmission spectrum of the earth's atmosphere in Fig. 2.12. Additionally the blackbody spectrum at the temperature of the environment, the return air and the sun are shown. It can be seen in Fig. 2.12 that these two regions of interest are the regions where high emission at the return air temperature coincides with low transmission through the atmosphere.

The carbon dioxide transmission negative peak lies within the standard range of medium wave infrared cameras, the water vapor on the other hand is only partly covered by long wave infrared cameras. (Risthaus, 2015) Therefore carbon dioxide was chosen as infrared active gas, since it's emissivity lies within the negative peak caused by carbon dioxide in the earth's atmosphere. This effect is described by Kirchhoff's law of thermal radiation.

Since carbon dioxide is also present in the earth's atmosphere, the radiation emitted by the carbon dioxide gas will also be absorbed on the way to the camera through the atmosphere. If the emission of carbon dioxide would be the same at the temperature of the return air as of carbon dioxide at ambient temperature, radiation from the hot carbon dioxide would hardly be detectable at a distance greater than several meters. The emissivity/absorptivity however depends on the temperature. This is shown in Fig. 2.13 for a hot and a cold state. It can be seen that the effective spectral emissivity peak is broader at higher temperatures. This results in a part of the emitted radiation which is hardly absorbed by the carbon dioxide in the ambient air at ambient temperatures.

Figure 2.14 shows the received radiant flux which is emitted by different carbon dioxide mole fractions, temperatures and optical path lengths. This has been calculated numerically. The radiant flux is assumed to be emitted over an optical path length of one meter, through a surface of one square meter. The atmosphere was assumed to have a relative humidity of 50% and a temperature of 23°C. It can be seen that the temperature of the carbon dioxide has by far the greatest influence on the signal strength.

Since the return air measured at the main receiver is limited to 200°C at the STJ and the camera is located 110 m away from the receiver the signal is expected to be weak. In Fig. 2.14 it can be seen that the radiant flux does not decay as fast all the time as in the first 20 m from the source. This arises from the temperature-dependent emissivity of carbon dioxide which is shown in Fig. 2.13. The reason for this is the absorption of the radiation where both the cold and the hot air have a high emissivity/absorptivity. The radiation with these wavelengths is absorbed quickly in the earth's atmosphere. In Fig. 2.13 these are the areas where the red and the black curve overlap. Additionally, the surface area covered per solid angle increases quadratically with the distance. This effect is seen in form of a lower resolution of an image recorded at a greater distance, if the same camera setup is used.

### 2.3.2 Signal Processing for Induced Infrared Thermography (IIT)

Due to the expected weak signal strength, signal processing has to be applied with great care. First, the composition of the taken infrared image is examined to identify required correction steps. The gray values of the taken infrared image at a given time  $g(x, y, t)$  can be decomposed into the original signal  $s(x, y, t)$  and noise  $\mathbf{n}(x, y, t)$ . The image could furthermore be distorted by a geometrical transformation  $T$ . This includes movement due to wobbling of the camera and distortions due to optical errors of the camera lens.

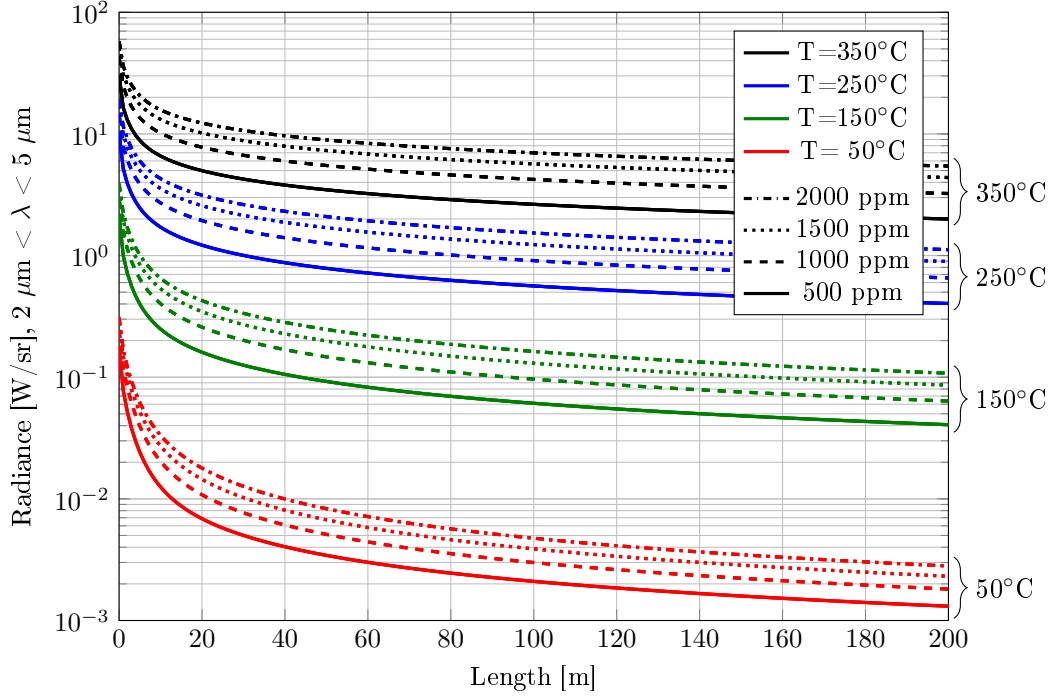


Figure 2.14: Radiant flux emitted by carbon dioxide, received per unit solid angle, depending on the optical length, temperature and mole fraction of carbon dioxide. The radiant flux is assumed to be emitted over an optical path length of one meter, through a surface of one square meter. Based on Risthaus (2015).

It can furthermore be altered by an offset  $o(x, y, t)$  of each pixel. The gray values of the taken infrared image can therefore be expressed as

$$g(x, y, t) = T[s(x, y, t) + \mathbf{n}(x, y, t)] + o(x, y, t), \quad (2.31)$$

with  $x, y$  being the spatial coordinates and  $t$  the time. To extract only the information regarding the return air flow, the original signal  $s(x, y, t)$  can be further broken down into the return air flow information  $f(x, y, t)$  and a background  $b(x, y, t)$ . This results in a further decomposition of the infrared image into

$$g(x, y, t) = T[f(x, y, t) + b(x, y, t) + \mathbf{n}(x, y, t)] + o(x, y, t). \quad (2.32)$$

The sought return air flow  $f(x, y, t)$  can therefore be expressed as

$$f(x, y, t) = T^{-1}(g(x, y, t) - o(x, y, t)) - b(x, y, t) - \mathbf{n}(x, y, t). \quad (2.33)$$

To obtain the return air flow  $f(x, y, t)$ , first the offset and then the geometrical distortion must be removed by the geometrical correction. The remaining terms can be corrected regardless of the order.

### Offset Removal

The offset  $o(x, y, t)$  can be split into the mean pixel intensity offset per image  $o_{image}(t)$  and a remaining offset for each individual pixel  $o_{pixel}(x, y, t)$

$$o(x, y, t) = o_{image}(t) + o_{pixel}(x, y, t). \quad (2.34)$$

The remaining offset for each individual pixel  $o_{pixel}(x, y, t)$  can be linearized at the time zero by using the first two terms of it's Taylor series representation

$$o(x, y, t) = o_{image}(t) + o_{pixel}(x, y, t = 0) + \dot{o}_{pixel}(x, y, t = 0) \cdot \Delta t_{off} + \underbrace{O_{pixel}(\Delta t_{off}^2)}_{\approx 0}, \quad (2.35)$$

into the offset at the beginning of the measurement  $o_{pixel}(x, y, t = 0)$ , a time-dependent offset of  $\dot{o}_{pixel}(x, y, t)$  and higher order terms  $O_{pixel}(\Delta t_{off}^2)$ . The time which has passed since the last offset correction is called  $\Delta t_{off}$ . The higher order terms are not further considered. The mean pixel intensity offset per image  $o_{image}(t)$  can be split into the mean over the sequence  $o_{image,mean}(t)$  and the fluctuations from this mean for each individual image  $o_{image,fluc}(t)$ . This leads to

$$o(x, y, t) = o_{image,mean} + o_{image,fluc}(t) + o_{pixel}(x, y, t = 0) + \dot{o}_{pixel}(x, y, t = 0) \cdot \Delta t_{off}. \quad (2.36)$$

Before each measurement, the lens was covered with a tight lid and the detected offset was removed from the measurement data, hence removing  $o_{image,mean}$  and  $o_{pixel}(x, y, t = 0)$ . This offset correction also sets  $\Delta t_{off} = 0$ . The time-dependent offset per pixel  $\dot{o}_{pixel}(x, y, t)$  cannot be compensated but only minimized by minimizing  $\Delta t_{off}$  by frequent offset removals.

Mean fluctuations for each individual image from the mean of the sequence  $o_{image,fluc}(t)$  were detected. The intensity of these fluctuations are calculated by first calculating the mean pixel intensity of a large region of the image which is supposed to have a constant temperature over the full sequence of images. The difference from this value to the mean pixel intensity of the examined region over the full sequence is calculated. This value

represents the image intensity fluctuations of the region and can be represented by

$$\frac{\sum_{\forall x, \forall y} (o(x, y, t) - o(x, y, t = 0))}{n_{pixel}} \approx \frac{\sum_{\forall x \in region, \forall y \in region} (o(x, y, t) - o(x, y, t = 0))}{n_{pixel} \in region}. \quad (2.37)$$

The region that is chosen, is the part of the image containing the building of the STJ since no return air is present in this region. Therefore the temperature is supposed to be stable.

For each image the found offset  $o(x, y, t)$  is subtracted from every pixel.

### Geometrical Correction

Although the infrared camera was mounted on a stable tripod, slight shaking of the camera could occur due to the presence of wind. Since the distance between the infrared camera and the receiver is very long, this effect would need to be corrected if a sequence of images is analyzed. To do so, image stabilization based on cross-correlation was used. Due to the presence of strong noise, the images were matched using only the part of the image containing the receiver. A significant distortion due to a lens error was not detected.

### Background Removal

A true background image cannot be taken, since the receiver is in operation and the background image hence changes over time. It is the part of the measured intensity which corresponds to actually present but unwanted radiation. This includes all measured infrared radiation that does not originate from the return air flow. Three different approaches to remove the background  $b(x, y, t)$  were examined. These estimate the background  $b_{est}(x, y, t)$  with three different definitions. The estimated backgrounds  $b_{est}(x, y, t)$  are subtracted from the image with the assumption that  $b(x, y, t) = b_{est}(x, y, t)$ .

The first approach defines the background estimation for each image, to be the previously taken image:

$$b_{est}(x, y, t) = T^{-1}(g(x, y, t - \Delta t) - o(x, y, t - \Delta t)) - n(x, y, t - \Delta t), \quad (2.38)$$

whereby  $\Delta t$  is the time that passes between these subsequent images. This approach

does not result in directly visualizing the flow in front of the receiver  $f(x, y, t)$ , but instead highlights the regions in which the radiation of the flow has the largest gradients in pixel intensity over time. This is mainly caused by the overlap of the observed flow structures between two images.

A second option for background estimation is defined as the minimum of each individual pixel over the complete sequence which is examined. The maximum length of a sequence is limited by the length of the uninterrupted recording of images. This can be expressed as

$$b_{est}(x, y) = \min_{\forall t \in \text{sequence}} (T^{-1}(g(x, y, t) - o(x, y, t)) - \mathbf{n}(x, y, t)). \quad (2.39)$$

This is a good estimation of the background, because the flow can be clearly seen without being distorted. Since the minimum has been chosen,  $b_{est}$  is an underestimation of the background. This background estimation is not time-dependent. It can however be expected that the background will change over time due to temperature changes of the background over the sequence. Therefore a time-dependent background estimation is defined as

$$b_{est}(x, y, t) = \min_{\forall t \in [(t-20\Delta t), (t+20\Delta t)]} (T^{-1}(g(x, y, t) - o(x, y, t)) - \mathbf{n}(x, y, t)). \quad (2.40)$$

This background estimation represents a moving minimum which is calculated for the previous and following 20 images. Because the flow in front of the receiver is turbulent, it can be assumed, that within the time span of these 41 images, the minimum of each pixel is caused by the absence of flow. This should leave only the visualization of the return air flow in  $f(x, y, t)$ . This method of background removal was chosen for the return air visualization at the STJ, since it resulted in the best signal to noise ratio of the return air flow. The number of images used for the background estimation was chosen based on the quality of the resulting flow visualization. The removed background further lacked any structure of the return air flow, underpinning its validity.

### Noise Removal

To remove the noise  $\mathbf{n}(x, y, t)$  of the image most effectively, various filters have been tested. Their effectiveness has been tested by visual quality of the resulting flow visualization. The removed noise should be of maximum amplitude and should lack significant structure. Table 2.4 shows an overview of the most common filters and their method of filtering. Shao et al. (2014) describe the three dimensional block matching algorithm (BM3D) as

the state of the art. It has been found superior for our application by comparison to the filters shown in Table 2.4.

The chosen BM3D processes the noisy input image by successively extracting reference blocks from it. For each block similar blocks within the image are found and stacked together into a group. The filtering of the group is conducted, and the estimates of the grouped blocks are returned to their original locations. After processing all reference blocks, the obtained block estimates can overlap. This could cause multiple estimates for each pixel. These estimates are aggregated to form an estimate of the whole image. This general procedure is implemented in two different forms to compose a two-step algorithm. (Dabov et al., 2007)

After smoothing the image, only the temperature changes due to the flow should be left. This image is a two dimensional integral projection of the three dimensional flow. This is the result of the IIT. This image can be used to examine the flow pattern. It can also be further investigated using the Infrared Image Velocimetry, which is described in the following section.

### **Application of Signal Processing**

The signal processing steps of the recorded data are exemplary shown in Fig. 2.15. The images were taken from ground level at a distance of around 60 m of the Testreceiver. The left image shows the raw infrared data without post processing. After the background and the offset is subtracted, the flow in front of the receiver can be identified for the first time. By applying a BM3D video filter, the noise of the image is reduced. Furthermore, by adapting the color map of the image the flow visualization can be further enhanced. The output after these steps can be seen in the right image.

### **2.3.3 Infrared Image Velocimetry (IRIV)**

Having visualized the return air flow, it would be valuable if a velocity field could be extracted from this data. In Particle Image Velocimetry (PIV), particles are introduced into the system and two images in rapid succession are taken. From the position of the particles, their movement and velocity can be estimated. From this data a velocity vector field can be calculated. Seedless velocimetry measurements in contrast require



Table 2.4: The different filters which were compared to the BM3D filter and their method of filtering.

Name of Filter	Method of Filtering	Literature
Anisotropic Diffusion	Application of the law of diffusion on pixel intensities, whereby the diffusion coefficient is dependent on the direction of the gradient.	(Perona and Malik, 1990)
Bayes	Treating images as probability-frequency functions and applying Bayes' theorem.	(Richardson, 1972)
Gauß	Smoothing of the image noise by averaging with sigma threshold.	(Lee, 1983)
Isotropic Diffusion	Application of the law of diffusion on pixel intensities.	(Perona and Malik, 1990)
Median	The image is constructed out of median values of neighboring pixels.	(Brownrigg, 1984)
Moving Average	The average for a certain number of images, previous or after the current image.	-
Non Local Mean	Mean of all pixels with weight depending on pixel similarity.	(Buades et al., 2005)
Wavelets	Employment of thresholding in the wavelet transform domain.	(Donoho and Johnstone, 1994)
Wiener	Least squares filter based on the local mean and variance of the neighborhood of the central pixel.	(Bovik, 2010)
BM3D	as described in text	(Dabov et al., 2007)

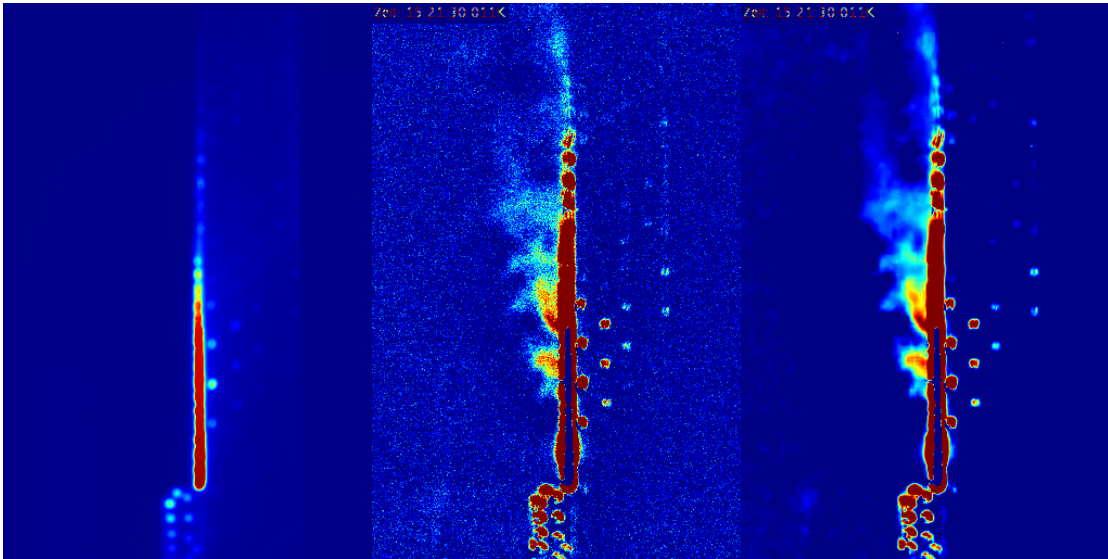


Figure 2.15: The signal processing of the IIT is shown for a sample image of the Testreceiver at the STJ. The left image is the raw image. From it the background and offset is subtracted to yield the central image. The result of the noise removal can be seen on the right. The position of the viewing area of these IIT images is shown in Fig. 4.16. Based on Tiddens et al. (2017a).

no particles. In Schlieren image velocimetry for example, “turbulent eddies can serve as the PIV particles in a Schlieren image or shadow gram. The PIV software analyzes motion between consecutive Schlieren or shadow graph frames to obtain velocity fields” (Jonassen et al., 2006).

The same methodology can be applied to the result of the IIT and is called Infrared Image Velocimetry (IRIV). The IRIV is currently being patented. (Tiddens and Röger, 2015) The prerequisite of a high Reynolds number is given for the air flow in front of the receiver of the STJ. (Maldonado Quinto, 2016) Therefore IRIV should be applicable, using turbulent eddies as PIV particle replacements.

The processing of the data is conducted using PIVlab, a MATLAB toolbox by Thielicke and Stamhuis (2014). Within this framework, the data is processed following the proceeding steps. First, the images are preprocessed. This is followed by the image evaluation and post processing. The used preprocessing uses the full intensity scale by applying “contrast limited adaptive histogram equalization”. (Reza, 2004) Furthermore an intensity capping was applied, to compensate for the bright spots within the area to the correlation signal.

The image evaluation is the step where the actual velocity information is generated. The velocity information is derived by cross correlating small parts a pair of images to obtain the most probable particle displacement in the interrogation areas. Cross-correlation is a statistical pattern matching technique. It is used to find particle patterns from the interrogation area of the first image (A) in an interrogation area of the second image (B). Since a discrete number of pixels is used, this can be expressed by the discrete cross correlation function.

Due to a small amount of flow information within each image, a large number of images has to be examined for a reasonable velocity estimation. The easiest approach of solving the discrete cross correlation function has a high computational cost. Therefore the cross correlation is derived in the frequency spectrum reducing these computational cost. This is realized using a Discrete Fourier Transformation. To reduce the influence of noise on the signal, several passes of the Discrete Fourier Transformation on the same dataset are run, whereby the integer result of the first analysis pass is used to offset the interrogation area in the following passes. The loss of information due to particle displacement is hence minimized. We apply a Gaussian peak finding method to the data. As shown in Fig. 2.16 this allows a sub pixel maximum detection. This is especially important for our application since dealing with a low resolution due to the use of infrared camera data. Since dealing with a two-dimensional correlation matrix, the integer intensity distribution of this matrix is fitted for each axis independently.

Post processing of the data is required to obtain results and filter these results for noise. First, the maximum displacement is determined manually. All vectors that exceed this significantly are removed. A further basic method for filtering outliers can now be applied, by defining a threshold of a certain number of standard deviations from the mean. After the removal of outliers, missing vectors are replaced by interpolated data. The data is finally averaged over the full recorded sequence to obtain a mean flow field. A more detailed description of the individual steps can be found in (Thielicke and Stamhuis, 2014).

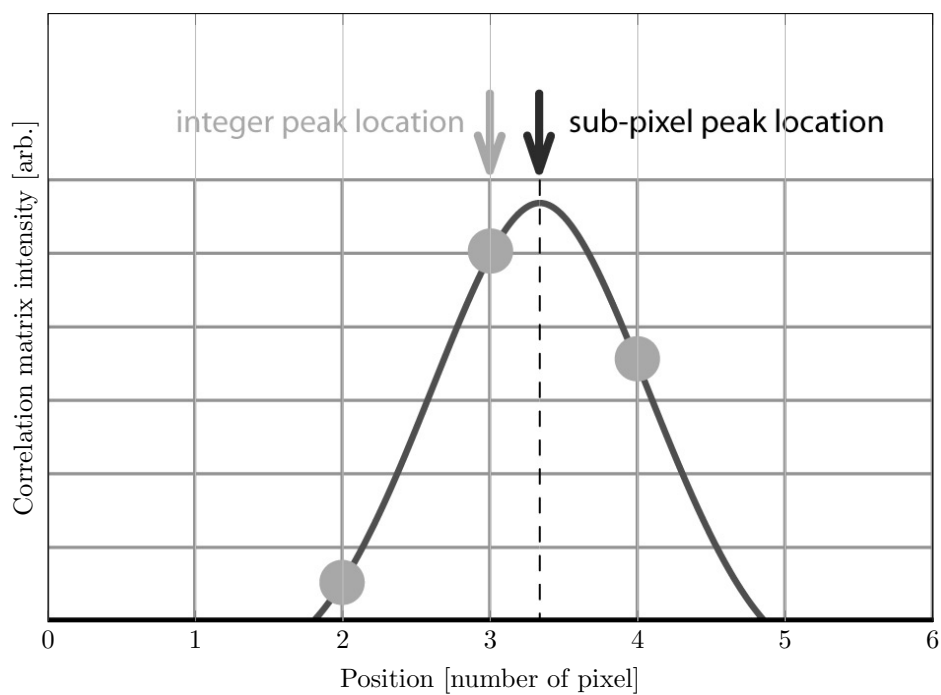


Figure 2.16: An exemplary measured correlation matrix intensity (dots) is shown for one dimension, being fitted with Gaussian function (solid line). This is done for both axes independently, resulting in a peak location determination of sub pixel precision. Based on Thielicke and Stamhuis (2014)

## 3 Setup

*"Duct tape is magic and should be worshiped."*

— Andy Weir, *The Martian*

The three environments which have been used for measurements and validations, are described in this chapter. First the receiver model is covered, which has been constructed to develop and validate the ARR measurements. The research platform at the STJ is only dealt with regarding the return air visualization (see table 1.2). Finally the main receiver of the STJ and the measurement setup for ARR as well as the return air visualizations are found in the last section.

### 3.1 Receiver Model

A model of a part of an open volumetric receiver has been built to develop, test and validate the measurement method without solar irradiation. It is a model of the open volumetric receiver containing 9 x 6 absorber modules at a scale of 1:2. A photo of the receiver is shown in Fig. 3.1.

The air is sucked through the receiver (6) by a fan (10) and is then returned to the receiver front through 13 air return tubes (8). The model is designed in consideration of the theory of similarity, to produce a flow pattern in front of the receiver which is physically similar to the one at the STJ. Due to the smaller size, modifications to the air circuit are simpler than at the full scale solar power plant. The fan can be operated at different frequencies to control the air mass flow. The air mass flow is measured by a thermal mass flow sensor in order to enable the measurements with different air mass flow rates (5). The receiver can be covered by a removable lid (7) to test for unwanted leaks.

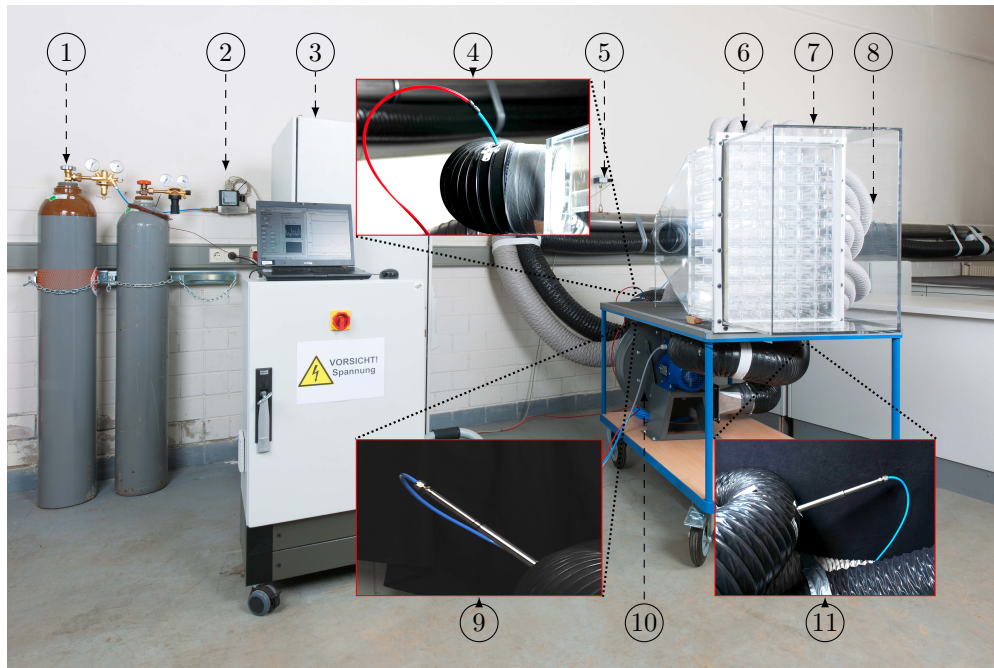


Figure 3.1: Photo of the measurement setup, showing: (1)helium, (2)mass flow controller, (3)mass spectrometer, (4)helium injection, (5)air mass flow meter, (6)receiver, (7)removable lid, (8)air return tubes, (9)measuring point 1, (10)fan, (11)measuring point 2. Based on Tiddens et al. (2016b).

By closing the receiver and removing some of the 13 return air tubes, different scenarios with fixed, unknown ARR values can be created for validation purposes (sec. 4.2.2).

To conduct a tracer gas measurement, helium (1) is injected into the system (4). The helium mass flow is controlled using a mass flow controller (2). The resulting helium mole fraction can be measured by extracting a sample at both measuring points (9), (11). Due to the choice of helium as tracer gas (see sec. 2.1.1) and the low mole fractions that need to be measured, a quadrupole mass spectrometer (QMS 200, Pfeiffer Vacuum) (3) is used to determine the mole fraction. Figure 3.2 shows a closer view of the receiver with a closed front and all 13 return tubes attached. These tubes can be removed in order to allow smaller ARR values.

To sample the molar fraction of the air stream at various radial positions with a 1 cm resolution, the measuring probe shown in Fig. 3.3 was constructed. The probe was designed to permit precise changes of the position of measurement during operation. This can be achieved without opening the air circuit. It reduced the required time



Figure 3.2: Photo of the receiver model with a closed front and all 13 return tubes attached (Tiddens et al., 2016b).

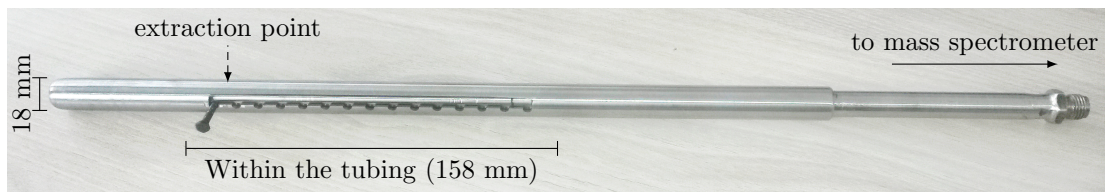


Figure 3.3: Photo of one of the measuring probe used at the receiver model sampling the helium mole fraction at discrete points of the cross section of the piping to obtain the spatial distribution.

and improved repeatability significantly. This measuring probe was furthermore the prototype of the probe used at the STJ shown in Fig. 3.10.

## 3.2 Solar Tower Juelich

The Solar Thermal Test and Demonstration Power Plant Juelich (STJ) was built as a demonstration as well as research power plant in 2008 by a consortium consisting of the German Aerospace Center (DLR), Solar-Institute Juelich, Kraftanlagen München GmbH and Stadtwerke Jülich. It was taken over by the DLR in 2011. (Koll et al., 2009)

A photo of the 60 meters high solar power tower, showing both the main receiver at the

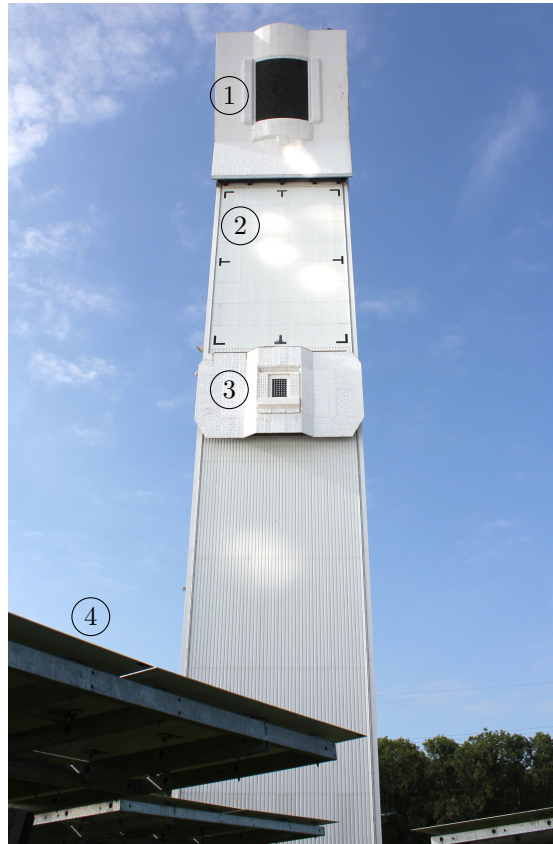


Figure 3.4: Photo of the STJ displaying the main receiver (1) at the top, the target for the calibration of heliostats (2), the Testreceiver (3) and the heliostats (4) at ground level. Based on Tiddens et al. (2017b).

top (1) and the Testreceiver (3) is depicted in Fig. 3.4. The main and the Testreceiver can be irradiated by reflecting and concentrating sunlight utilizing an array of 2153 heliostats. The heliostats make up a combined total surface of nearly 18000 m<sup>2</sup>. (Funken, 2013) The back structure of the heliostats can be seen in (4). Furthermore the ultrasonic anemometer (Thies, Ultrasonic Anemometer 3D) on the roof of the solar tower is used to collect wind data. The research platform and the main receiver are described in the following two sections, respectively.

### 3.2.1 Research Platform

The research platform is a 80 m<sup>2</sup> large laboratory located at 26 m height within the STJ. Allowing a maximum power of about 1400 kW at its design point (solar noon, March 21,



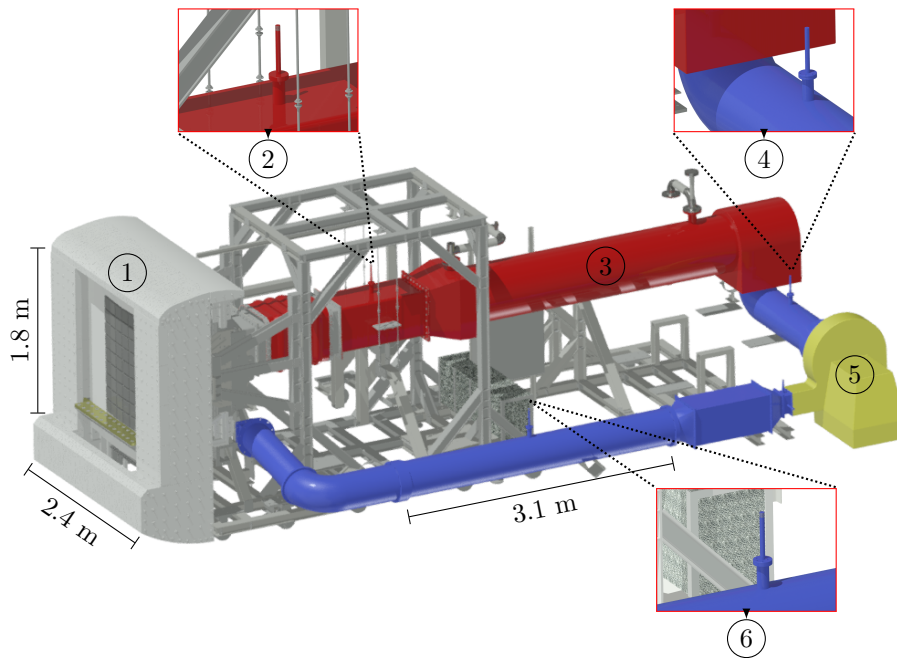


Figure 3.5: The research platform of the STJ with the solar receiver (1), two gas measuring point (2,6), the gas cooler (3), the injection point (4) and the blower (5).

DNI = 850 W/m<sup>2</sup>), it is suitable to perform large-scale radiation experiments. (Göhring et al., 2009; Feckler et al., 2015)

Our experiments were conducted using the so called Testreceiver with an irradiation of around 500 kW. The measurements were conducted during performance tests of 54 metallic absorber modules by Feckler et al. (2015). Figure 3.5 shows a schematic of the Testreceiver with measuring points (2,6) and the injection point of helium (4). Air is sucked in using a fan (5) through the irradiated receiver (1). The air is cooled down in the gas cooler (3) before passing the fan and being returned through the structure of the receiver. The mass flow was measured using differential pressure flow meter (McCrometer, V-Cone). The temperature of the return air is measured by averaging the temperatures of five type K thermocouples.

The carbon dioxide tracer was injected in front of the fan (4) to achieve a good mixing of the carbon dioxide within the return air. Figure 3.6 shows a front and a side view photo of the research platform with the Testreceiver in operational position. The return air visualizations were performed using a mid-wavelength infrared camera (InfraTec,

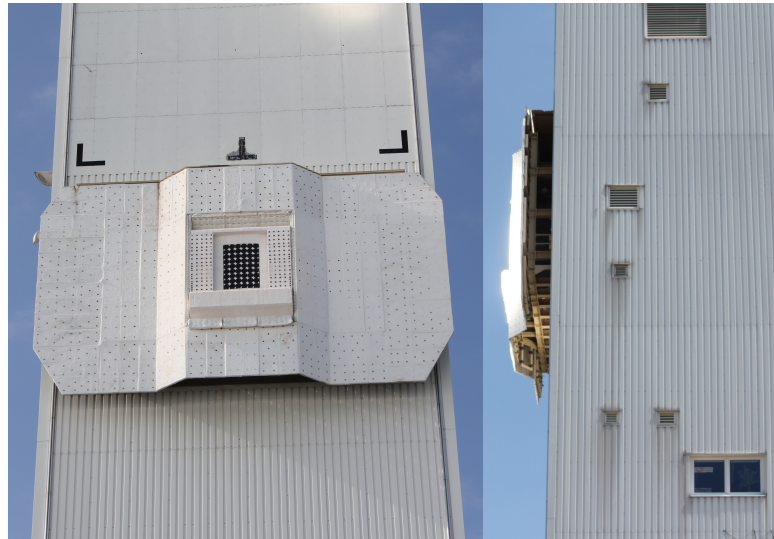


Figure 3.6: Photo of the research platform of the STJ from front and side perspective. Tiddens et al. (2017b)

ImageIR 8380). The camera is cooled by a Stirling motor. This allows a high thermal resolution (better than 20 mK). The infrared measurements were conducted using a bandpass filter at  $4.24 \mu\text{m}$  to increase the signal to noise ratio. The filter has a full width at half maximum of  $0.2 \mu\text{m}$ . The camera was placed at ground level with a distance of around 60 m to the Testreceiver.

### 3.2.2 Main Receiver, Power Block and Storage

The main receiver consists of 1080 ceramic absorber modules with an overall surface area of around  $22 \text{m}^2$  and is heated by concentrated sunlight. Air is sucked in through these hot modules and is heated to a temperature of about  $680^\circ\text{C}$ . The hot air is either transported to the thermal storage system consisting of a large vessel filled with porous ceramic bricks or directly to the steam boiler. Here steam is generated in a heating tube boiler to drive a turbine and produce electricity. (Koll et al., 2009) Having passed the heat storage or the steam boiler, the air is returned to the front of the receiver. There it is blown out through the gaps between the absorber modules. This can be seen schematically in Fig. 1.5. Before being sucked in again, a fraction of the return air is lost and replaced by ambient air. The functionality of the STJ is summarized in a schematic in Fig. 3.7.

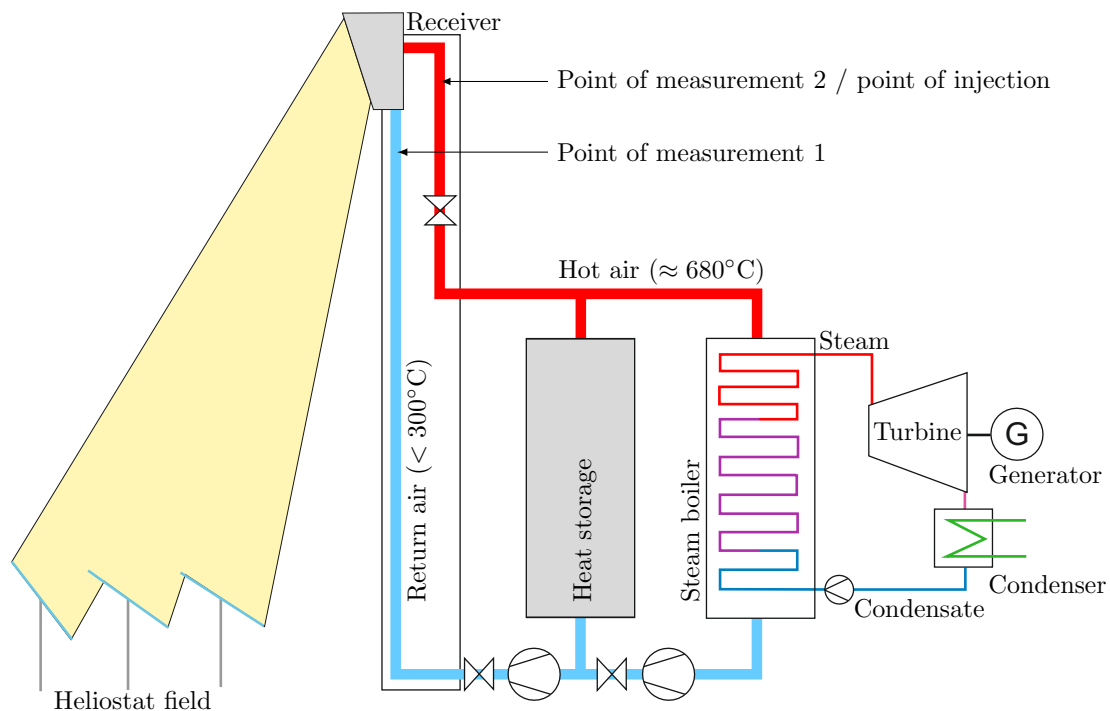


Figure 3.7: Schematic of the STJ. The receiver is heated by a field of heliostats. Air is sucked through the receiver, heating up to about  $680^{\circ}\text{C}$  and used to drive a water steam cycle or is stored in a thermal storage. The still warm air ( $< 300^{\circ}\text{C}$ ) is returned to the receiver for efficiency purposes. The location of the measuring points and helium injection for the tracergas method are indicated. Based on Funken (2013).

A photo of the main receiver is shown in Fig. 3.8. The main receiver has the shape of a section of a cylinder which stands in contrast to the flat Testreceiver. It is furthermore inclined downwards towards the heliostats. The STJ has been operated for the experiments in a mass flow controlled mode. The mass flow is measured using an ultrasonic flow meter (GE Sensing, Digital Flow) and the speed of the fan is controlled. Since mainly designed for research, the temperature is measured at a multitude of locations in the STJ using thermocouples.

To extract gas samples out of the air circuit of the STJ, probes have been constructed and built. This allows the measurement of the helium distribution along the cross section of the piping as described in Section 2.1.2. The probe at measuring point 2 which also incorporates the injection of helium is shown in Fig. 3.9. By moving the inner probe within the support structure, a sample can be extracted towards the mass spectrometer at discrete locations along the cross section of the piping of the STJ. The probe in



Figure 3.8: Photos of the main receiver of STJ from front and side perspective. The active absorber surface consists of 1080 absorber modules (1), surrounded by an irradiation shield (2). The modularity of the receiver can be seen in Fig. 1.2. At the sides and underneath the absorber there are outlets of the external air return system (3). Based on Tiddens et al. (2017b).

Fig. 3.9 can be seen in an assembled state (red probe) within the piping of the STJ in Fig. 3.10. The probes allow the sampling of the air/helium mixture with 30 discrete measurement locations along the cross section for each of the two measuring point. The location of extraction can be changed during operation of the power plant. The helium injection was also realized at this measuring point, facing away from the extraction probes in the direction of the air flow. To reduce construction costs, the probes were introduced at a point where flanges already existed. Since these were previously used to measure the temperature, the designed probes contain mounts for the previously installed thermocouples (4), too. The insulation of the piping is not shown.

A photo of the installed probes can be seen in Fig. 3.11 taken from the inside of the piping. In the background the splitting of the air stream towards either storage or steam boiler can be seen. A more detailed description of the measuring probes can be found in (Braemer, 2014).

An external air return system was recently implemented in order to reduce parasitic losses due to high pressure losses and increase efficiency at the STJ. Hereby a fraction of the return air can be diverted to the sides and the bottom of the receiver, instead of being blown out through the gaps between the 1080 absorber modules. The outlets of the external air return can be seen in Fig. 3.8.

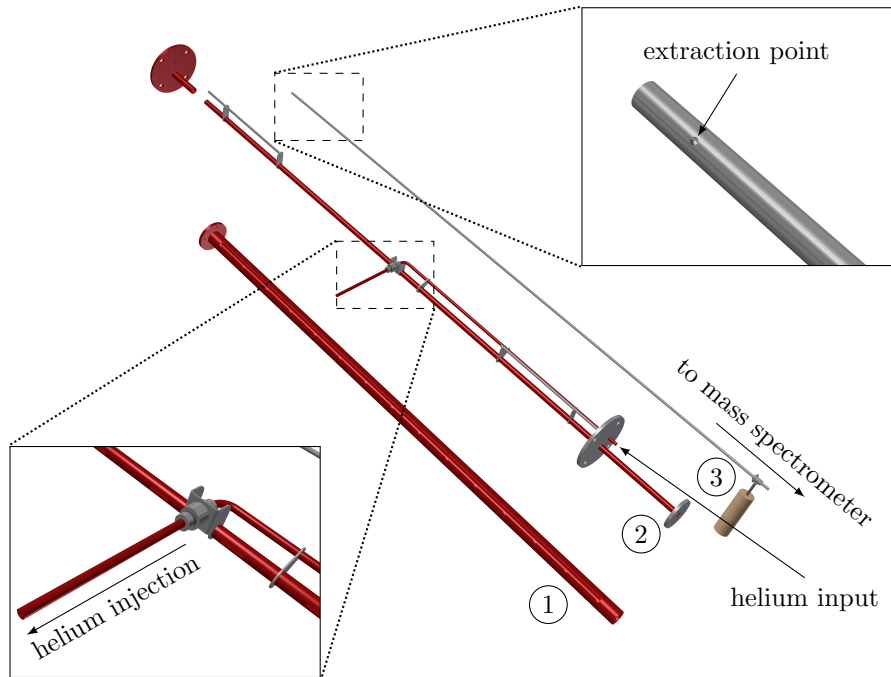


Figure 3.9: Schematic of the measurement probe of the measuring point 2 which incorporates the injection of helium. Showing the inner probe (1) which is held in place by the support structure (2,3). By moving the inner probe within the support structure, a sample can be extracted towards the mass spectrometer at discrete locations along the cross section of the piping of the STJ. Based on Tiddens et al. (2017b).

The infrared measurements for the IIT and IRIV methods were conducted with the same camera and filter setup as displayed in Section 3.2.1. The measurements were executed from ground level with a distance of the main receiver of about 110 m. The carbon dioxide gas for IIT was injected into the air circuit at measuring point 2. The tracer was not induced through the injection point but through an extraction probe that was not used for tracer gas measurements at the time.

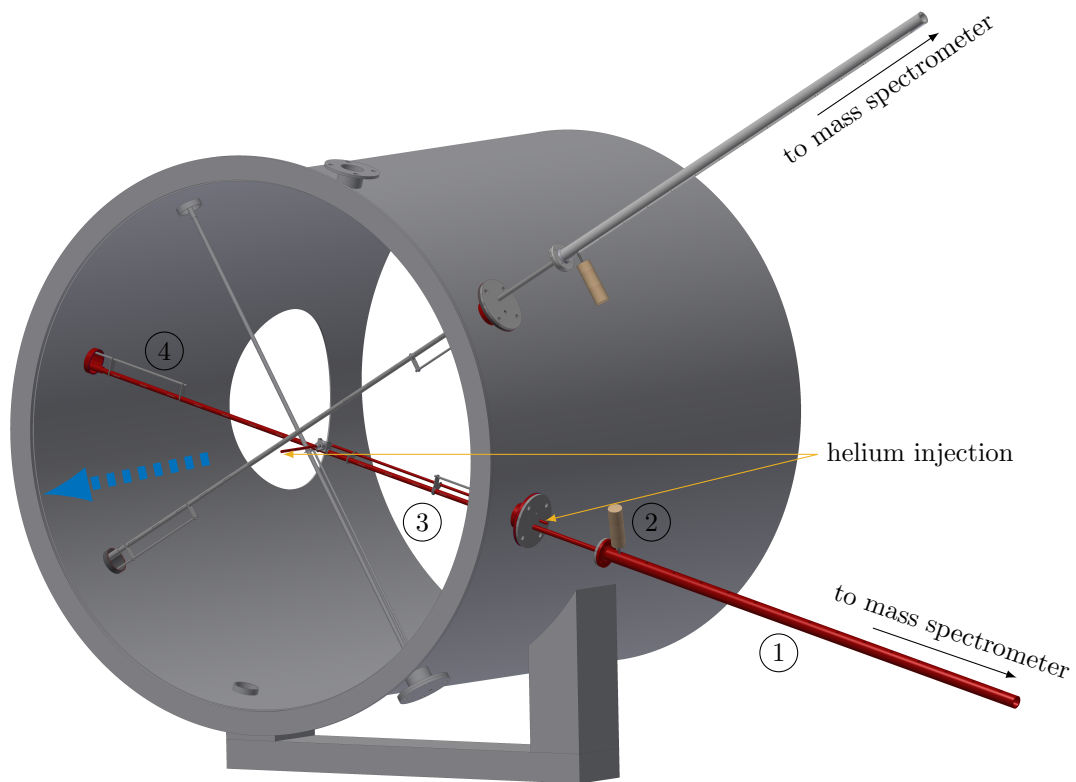


Figure 3.10: Schematic of the measuring point 2, with two measurement probes. The inner probes (1) are held in place by the support structure (2,3). By moving the inner probe within the support structure, a sample can be extracted towards the mass spectrometer at 15 discrete locations along the cross section of the piping of the STJ. The red probe (see Fig. 3.9) incorporates the injection of helium, which is facing downstream (blue arrow) to not influence the extracted probes. The designed probes furthermore contain mounts for the previously installed thermocouples (4). Based on Tiddens et al. (2017b).



Figure 3.11: Photo of the of the measuring point directly behind the receiver. The photo was taken from the inside of the piping at the STJ. The direction of air flow follows the line of sight. In the background the splitting towards emergency vent, storage and steam boiler (left to right) can be seen.





## 4 Results

*"The Answer to the great Question... of Life, the Universe and Everything... is... forty-two."*

— Douglas Adams, *The Hitchhiker's Guide to the Galaxy*

This chapter contains the results of the ARR measurements with both the dynamic and the numeric method at the STJ as well as all necessary validation measurements. This includes the validation of the dynamic measurement method and the static method at the receiver model with one another. The validation of the numeric method with the dynamic method is conducted at the STJ. The last section covers the results of the return air visualization applying both IIT and IRIV to the two receivers of the STJ.

### 4.1 Static ARR Measurements

Although the static method is not applicable at the STJ, it is crucial for the validation of the dynamic method at the receiver model. This section presents static ARR measurement results at the receiver model. The application of which is used in Section 4.2.2 for the validation of the dynamic method.

#### 4.1.1 Static Measurements at the Receiver Model

The most important prerequisite of the static measurement is that at both point sampling at the measuring points is possible. Therefore, the homogeneity of the helium tracer within the piping is measured.

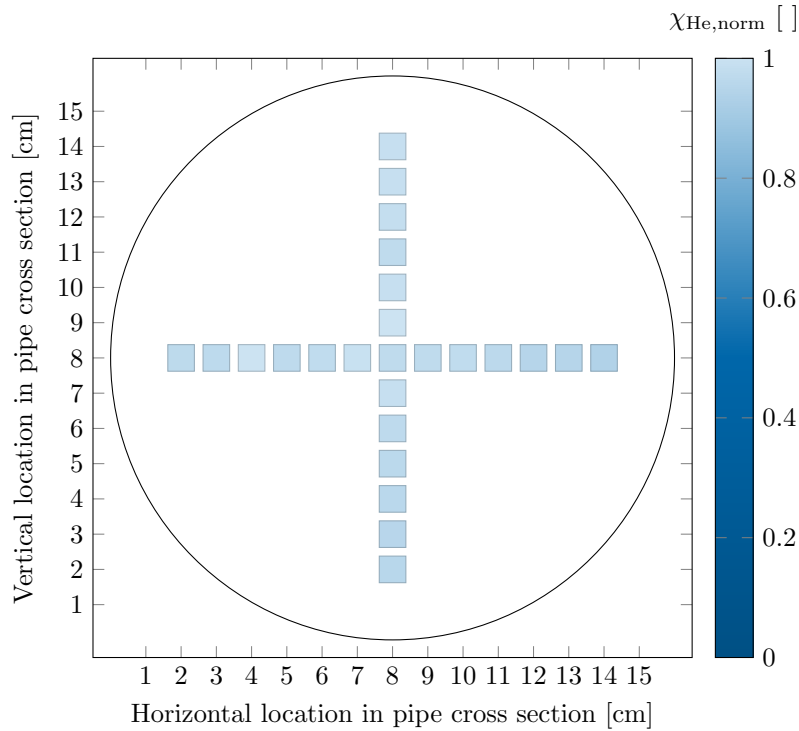


Figure 4.1: The helium mole fraction across the piping of the receiver model at measuring point 2 (see Fig. 3.1) is homogeneously distributed. The measurements show only small fluctuations with a standard deviation of 1.6%. Based on Tiddens et al. (2016b).

### Mixing

The helium mole fraction was measured at a total of 26 sampling points (see Fig. 3.3) within the piping (length  $\approx 27$  m, cross section = 0.16 meter) at both measuring points. The result of an exemplary measurement at measuring point 2 is shown in Fig. 4.1. At these the helium mole fraction is homogeneously distributed along the cross section of the piping. The measurements show only small fluctuations with a standard deviation of 1.6%. A central extraction point represents therefore the mean value over the cross section area. Hence single point sampling is possible.

### Corrections

The background mole fraction of helium in the ambient air is subtracted from the data (Eq. 2.5). This mole fraction can be higher in the laboratory environment of the

receiver model than in ambient air ( $\approx 5.2$  ppm) since helium is blown out into the lab. Without counteractions the background helium mole fraction increased to 200 ppm after 30 minutes of measurement. This is about 30 % of the minimum signal amplitude for ARR determination. This significant background changes over time, increasing the complexity of the data evaluation. To eliminate this problem, the background helium mole fraction was kept below 20 ppm by opening large doors and a skylight in the laboratory.

A peripheral leak between the two measuring points could not be observed after optimizing the sealing. Therefore no peripheral leakage correction was introduced for the static measurement at the receiver model. Since the static measurement is furthermore conducted at equilibrium a diffusion correction has not been considered.

### Sensitivity Analysis

A sensitivity analysis is conducted to examine if variables have a distorting effect on the measurement. The static measurements at the receiver model were executed with two levels of helium injection ( $25 \text{ std l/min}$ ,  $50 \text{ std l/min}$ ), since a dependency on the tracer mole fraction would be troublesome. The results of both mole fractions however lie well within the uncertainty of the measurement, therefore the helium mole fraction is not a significant factor. It can be seen that the uncertainty depends on the injected helium amount for the static method. This is expected, since an increase in helium mole fraction increases the signal to noise ratio of the measured signal. For the case of 8 of 13 attached air return tubes an increase from  $25 \text{ std l/min}$  to  $50 \text{ std l/min}$  helium injection reduced the measurement uncertainty from 4.1 % to 2.5 %. The ambient temperature, ambient air pressure and small variations in the air mass flow had no significant influence on the results and were not further examined.

### Results

Measurements at the model were conducted with an air mass flow of  $\dot{m}_{out} = (0.247 \pm 0.008) \text{ kg/s}$ . The mass flow measurement was executed without helium present, since the measurement system was calibrated for pure air.

After the mole fraction reaches equilibrium, the measuring point is switched every two

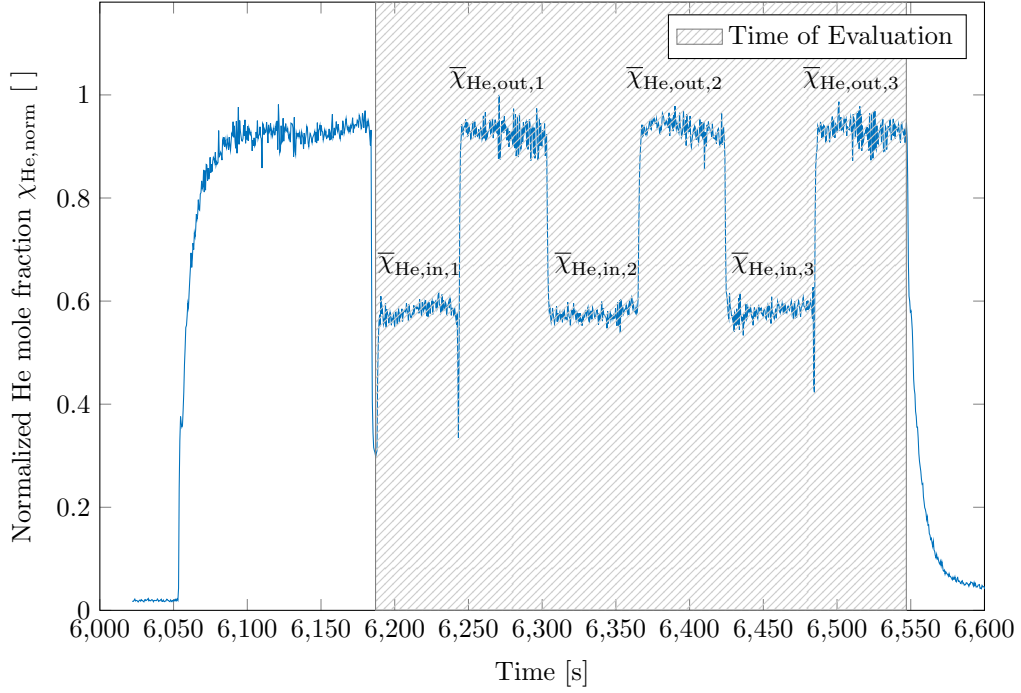


Figure 4.2: The figure shows the normalized raw data of a helium injection of 50 std l/min for the static method with 8 of 13 attached air return tubes. Based on Tiddens et al. (2016b)

minutes between point 1 and 2 (see Fig. 2.1). In Fig. 4.2 the normalized mole fraction data of an exemplary measurement is shown for the case of 8 of 13 attached air return tubes. The ARR is calculated according to Eq. 2.5

$$ARR_{\text{meas, stat}} = \frac{\chi_{\text{He, in}} - \chi_{\text{He, amb}}}{\chi_{\text{He, out}} - \chi_{\text{He, amb}}}$$

which leads to

$$ARR_{\text{meas, stat}} = \frac{1}{5} \cdot \left( \frac{\bar{\chi}_{\text{He, in, 1}} - \chi_{\text{He, amb}}}{\bar{\chi}_{\text{He, out, 1}} - \chi_{\text{He, amb}}} + \frac{\bar{\chi}_{\text{He, in, 2}} - \chi_{\text{He, amb}}}{\bar{\chi}_{\text{He, out, 1}} - \chi_{\text{He, amb}}} + \frac{\bar{\chi}_{\text{He, in, 2}} - \chi_{\text{He, amb}}}{\bar{\chi}_{\text{He, out, 2}} - \chi_{\text{He, amb}}} + \frac{\bar{\chi}_{\text{He, in, 3}} - \chi_{\text{He, amb}}}{\bar{\chi}_{\text{He, out, 2}} - \chi_{\text{He, amb}}} + \frac{\bar{\chi}_{\text{He, in, 3}} - \chi_{\text{He, amb}}}{\bar{\chi}_{\text{He, out, 3}} - \chi_{\text{He, amb}}} \right) \quad (4.1)$$

for this particularity measurement. The ARR has been calculated to be  $ARR_{\text{meas, stat}} = (62.2 \pm 2.5)\%$ . Further static measurements are conducted for the validation of the dynamic measurement in Section 4.2.2.

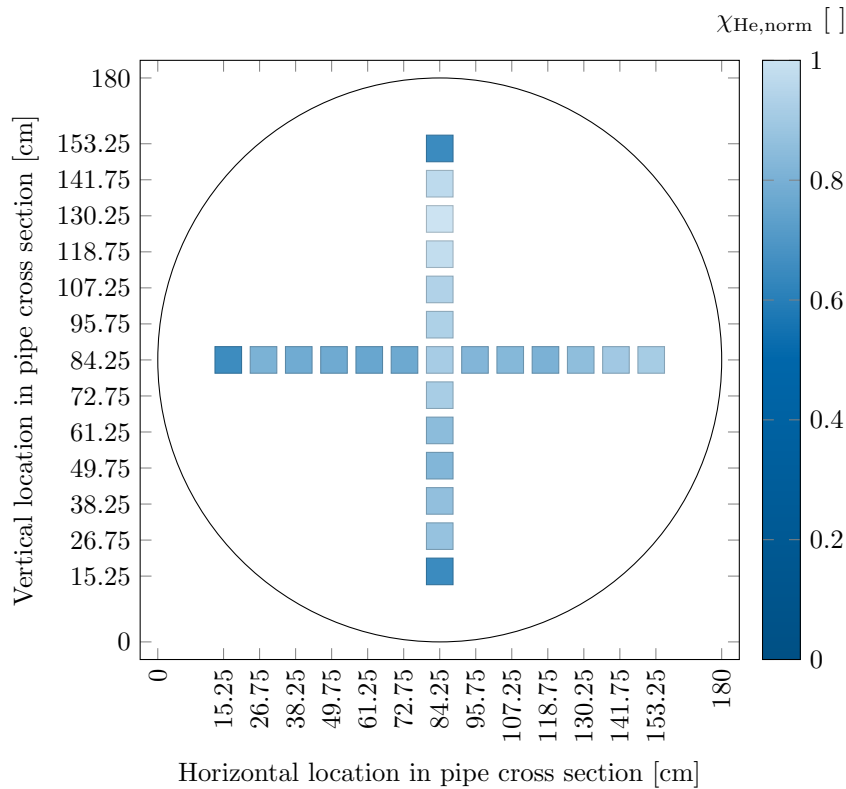


Figure 4.3: The helium mole fraction across the piping of the STJ at measuring point 2, directly behind the receiver. The measurements show large fluctuations, with an standard deviation of 9.7%. This inhibits single point measurements.

#### 4.1.2 Static Measurements at the Solar Tower Juelich

To investigate if the static measurement is applicable at the STJ, the mixing of the tracer must be examined at both measuring points. A low fluctuation along the cross section of the piping is required to allow point sampling of the helium mole fraction  $\chi_{\text{He}}$  (see Section 4.1.1). As can be seen in Fig. 4.3, the measurements show large fluctuations, with an standard deviation of 9.7%. The static measurement however requires a homogeneous helium distribution across the piping, and hence cannot be applied at the STJ. The previously covered measurement (see Section 4.1.1) is however used at the receiver model to validate the dynamic method, which is described in Section 4.2.2.

## 4.2 Dynamic ARR Measurements

Before the results of the dynamic measurement method can be trusted it must be validated. This is covered within the first two parts of this section. The validation is carried out at the receiver model in order to be able to apply the dynamic measurement at the STJ. The results of the measurement at the STJ are covered at the end of this section.

### 4.2.1 Dynamic Measurements at the Receiver Model

The uncorrected ARR must first be measured before the occurring errors can be corrected. Since the dynamic measurements at the receiver model are conducted with very short circulation periods, the most important correction is that of the dynamic error. The different evaluation steps are shown for a helium injection of 50 stdl/min and 8 of 13 attached air return tubes. This exemplary measurement was executed with a mass flow of  $\dot{m} = (0.247 \pm 0.008) \text{ kg/s}$ .

#### Circulation Period

The circulation period  $T_{\text{circ}}$  must be measured before  $ARR_{\text{fit}}$  can be determined. The helium mole fraction response due to the injection of two short helium peaks is shown in Fig. 4.4. Each peak passes the measuring point four times, before the peaks become indistinguishable. The time between two peaks after the injection of a short helium peak is the circulation period  $T_{\text{circ}}$ , marked in red. The circulation period of the exemplary measurement has been determined by injecting five short helium peaks and averaging the indicated circulation periods, resulting in  $T_{\text{circ}} = (3.8 \pm 0.1) \text{ s}$ .

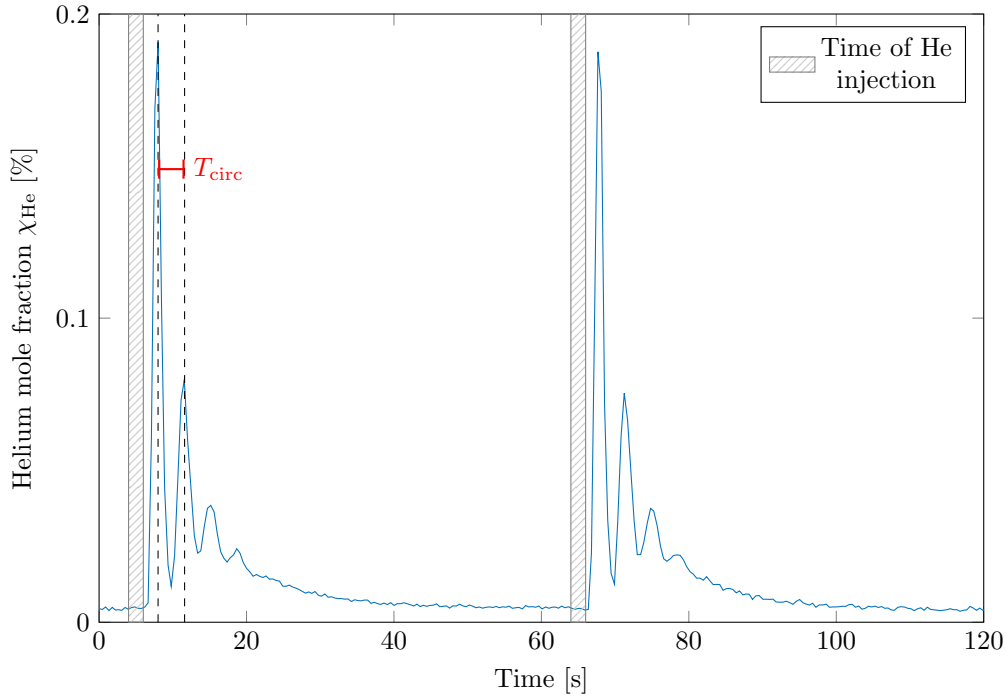


Figure 4.4: The helium mole fraction response due to the injection of two short helium peaks is shown. Each peak passes the measuring point four times, before the peaks become indistinguishable. The time between two peaks is the circulation period  $T_{\text{circ}}$ , marked in red. Based on Tiddens et al. (2016b).

### Uncorrected Air Return Ratio Measurement

Having found the circulation period  $T_{\text{circ}}$ ,  $ARR_{\text{fit}}$  can be determined by fitting Eqs. 2.17 and 2.19

$$\begin{aligned}\chi_{\text{He,fit,leading}}(t) &= 1 - (ARR_{\text{fit,leading}})^{t/T_{\text{circ}}} \\ \chi_{\text{He,fit,trailing}}(t) &= (ARR_{\text{fit,trailing}})^{t/T_{\text{circ}}}\end{aligned}\quad (4.2)$$

to the measured data.  $ARR_{\text{fit}}$  is calculated by averaging over the leading ( $ARR_{\text{fit,leading}}$ ) and the trailing edge ( $ARR_{\text{fit,trailing}}$ ). Having found  $ARR_{\text{fit}}$ , the corrected  $ARR_{\text{meas,dyn}}$  can be found by applying all necessary corrections.

The raw data of the measurement is shown in Fig. 4.5. The uncorrected  $ARR_{\text{fit}}$  was found to be  $(62.5 \pm 2.5)\%$ . Having found the uncorrected ARR, corrections due to peripheral leakage, diffusion background and dynamic error must be considered and if

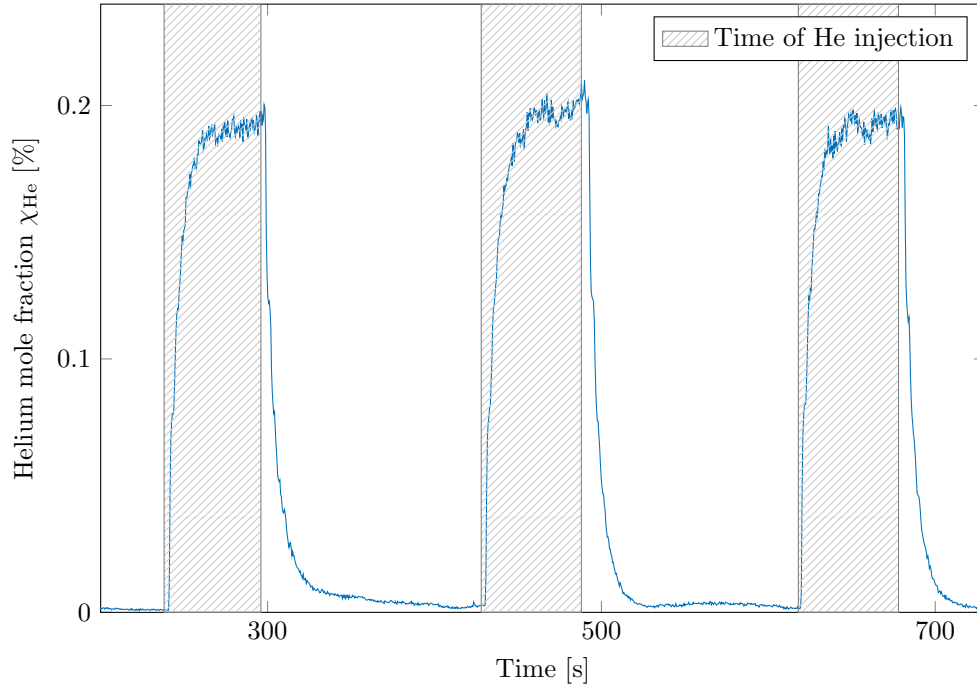


Figure 4.5: The helium mole fraction response due to the injection of three long helium peaks is shown. Based on Tiddens et al. (2016b).

necessary applied.

### Error corrections

According to Eq. 2.24, the corrected  $ARR_{\text{meas,dyn}}$  can be found by applying the peripheral leak and dynamic correction to the uncorrected  $ARR_{\text{fit}}$ ,

$$ARR_{\text{meas,dyn}} = ARR_{\text{fit}} \cdot cor_{\text{dyn}} \cdot cor_{\text{peri}} \cdot$$

For the exemplary measurement the peripheral leak correction was found to be  $cor_{\text{peri}} = (1.025 \pm 0.003) \%$  and the dynamic correction  $cor_{\text{dyn}} = (0.968 \pm 0.015)$ . The corrected ARR is calculated to be  $ARR_{\text{meas,dyn}} = (61.9 \pm 2.7) \%$ .



Table 4.1: The table shows exemplary results for both measurement methods at the receiver model. These measurements have been performed with a helium injection of 50 std l/min and with 8 of 13 attached air return tubes. The presented variable uncertainty is given with a 95 % level of confidence.

	Method		Uncertainty type
	Static	Dynamic	
$ARR_{\text{fit}}$	$(62.2 \pm 3.1)\%$	$(62.4 \pm 2.5)\%$	A/B
$cor_{\text{peri}}$	-	$(1.025 \pm 0.003)$	A
$T_{\text{circ}}$	-	$(3.8 \pm 0.1)s$	A
$cor_{\text{dyn}}$	-	$(0.968 \pm 0.015)$	A
<b><math>ARR_{\text{meas}}</math></b>	$(62.2 \pm 3.1)\%$	$(61.9 \pm 2.7)\%$	A/B

#### 4.2.2 Validation of the Dynamic and the Static Method

To use the dynamic method at the STJ, first it must be validated. This is achieved by validating the dynamic and the static method with one another. Table 4.1 depicts necessary variables to determine the ARR with their uncertainties for the exemplary measurement. The uncertainty of dynamic  $ARR_{\text{fit}}$  is by far the largest contribution to the uncertainty of the dynamic  $ARR_{\text{meas}}$ . In order to validate the static and dynamic measurement method, the ARR of four different measurement scenarios was determined using both the dynamic and the static method. The same measurement conditions were applied as in sec. 4.1.1. The validation of the two methods was carried out at the model since only here it is possible to create various scenarios with constant ARR values. This was realized by closing the receiver with a lid and removing a certain number of the 13 return tubes. In the static measurements helium was injected for a total of 8 minutes. After two minutes the extraction was switched between the measuring points every minute. In total 5 minutes of the measurement data is evaluated as indicated in Fig. 4.2 according to Eq. 2.5. For each dynamic measurement helium injections of a length of one minute are followed by a pause of two minutes. This is repeated 5 times summing up to 5 minutes of active measurement. In Fig. 4.5 the mole fraction response of three of these injections are displayed. The same duration of active measurement is used in both measurement methods, making them comparable.

The results are shown in Fig. 4.6. The general trend that can be observed, is that the

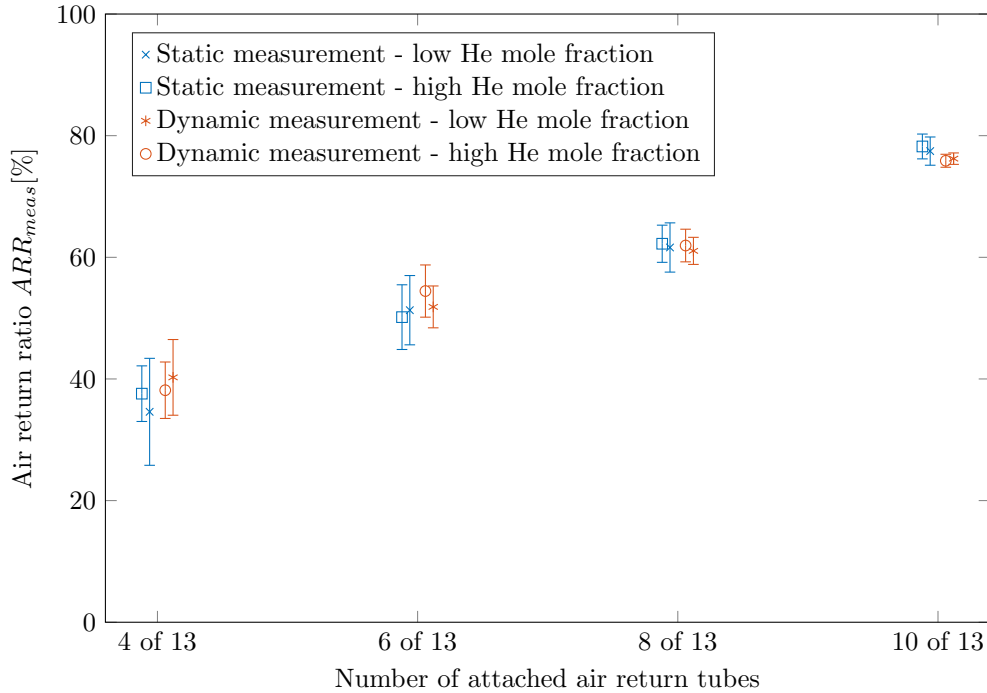


Figure 4.6: The ARR was measured using the static as well as the dynamic tracer gas measurement with a closed receiver configuration (see Fig. 3.2) for four different scenarios with a certain number of return tubes attached. The measurement was conducted with helium injection quantities of 25 std l/min and 50 std l/min. The uncertainties are presented with a 95 % level of confidence. Based on Tiddens et al. (2016b).

ARR increases with more attached air return tubes. This is to be expected, since a smaller fraction of the return air is blow away. Furthermore both static and dynamic measurements of the ARR are taken under the same experimental conditions and should therefore yield the same result. This is the case, since the results lie well within the uncertainty bounds. The two measurement methods can hence be considered validated. A further noteworthy observation is, that the uncertainty of the ARR decreases with increasing ARR. This results from a better signal to noise ratio due to a greater helium mole fraction and a smaller influence of the dynamic correction. Due to this successful validation of the two methods at laboratory scale, dynamic ARR measurements can now be applied at the STJ, which is covered in the following section.

### 4.2.3 Dynamic Measurements at the Solar Tower Juelich

Having shown that the dynamic method yields good results for the receiver model, it was applied to the STJ. First the measurement of the homogeneity of the helium mole fraction at measuring point 1 along the cross section of the piping was performed.

#### Mixing

In order to examine this at the measuring point 1, the air was blown out through a vent in the STJ which is located between the measuring point 1 and the receiver, thus effectively reducing the ARR to zero. This allows to investigate only the homogeneity of the injected helium without any temporal fluctuations. Only small deviations of the mean of 1.4% were found (see Fig. 4.7). Therefore a centrally extracted mole fraction represents the mean of the cross section, allowing point sampling.

#### Circulation Period

To measure the circulation period, helium was injected into the system. The injection time of 10s was found to give the strongest signal to noise ratio. Since the circulation period is crucial for the ARR determination (Eqs. 2.8 and 2.7), it was measured for every ARR measurement individually.

Figures 4.8 and 4.9 show circulation period measurements for an air mass flow of 5 kg/s and 10 kg/s respectively. The shown exemplary measurements are conducted without irradiation of the receiver and result in a circulation period of  $T_{\text{circ}} = (52.5 \pm 2.5)\text{s}$  and  $T_{\text{circ}} = (25.4 \pm 1.4)\text{s}$  respectively. For evaluation reasons, all circulation period measurements are conducted for 120 s. This duration was chosen to enable measuring two peaks at the lowest examined air mass flow. For this reason a third peak can be seen in Fig. 4.9, which is however not used during the calculations, due to its low signal to noise ratio.

The time of 120 s per measurement is short compared to the typical measurement time of the dynamic method. Therefore the circulation measurement is repeated more often (5 times) than the dynamic measurements (3 times).

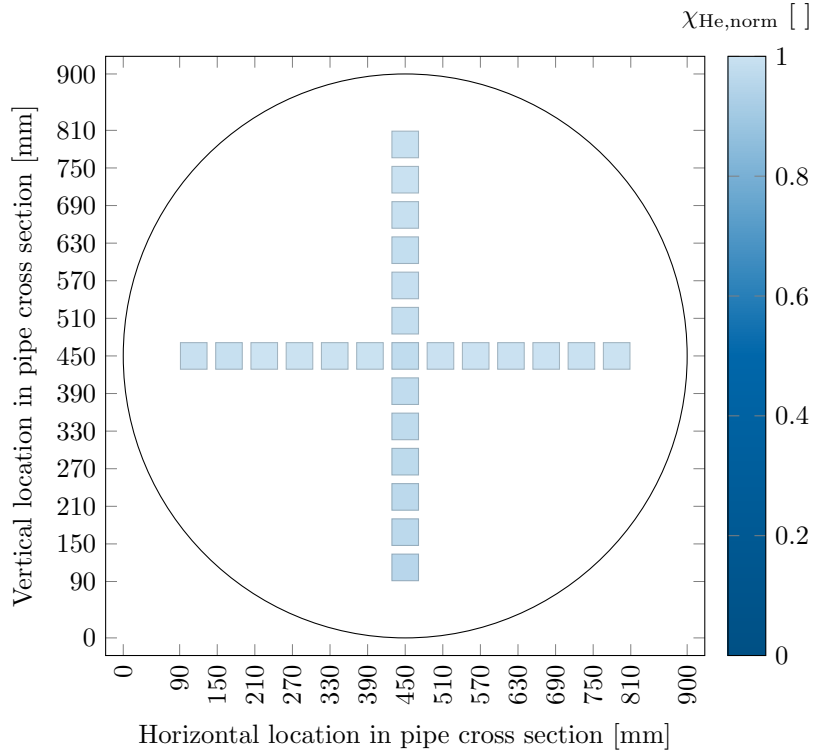


Figure 4.7: The normalized helium mole fraction is sampled along the cross section of the piping at measuring point 1 of the STJ. These measurements were performed with all return air being blown out through the vent, resulting in  $ARR = 0$ . The measurements show only minor fluctuations, with a standard deviation of 1.4%. Based on Tiddens et al. (2017b).

### Measurements without Irradiation

Figure 4.10 shows exemplarily a helium mole fraction curve of the dynamic ARR measurement without irradiation and the corresponding fit according to Eqs. 2.7 and 2.8. The leading and trailing edge of the helium mole fraction data were fitted independently ( $\chi_{\text{fit}}$ ), showing only small deviations from the data ( $\chi_{\text{He,meas,norm}}$ ).

The corrected values of the  $ARR_{\text{meas,dyn}}$  were found to be  $(51.3 \pm 0.8) \%$  and  $(67.7 \pm 0.5) \%$  for air mass flows of  $(4.98 \pm 0.03) \text{ kg/s}$  and  $(9.96 \pm 0.04) \text{ kg/s}$  respectively. The measurements were conducted at an average return air temperature of  $(18.0 \pm 1.2) ^\circ\text{C}$  and  $(18.9 \pm 0.6) ^\circ\text{C}$  and an average wind speed of  $(4.8 \pm 2.0) \text{ m/s}$  and  $(3.2 \pm 1.5) \text{ m/s}$ . The results and the corresponding circulation periods and corrections are shown in Table 4.2.

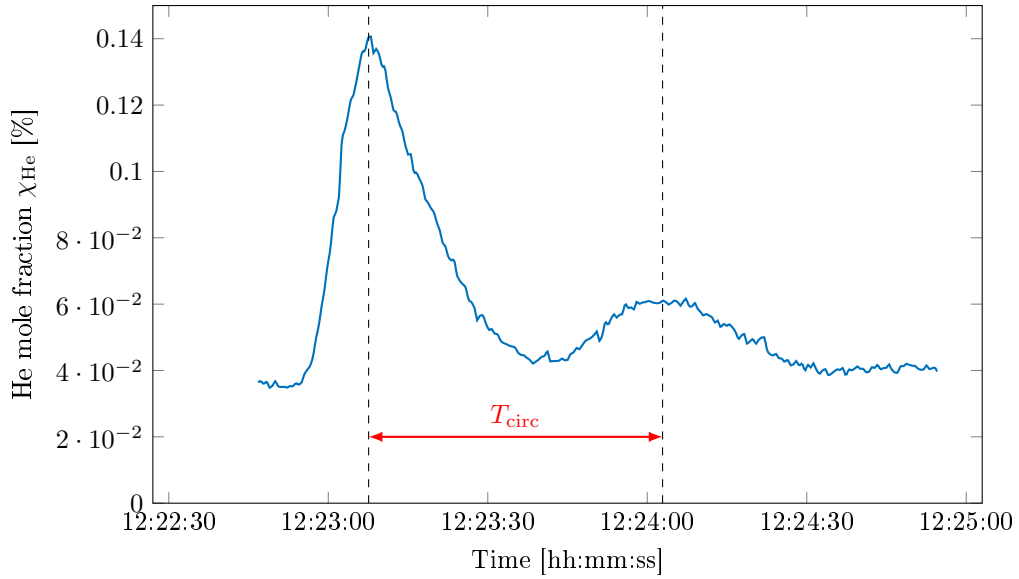


Figure 4.8: A circulation period measurement at an air mass flow of  $\dot{m} = 5 \text{ kg/s}$ . A circulation period of  $T_{\text{circ}} = (52.5 \pm 2.5) \text{ s}$  was found by measuring the duration in between the peaks. Based on Tiddens et al. (2017b).

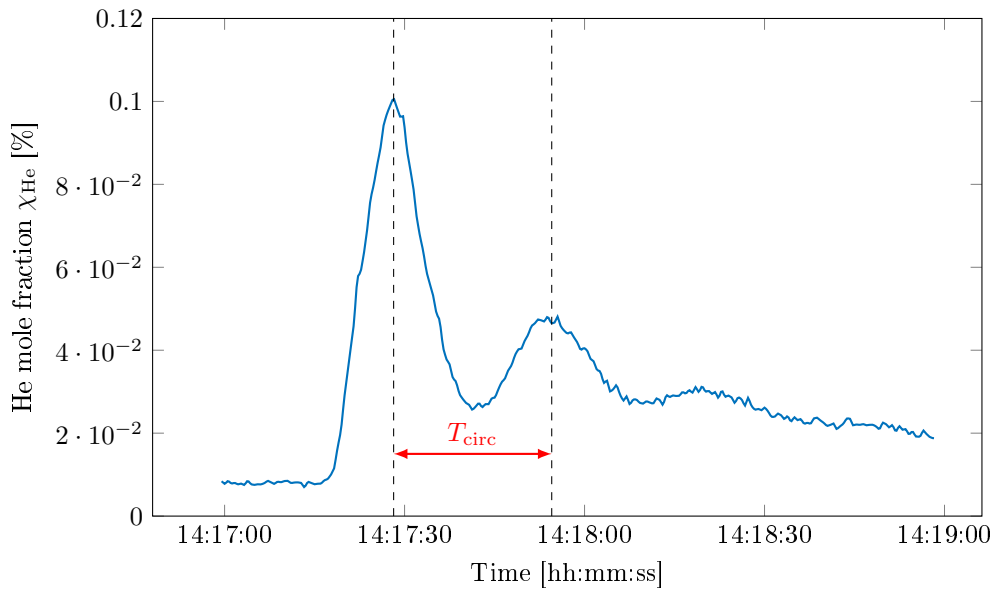


Figure 4.9: A circulation period measurement at an air mass flow of  $\dot{m} = 10 \text{ kg/s}$ . A circulation period of  $T_{\text{circ}} = (25.4 \pm 1.4) \text{ s}$  was found by measuring the duration in between the peaks. Based on Tiddens et al. (2017b).

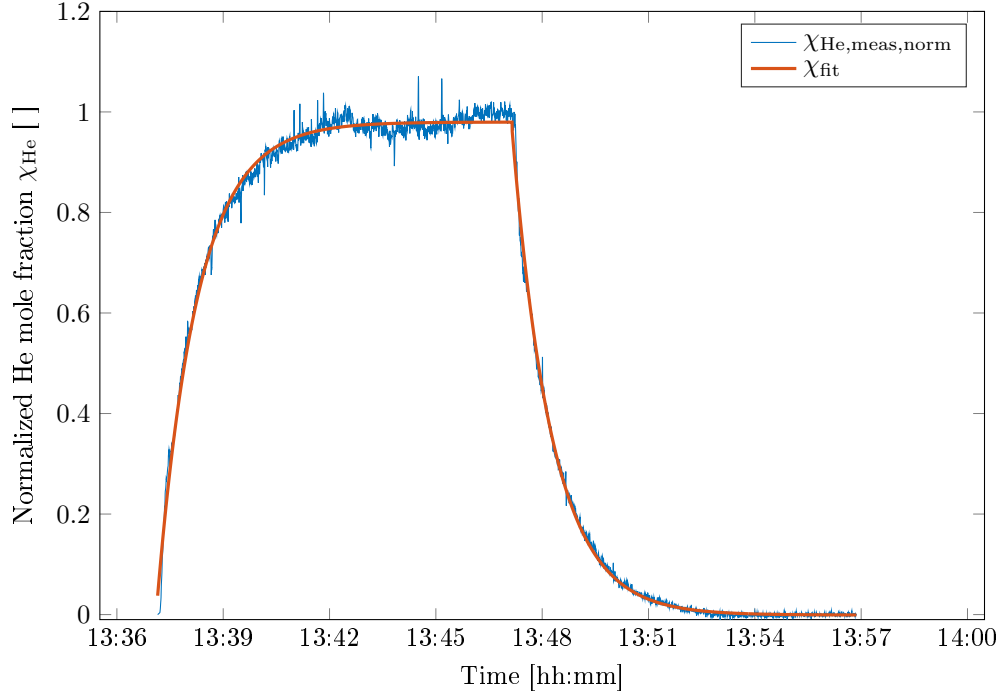


Figure 4.10: Helium mole fraction over time is shown for a measurement using the dynamic method. The measurement was conducted without irradiation with an air mass flow of  $(9.96 \pm 0.04)$  kg/s. Based on Tiddens et al. (2017b).

Table 4.2: The results of the ARR measurements at the STJ without irradiation for two different air mass flows are shown.

Measured variable	Low air mass flow	High air mass flow
Air mass flow ( $\dot{m}$ )	$(4.98 \pm 0.03)$ kg/s	$(9.96 \pm 0.04)$ kg/s
Wind Speed ( $v_{\phi,wind}$ )	$(4.8 \pm 2.0)$ m/s	$(3.2 \pm 1.5)$ m/s
Circulation period ( $T_{circ}$ )	$(52.2 \pm 0.5)$ s	$(25.5 \pm 0.6)$ s
Measured ARR ( $ARR_{fit}$ )	$(52.5 \pm 0.8)$ %	$(68.6 \pm 0.5)$ %
Dynamic correction ( $cor_{dyn}$ )	$(0.979 \pm 0.003)$	$(0.987 \pm 0.003)$
Corrected ARR ( $ARR_{dyn}$ )	$(51.3 \pm 0.8)$ %	$(67.7 \pm 0.5)$ %

Table 4.3: The results of the ARR measurements at the STJ with irradiation, for two different air mass flows are shown. The wind speed was not recorded for these measurements.

Measured variable	Low air mass flow	High air mass flow
Air mass flow ( $\dot{m}$ )	$(4.96 \pm 0.07)$ kg/s	$(9.94 \pm 0.04)$ kg/s
Circulation period ( $T_{\text{circ}}$ )	$(39.0 \pm 0.8)$ s	$(23.5 \pm 0.5)$ s
Measured ARR ( $ARR_{\text{fit}}$ )	$(57.4 \pm 1.0)$ %	$(69.4 \pm 0.7)$ %
Dynamic correction ( $cor_{\text{dyn}}$ )	$(0.981 \pm 0.003)$	$(0.988 \pm 0.003)$
Corrected ARR ( $ARR_{\text{meas,dyn}}$ )	$(56.3 \pm 1.0)$ %	$(68.6 \pm 0.7)$ %

### Measurements with Irradiation

The dynamic ARR measurements are conducted during irradiation of the main receiver. The ARR is found to be  $(56.3 \pm 1.0)$  % and  $(68.6 \pm 0.7)$  % for an air mass flow of  $(4.96 \pm 0.07)$  kg/s and  $(9.94 \pm 0.04)$  kg/s, respectively. The measurements were conducted at an average return air temperature of  $(159.6 \pm 18.2)$  °C and  $(103.6 \pm 2.6)$  °C. An average wind speed of  $(7.5 \pm 2.7)$  m/s was recorded for the first measurement, for the second measurement unfortunately no wind data was available. The corresponding results are shown in Table 4.3.

### Partial/External Air Return Measurements

To evaluate how changes of the air return system improve the overall efficiency of the power plant, the ARR must be measurable. Within this thesis two scenarios of alternative air return strategies were examined. In the first scenario a fraction  $(1 - \Psi)$  of the return air was blown out through the vent of the system to reduce the power consumption of the fan (see Section 1.2.2). In the second scenario this air was returned to the receiver using the external return system. The motivation for this is a suspected increase in the ARR as well as reduced parasitic losses due to the lower power consumption of the fan. The corrected  $ARR_{\text{meas,dyn}}$  is found to be  $(64.3 \pm 0.7)$  % and  $(67.7 \pm 0.5)$  % for an partial and external return air system, respectively. The corresponding results are shown in Tables 4.4 and 4.5.

Table 4.4: The results of the ARR measurements at the STJ without irradiation, with conventional and partial return air system are shown.

Measured variable	Air return system	
	Conventional	Partial $\Psi = 0.9$
Air mass flow ( $\dot{m}$ )	$(9.96 \pm 0.07)$ kg/s	$(9.96 \pm 0.07)$ kg/s
Circulation period ( $T_{\text{circ}}$ )	$(24.6 \pm 0.5)$ s	$(24.6 \pm 0.5)$ s
Measured ARR ( $ARR_{\text{fit}}$ )	$(65.7 \pm 0.6)$ %	$(65.3 \pm 0.7)$ %
Dynamic correction ( $cor_{\text{dyn}}$ )	$(0.986 \pm 0.003)$	$(0.985 \pm 0.003)$
Corrected ARR ( $ARR_{\text{meas,dyn}}$ )	$(64.8 \pm 0.6)$ %	$(64.3 \pm 0.7)$ %

Table 4.5: The results of the ARR measurements at the STJ of the conventional and external return air system are shown. The data for the conventional air return system is the same as in Table 4.3. The measurements were performed during irradiation of the receiver.

Measured variable	Air return system	
	Conventional	External $\Psi = 0.52$
Air mass flow ( $\dot{m}$ )	$(9.94 \pm 0.04)$ kg/s	$(9.94 \pm 0.06)$ kg/s
Circulation period ( $T_{\text{circ}}$ )	$(23.5 \pm 0.5)$ s	$(23.7 \pm 0.5)$ s
Measured ARR ( $ARR_{\text{fit}}$ )	$(69.4 \pm 0.7)$ %	$(68.6 \pm 0.5)$ %
Dynamic correction ( $cor_{\text{dyn}}$ )	$(0.988 \pm 0.003)$	$(0.987 \pm 0.003)$
Corrected ARR ( $ARR_{\text{meas,dyn}}$ )	$(68.6 \pm 0.7)$ %	$(67.7 \pm 0.5)$ %

### Fluctuating Air Return Ratio

The mole fraction curves of the displayed results deviate only very little from the applied fits. However, other mole fraction curves showed large deviations between the shape of the analytically derived curve. Fig. 4.11 shows the helium mole fraction of such a measurement over time with large deviations from the fit. Due to the low temporal resolution of the analytical method, these fluctuations are not resolved. This was the motivation for the development of the numeric method with its greater temporal resolution. The method is applied to the STJ which is described in the following section.



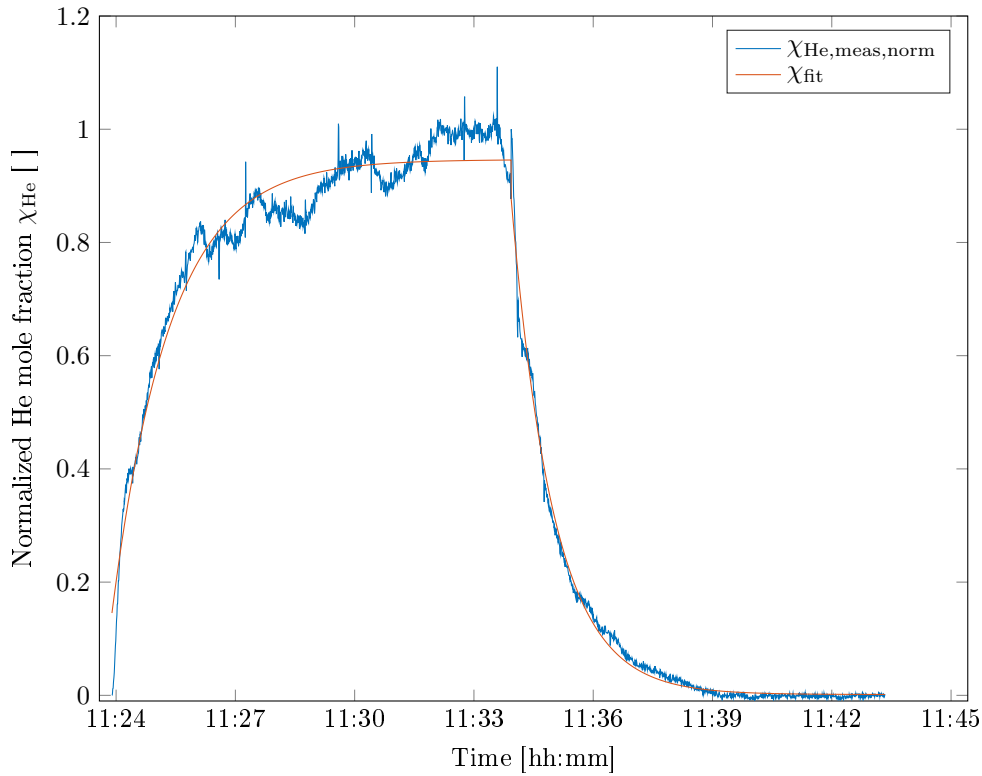


Figure 4.11: The helium mole fraction over time is shown for a measurement using the dynamic method. The measurement was conducted with an air mass flow of  $(4.96 \pm 0.07)$  kg/s at an irradiated receiver. Large deviations from the fit within the time of measurement can be observed. Based on Tiddens et al. (2017b).

### 4.3 Numeric ARR Measurements

To determine the ARR with the numeric method, two measurements need to be conducted to be able to solve Eq. 2.29. First the helium mole fraction without using the air return system  $\chi_{\text{He, meas, ARR}=0}(t)$  has to be determined. This is realized at the STJ by blowing out all return air through a vent instead of returning it to the receiver. The gathered mole fraction data also contains an error due to diffusion, this error is removed by applying a correction according to Section 2.1.3. The resulting helium mole fraction  $\chi_{\text{meas, ARR}=0}(t)$  is shown in Fig. 4.12. The fact that the shape of the curve is flat in the central region, is a further proof that the background subtraction is correct. The remaining deviation from a rectangular form arises from a non ideal helium injection. This discrepancy is further increased by the dispersion that occurs from the point of

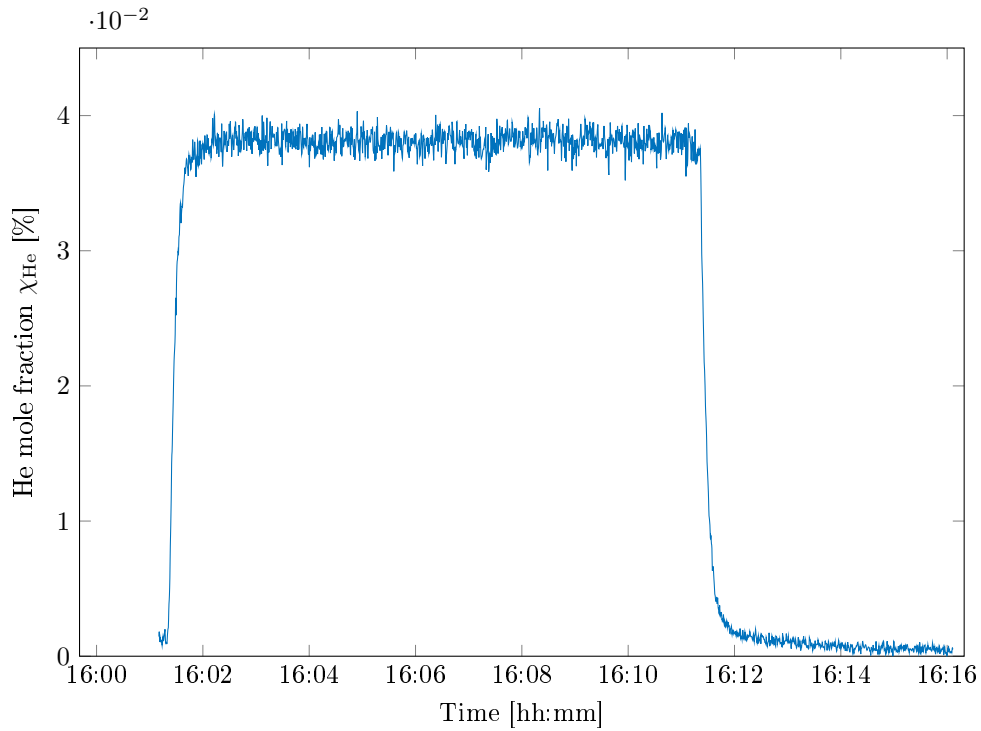


Figure 4.12: The helium mole fraction over time is shown for a measurement with an  $ARR = 0$ , achieved by blowing all return air through a vent instead of the receiver. The shown mole fraction data has been corrected for the diffusion of the helium  $\chi_{\text{He,diff}}$  according to Section 2.1.3.

injection to the measuring point 1.

#### 4.3.1 Validation of the Numeric with the Dynamic Method

The numeric method has been applied to all ARR measurements conducted at the STJ. The ARR is hereby determined for every point of helium mole fraction measurement. Therefore the average of the numerical ARR is calculated to compare the numeric results to the dynamic ones. It was then compared to the mean of the dynamic method. The difference between the results of the two measurement methods was calculated for a total of 33 measurements. The average deviation between the results is 1.1%. The numeric method is hence successfully validated at the STJ with the dynamic method. It can therefore be applied for high resolution ARR measurements.

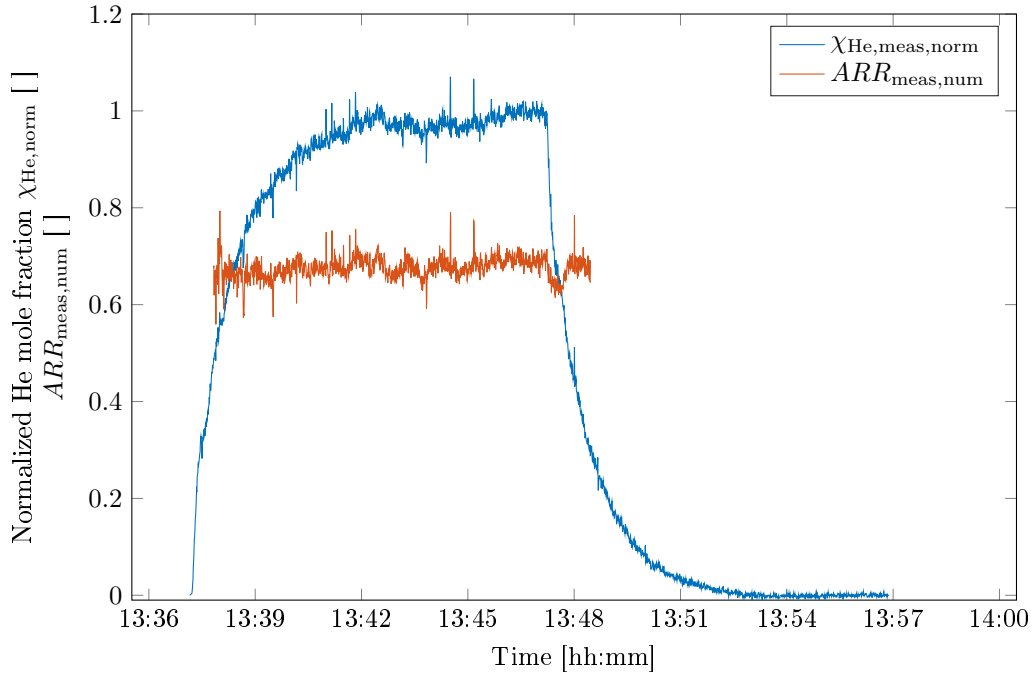


Figure 4.13: Helium mole fraction and ARR over time are shown for a measurement using the numeric method. The average  $ARR_{\text{meas,num}}$  is found to be  $ARR_{\text{meas,dyn}} = (67.6 \pm 0.4) \%$  compared with the result of the dynamic method  $(67.7 \pm 0.5) \%$ . The measurement was conducted without irradiation with an air mass flow of  $(9.96 \pm 0.036) \text{ kg/s}$  (same data as used in Fig. 4.10).

### 4.3.2 Measurements at the Solar Tower Juelich

The numeric method allows an ARR measurement with the same temporal resolution as the mole fraction measurements. Because this resolution is about 0.5 seconds per measurement, it is possible to reevaluate the recorded mole fraction data. Fig. 4.13 shows the exemplary results of the numeric method for the same data as in Fig. 4.10. The ARR shows only small deviations over the time of measurement. In the measurement displayed in Fig. 4.14 this is however not the case. It may be suspected, that these changes in ARR result from changes in environmental conditions such as wind or temperature of the main receiver. A variation due to a fluctuating air mass flow was excluded since the mass flow  $(4.96 \pm 0.07) \text{ kg/s}$  showed very little variation.

To investigate the correlations between the ARR and wind, the three recorded wind parameters (azimuth wind speed, elevation wind speed, wind direction) are compared to

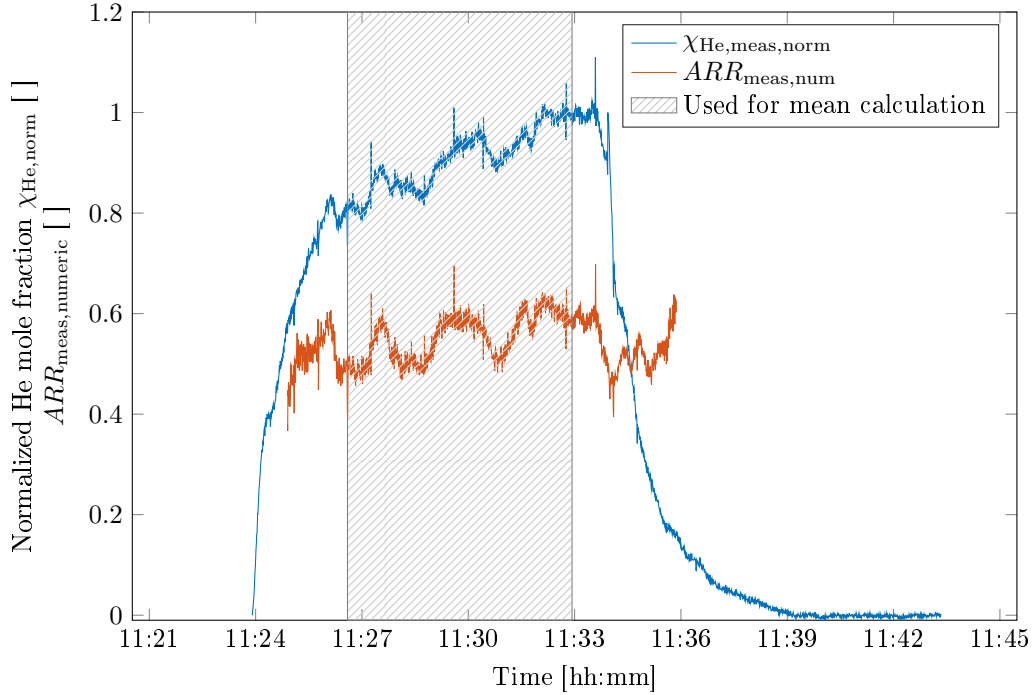


Figure 4.14: Helium mole fraction and ARR over time is shown for a measurement using the numeric measurement. When regarding only the indicated central part, the average  $ARR_{\text{meas,num}}$  is found to be  $(54.32 \pm 9.1) \%$  compared with the result of the analytical method  $ARR_{\text{meas,dyn}} = (56.3 \pm 1.0) \%$ . The measurement was conducted without irradiation with an air mass flow of  $(4.96 \pm 0.07) \text{ kg/s}$  (same data as: Fig. 4.11).

the  $ARR_{\text{meas,num}}$ .

Fig. 4.15 shows an exemplary measurement whereby the three wind parameters were plotted next to the ARR. No correlation between the ARR and the existing wind data could be observed. Therefore the correlation coefficients for the three wind parameters and the ARR were calculated for different time shifts. No significant correlations have been found either. The correlation between the wind and the ARR should be examined in greater detail with a larger data set.

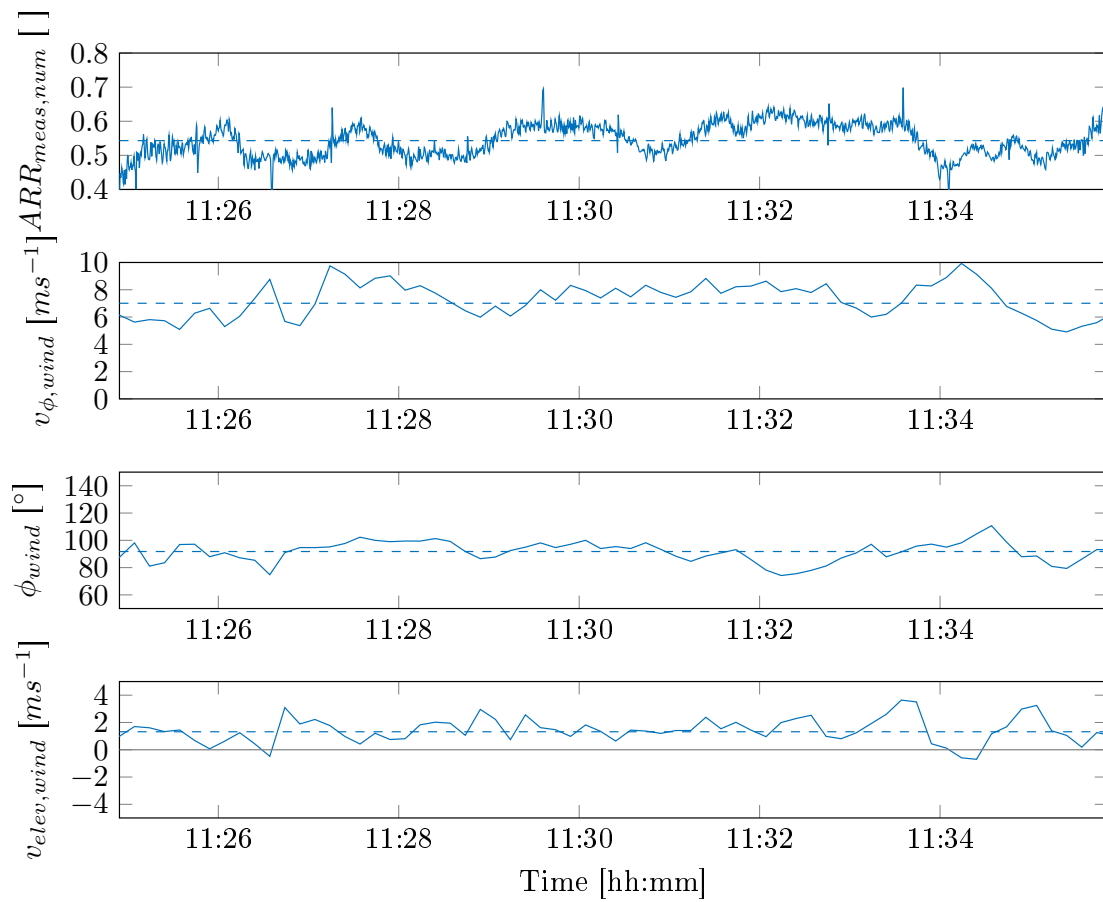


Figure 4.15:  $ARR_{meas,num}$ , azimuth wind speed  $v_{\phi,wind}$ , wind direction  $\phi_{wind}$  and elevation wind speed  $v_{wind,elev}$  are shown (same data as: Fig. 4.14). A negative  $v_{wind,elev}$  indicated a downwards wind,  $\phi_{wind} = 0$  indicates a wind from the north. No apparent correlation between  $ARR_{meas,num}$  and the other parameters can be observed.

## 4.4 Return Air Visualization

In this section the application of the Induced Infrared Thermography (IIT) at the research platform as well as the main receiver of the STJ are covered. The developed Infrared Image Velocimetry (IRIV) was used to further investigate the found flow field.

### 4.4.1 Visualizations at the Testreceiver

In order to visualize the return air flow using IIT, carbon dioxide is injected into the return air. The reached carbon dioxide mole fraction has not been measured at the

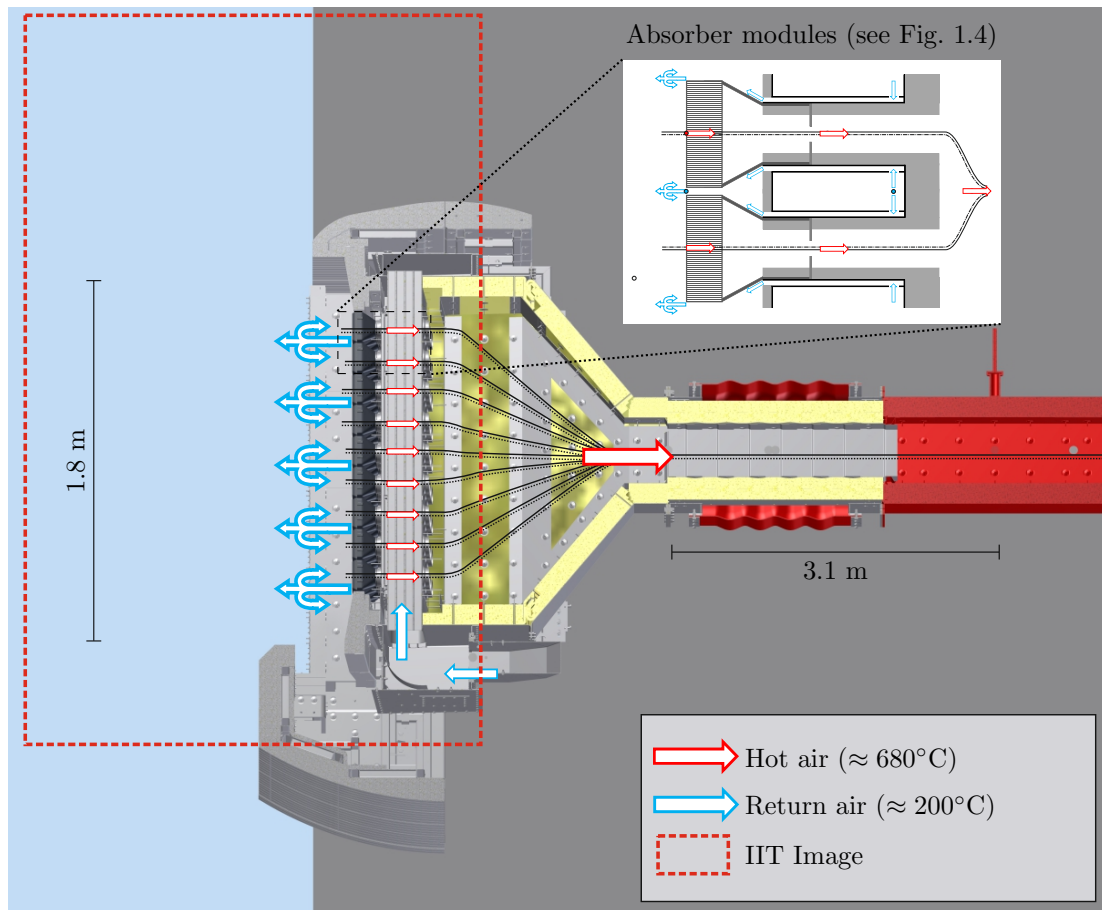


Figure 4.16: A sectional CAD view of the Testreceiver is shown. The air flow as well as the position of the viewing area of the IIT images is indicated. Based on Tiddens et al. (2017a).

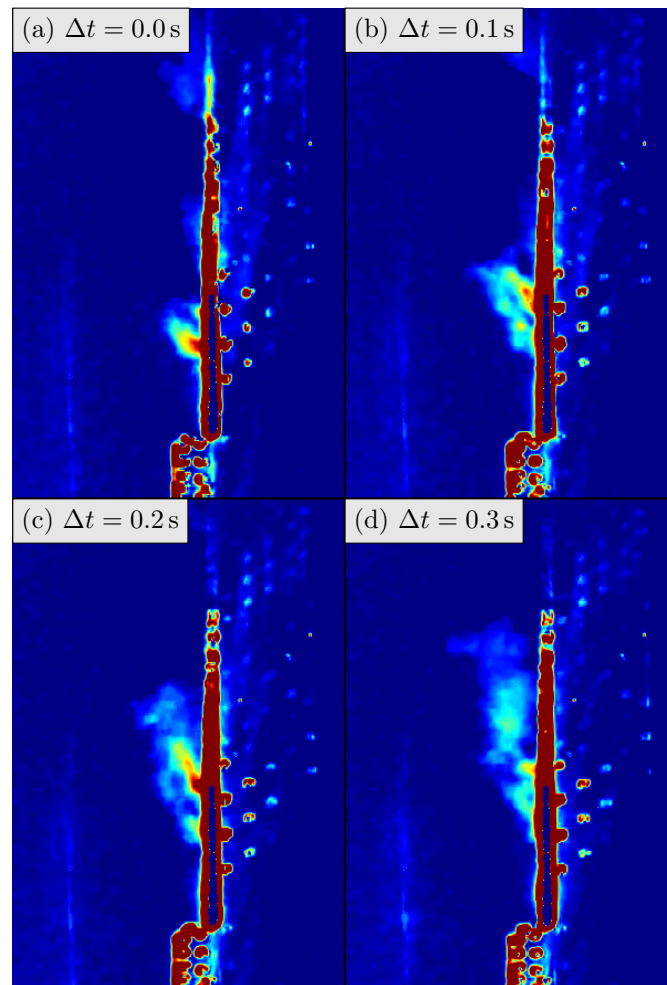


Figure 4.17: A typical sequence of four successive images has been taken at the research platform. It can be seen that the air flow moves upwards from image (a) to (d). Based on Risthaus (2015)

research platform. It can however be assumed, that the concentration was at least 1%, due to the small mass air flow of  $(0.755 \pm 0.027)$  kg/s. A sectional CAD view of the Testreceiver is shown in Fig. 4.16. The air flow as well as the position of the viewing area of the IIT images is indicated.

A typical sequence of images which were taken of the Testreceiver from a side view is shown in Fig. 4.17. From image (a) to (d) it can be seen, that a large part of the blown out air moves upwards, and does not seem to be sucked in again. This typical direction of flow was however also disturbed in some events. In Fig. 4.18 two non subsequent images are shown where the direction of flow differs from the direction in Fig. 4.17. Although

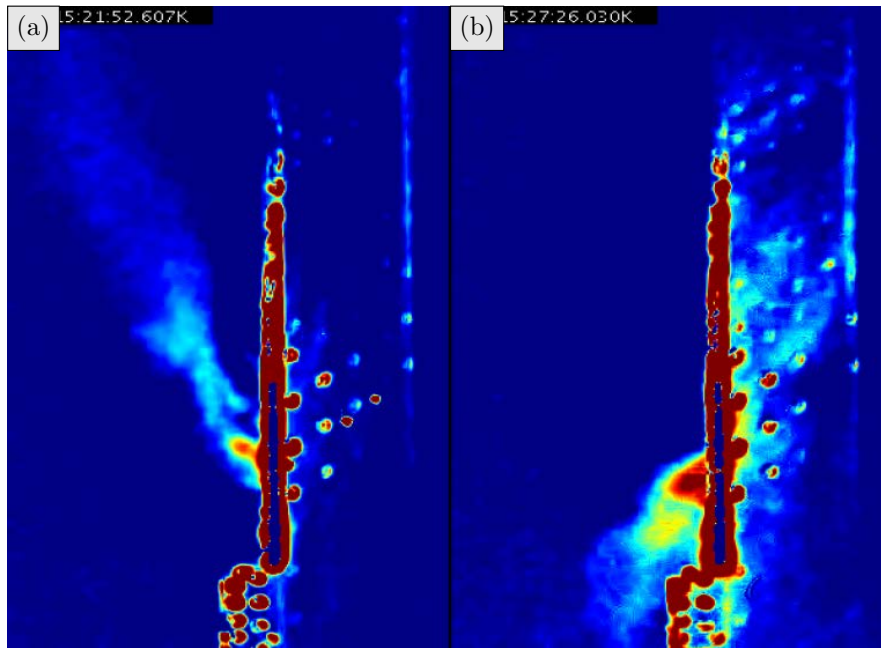


Figure 4.18: Two IIT images showing an atypical flow are displayed. The return air is taken further away from the receiver in (a) and the direction of the flow is reversed in (b). (Risthaus, 2015)

the motion of the flow in image (a) is directed upwards again, the flow moves further away from the receiver. In image (b) the direction of flow is completely reversed, and the blown out air moves downwards.

In order to examine the typical flow field, it is important to have representative measuring results for the direction of flow and velocity for a longer period. To achieve this, a sequence of 100 images within 4.5 seconds was processed using the newly developed IRIV technique which is described in Section 2.3.3. The results are shown in Fig. 4.19. The measurements were conducted with irradiation and an air return temperature of  $(122 \pm 1)^\circ\text{C}$ . It can be seen that the flow is buoyancy driven and moves generally upwards and away from the receiver. The results are not considered as quantitative velocimetry results so far. It should at the moment rather be seen as an indication of direction of the flow over a certain period of time.



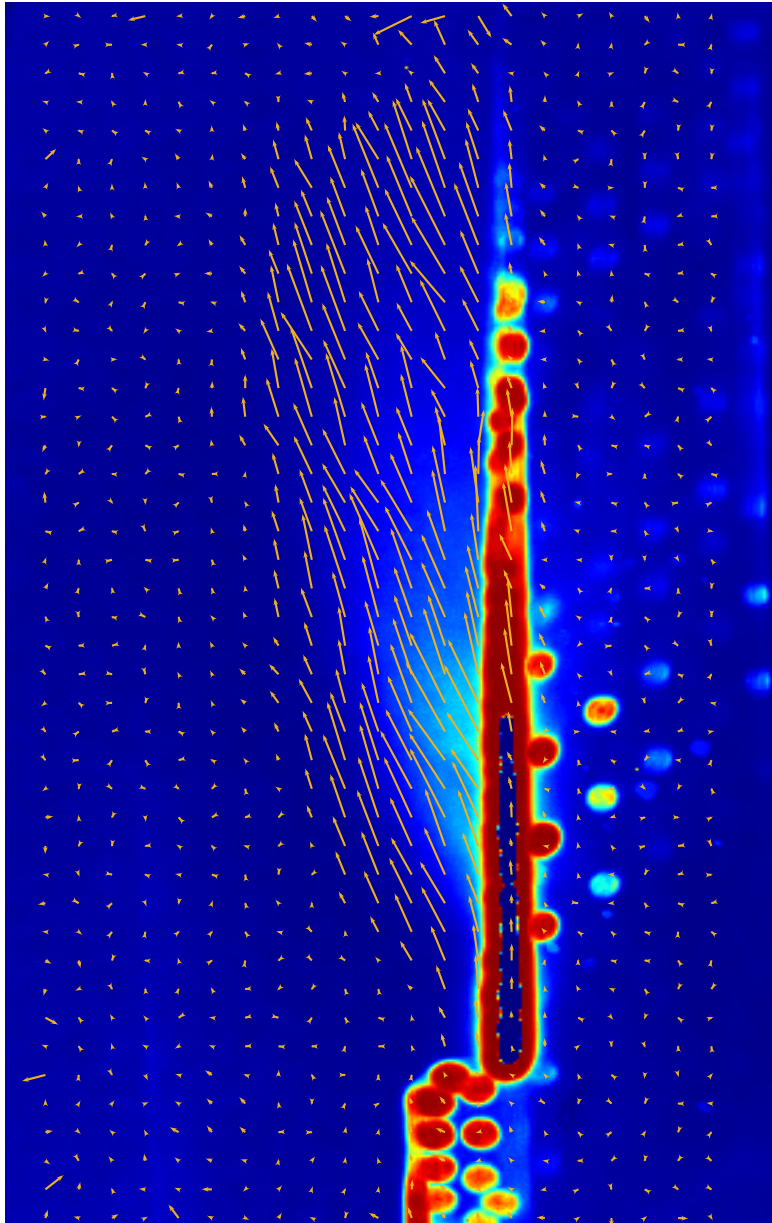


Figure 4.19: The vector field indicating the flow is superimposed on the average of the sequence's images. The examined sequence consists of 100 IIT images with a total duration of 4.5 seconds. Since this is the first application of IRIV and the first flow measurement at the Testreceiver, it should to be treated as a qualitative measurement only. Based on Tiddens et al. (2017a).

#### 4.4.2 Visualizations at the Main Receiver

The measured signal is significantly weaker at the STJ than at the research platform. This is caused by lower air return temperatures, lower achievable carbon dioxide concentrations in the air flow of  $(1272 \pm 151)$  ppm and a larger distance between the air flow and the camera. A photo of the STJ from the perspective of the infrared camera is shown in Fig. 4.20. The section of the image seen by the infrared camera is indicated.

In Fig. 4.21 a typical sequence is shown for the main receiver of the STJ. The sequence consists of four images with a total duration of 0.72 s taken at a return air temperature of

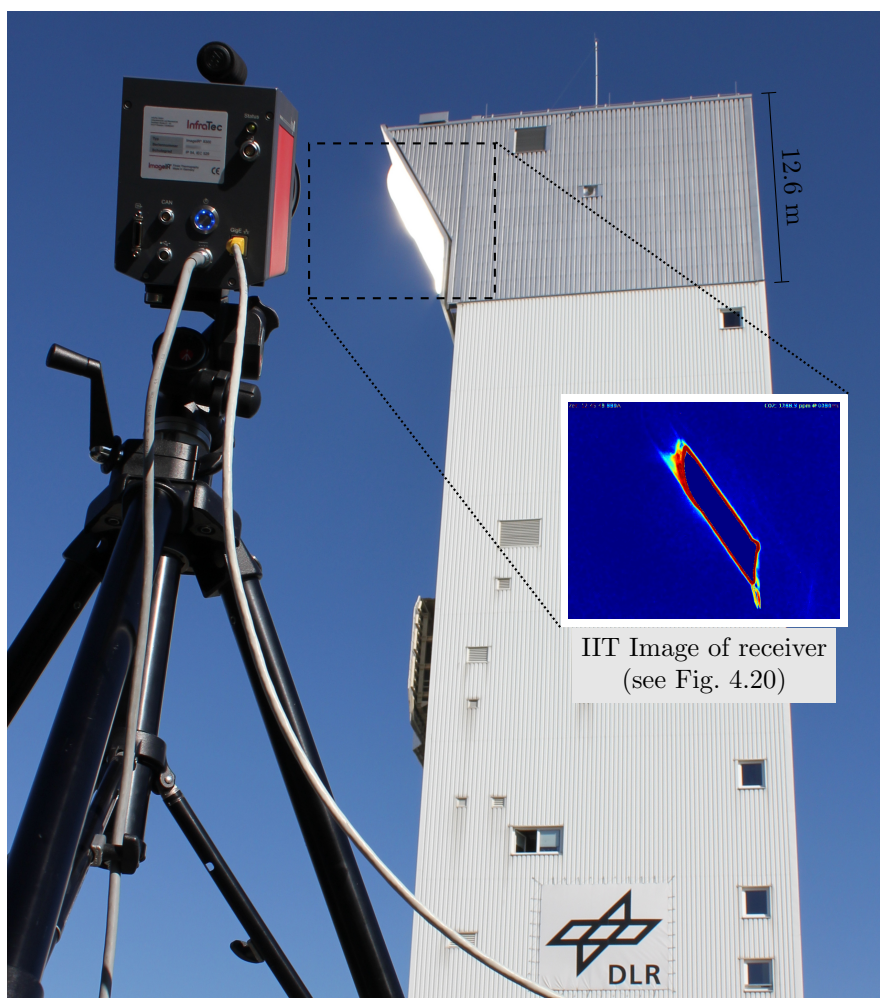


Figure 4.20: A photo of the STJ from the perspective of the infrared camera. The section of the image seen by the infrared camera is indicated.

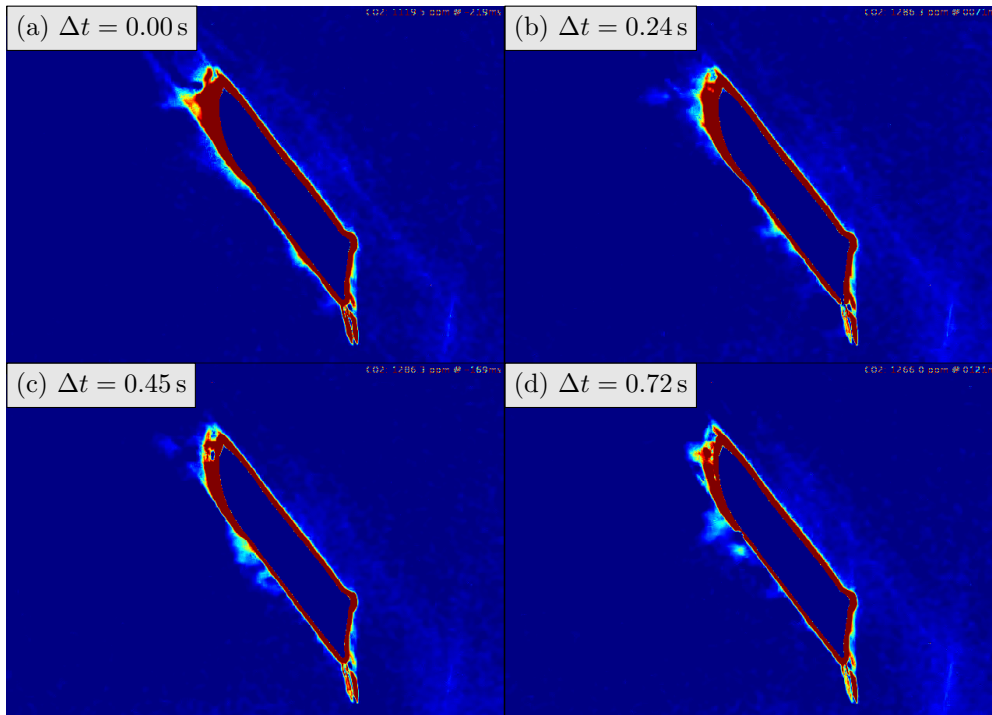


Figure 4.21: A typical sequence of four successive images taken at the main receiver is shown. It can be seen that the air flow moves upwards from image (a) to image (d). Based on Risthaus (2015).

( $184 \pm 1$ ) °C. The azimuth wind speed was recorded with ( $7.3 \pm 1.6$ ) m/s. The typical air flow of the STJ in images (a) to (d) moves upwards. This is similar to the return air flow measured at the Testreceiver. However, at the STJ the receiver is inclined downward. Therefore the hot air closer to the receiver while moving upwards. An inverse direction of airflow could also be observed. This downward flow is not shown due to its very weak signal to noise ratio. The flow inversion can be seen in a video, however not in a still image. To be able to display the direction of the air flow in front of the receiver, the IRIV method was applied to a sequence of 100 images within 1.9 s. The results are shown in Fig. 4.22. These velocimetry results should not be considered quantitative but as qualitative information about the return air flow. The direction of flow shows a clear upwards movement close to the receiver's surface.

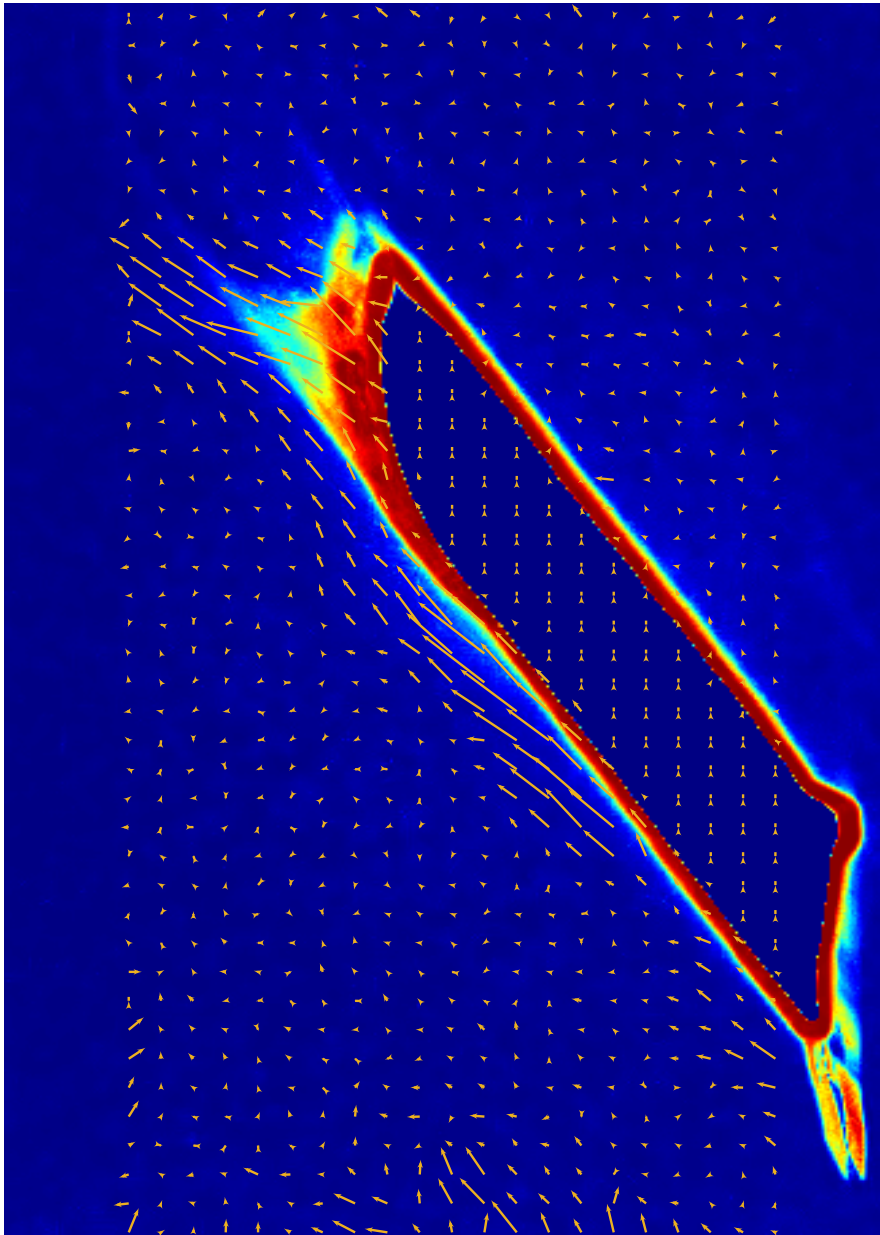


Figure 4.22: The vector field indicating the flow is superimposed on the average image of the sequence of the main receiver of the STJ. The examined sequence consists of 100 IIT images of a total duration of 1.9s seconds. Since this is the first application of IRIV and the first flow measurement at the main receiver, it should be treated as a qualitative measurement only. The conventional air return mechanism was used and an  $ARR_{\text{meas,dyn}} = (58.0 \pm 1.2)\%$  has been measured. Based on Tiddens et al. (2017a).

## 5 Discussion

*“Forty-two!” yelled Loonquawl. “Is that all you’ve got to show for seven and a half million years’ work?”*

— Douglas Adams, *The Hitchhiker’s Guide to the Galaxy*

The results of the ARR measurements and the return air visualization that were given in Chapter 4, will be discussed within this chapter.

### 5.1 ARR Measurement Methods

The thermal ARR is not measurable, since all required temperature and flow measurements would have to be conducted at the surface of the receiver with a high spatial resolution. Since the return air flow in front of the receiver is turbulent, the diffusion of helium and thermal conduction effects become negligible. Therefore the substantial ARR can be assumed to be equal to the thermal ARR, which has been measured within this thesis.

The original goal was to achieve an ARR measurement with a maximum uncertainty of at least  $\pm 5\%$ . This goal was reached since the ARR was measured with a minimal uncertainty of  $\pm 0.3\%$ . The fact that the measurement precision is better than expected is caused by the larger than anticipated circulation periods at the STJ. These arise mainly from the use of the thermal storage during all the measurements at the STJ, which incorporates a large air volume.

The occurring long circulation periods however lead to a bad temporal resolution of the dynamic method, which prevents the analysis of the ARR fluctuations during measurement. The dynamic method at the STJ has a temporal resolution of about one

measurement every 300 seconds. The numeric method was developed in order to achieve a higher temporal resolution of about one measurement every 0.5 seconds. This is the measurement frequency of the used mass spectrometer.

The numeric method was successfully validated with the dynamic method for various different measurement scenarios. This included the usage of the partial and external air return systems, whereby a part of the return air is not blown out in between the absorber modules of the receiver. An external validation of the tracer gas methods could not be conducted, since a trustworthy ARR measurement based on an entirely different measurement method currently does not exist.

In total three different methods of measurement are presented, which promise a successful future application in any given solar thermal power plant based on the open volumetric receiver concept. A summary of the three methods is given in Table 5.1. Due to the fact that a future commercial power plant is likely to have a larger length of piping, the mixing of the tracer within the air will probably not pose a restriction on the type of measurement as being the case at the STJ. The static method should be chosen if low effort in data processing has a priority. However, the application of the static method requires a homogeneous distribution of the tracer at both measuring points, leading to a more complicated experimental setup. A further disadvantage of the static method is the low measurement frequency.

The dynamic method should only be applied in two cases. Either if a validation of the numeric or the static measurement is needed or if both the static and the numeric method can not be applied. This could be the case if no vent exists and point sampling is only possible at one measuring point.

The numeric method should be applied in all other cases for several reasons. Foremost it allows the measurement of the ARR with a high temporal resolution. Additionally, only one measuring point is needed and it furthermore has the potential to be developed into an integrated measurement system. The data processing of the numeric method is furthermore less complex than the one of the dynamic measurement.

Table 5.1: Summary of the three developed tracer gas measurement techniques to determine the ARR. All three techniques require helium to be injected into the air circuit and the measurement of the helium molar fraction using a mass spectrometer (MS).

	Measurement method		
	Static	Dynamic	Numeric
Points of measurement	2	1	1
Additional required measurements	Mixing of helium at both measuring points	Circulation period, transfer function, diffusion of helium	Circulation period, ARR=0 (vent), diffusion of helium
Best temporal resolution	Limited by MS temporal resolution, typically 0.5 seconds	Depends on circulation period	Limited by MS temporal resolution, typically 0.5 seconds
Prerequisites	Point sampling possible at both measuring points	Constant mass flow during measurement required	Currently constant mass flow during measurement required
Development potential	Low	Low	High
Limitations	Complicated experiential setup, two MS required for high temporal resolution	Low temporal resolution	Vent required for ARR=0
Application at STJ	No, point sampling was not possible at measuring point 2	Yes	Yes
Best measured temporal resolution	-	300 seconds	0.5 seconds
Smallest measured uncertainty	-	$\pm 0.3\%$	$\pm 0.4\%$
Reason for future application	If low complexity of data processing required, for validation purposes	If point sampling not possible and no vent available, for validation purposes	For all other measurements

## 5.2 ARR Measurements at the Solar Tower Juelich

The ARR of open volumetric receivers was often assumed and measured to be up to 60 % (Vogel and Kalb, 2010; Ávila-Marín, 2011). The measured  $ARR_{\text{meas,dyn}}$  at the STJ of  $(68.5 \pm 0.7) \%$  is higher than this expected value. Fig. 1.4 shows that this difference corresponds to an increase of the expected overall system efficiency of 4 – 5 %, making the open volumetric receiver concept more promising. A negative effect of irradiation on the ARR could not be found. In contrast to expectations, the ARR at the main receiver was even slightly higher with an irradiated receiver than with a cold one.

At the receiver model no influence of the air mass flow on the ARR was apparent. However, at the main receiver of the STJ, the ARR is strongly dependent on the air mass flow. Téllez et al. (2004) also measured an increase in the ARR with increasing air mass flow. Although the measurements by Téllez et al. (2004) should only be seen as a rough estimate, the measurements at the STJ confirms this finding. The ARR without irradiation increased by 16 % when increasing the air mass flow from 5 kg/s to 10 kg/s. The ARR of an irradiated receiver increased by 12 % with the same increase in air mass flow. These findings are based on four measurements only and can therefore not be separated from other sources of influence as for example wind. It does however highlight the importance of understanding the air flow in front of the receiver and in the influence of wind.

## 5.3 Influence of Wind on the ARR

It is suspected that wind has an influence on the ARR. This is assumed since losses due to  $ARR < 1$  occur at the receiver front. The air flows which govern the ARR are hence exposed to wind.

The annual amount and direction of the occurring wind depends strongly on the power plant location. The knowledge of the influence of wind on the ARR is therefore important to allow correct annual efficiency predictions for a potential power plant location. This is especially important for the construction of power plants with taller tower heights, exposed to higher wind speeds.



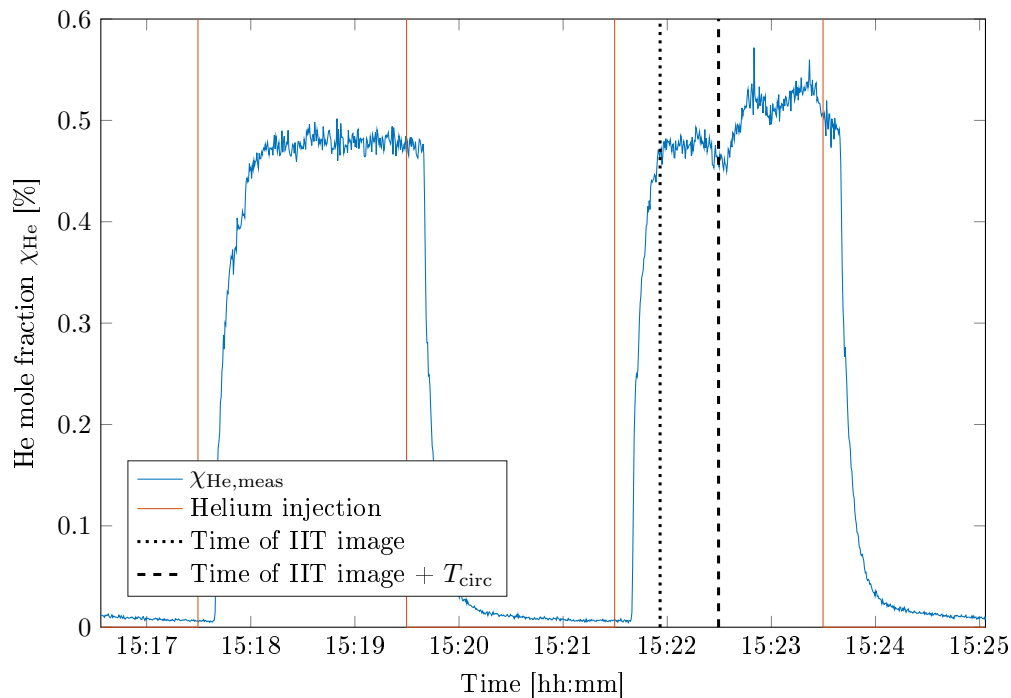


Figure 5.1: Helium mole fraction data around the time of the IIT (see Fig. 4.18 (a)). The anomaly was detected in front of the receiver at 15:21:52, corresponding to the helium mole fraction at around 15:22:30.

A correlation between wind and the ARR could so far not be observed. It is suspected that this is caused by the lack of a sufficiently large database of wind and ARR data. The wind data for a great portion of the conducted ARR measurements is missing. This was caused by a data acquisition malfunction of the weather station at the STJ. Variations within the captured weather data could so far not be associated with ARR fluctuations.

The assumption that wind plays a significant role on the ARR is however backed by a combination of ARR and IIT measurements. The detected air flow anomaly in front of the receiver (see Fig. 4.18 (a)) was conducted in parallel with a dynamic tracer gas measurement. In Fig. 5.1 the helium mole fraction data around the time of the IIT measurement is displayed. The effect of the flow anomaly can be seen in the helium mole fraction data. At the time of the IIT image the ARR at the receiver front decreases, which can be measured about one circulation period later at the measuring point at around 15:22:30. At this time the helium mole fraction is lower compared to the previously measured peak. This underpins the assumption that the ARR is influenced significantly

by wind.

## 5.4 Flow Field in Front of the Receivers

The observed return air flow is a two-dimensional projection of the infrared radiation emitted by the carbon dioxide within the return air flow. It is not simply an integration over the intensity of the emitted radiation over the volume, since the carbon dioxide also absorbs radiation. This suggests that the visualization should only be used qualitatively.

The previously described combination of the return air visualization with tracer gas measurements is helpful in examining the link between wind and the ARR. Additionally, the return air visualization is especially interesting for comparing the IRIV results (Fig. 4.19) to the results of the CFD simulations shown in Fig. 1.10. Although these CFD simulations only take four absorber modules into account, they are the best existing reference for the flow pattern in front of the receiver.

The observed flow pattern in the CFD simulation is similar to the IRIV results. The air flow close to the receiver could however not be observed at the research platform, since the receiver modules were blocked from vision by the irradiation protection. At the main receiver the signal close to the receiver could also not be identified clearly. This was caused due to a lower spatial resolution resulting from a greater distance and a generally weaker signal strength, which is discussed in more detail in Section 2.3. At a larger distance from the receiver the air flow could be detected at both receivers. In the majority of cases the blown out air moves upwards. Return air which is once visible in front of the receiver is not sucked in again into the receiver. The upwards movement is mainly dominated by buoyancy forces caused by the decreased density of the hot air.

This detected air flow pattern could be the explanation why at the STJ the ARR is larger than expected. It can be seen that in the case of the inclined main receiver the blown out air of the lower regions is transported upwards along the upper receiver modules, potentially increasing the ARR by being sucked in again. This in turn highlights the importance of the receiver geometry and the understanding of the air flow. The effect can currently not be investigated, due to the lack of resolution in flow information close to the receiver.

## 5.5 ARR Measurements of the Partial and External Air Return Mechanism

The partial and external air return system was developed to increase the overall efficiency of the power plant. For a partial air return of up to  $\Psi = 0.7$  it was predicted that the air return ratio would stay constant (see Fig. 1.9). The improvement in the overall system efficiency arises hereby due to a decrease in parasitic losses caused by the fan. The predictions are based on a single absorber module.

The measurement results support the trend of the partial air return shown in Fig. 1.9 which were found from simulations by Maldonado Quinto (2016). Improvements of the system efficiency by partial and external air return systems are also apparent from the measurements since the ARR stays fairly constant and the parasitic losses of the fan were reduced due to a decrease in pressure drop.

An increase of the ARR to about 80% was predicted by Maldonado Quinto (2016) for the external air return system. Unfortunately this increase could not be measured. An improvement to the system efficiency is however given due to reduced parasitic losses.

A further improvement of the overall system efficiency of the partial or external air return is caused by the reduction of cooling losses. These losses occur due to the heat transfer between the sucked in and blown out air within the receiver (Ahlbrink et al., 2013). The cooling losses are the fraction of this transferred heat which is lost to the environment due to a non ideal ARR. For the partial and external air return system these cooling losses are smaller. Less air is blown out in between the absorber modules with a higher ARR than the fraction of externally returned air. Therefore less energy is lost to the environment. A partial or external air return system with the same ARR as the conventional air return system would hence have a higher system efficiency. The cooling losses should be investigated further.

## 5.6 Improvements of the Open Volumetric Receiver Concept

The ARR of the open volumetric receiver concept could be improved on the receiver scale as well as the absorber module scale. A cavity shaped receiver would reduce return air losses due to natural convection. Although the influence of wind on cavity receivers is currently still under investigation, it can be expected that the ARR would be higher in a cavity shaped receiver due to the protection of the return air from wind. The remaining influence of wind could be reduced by using an air curtain at the opening of the cavity.

On an absorber scale the size of the areas through which the air is blown out (outlet area) and sucked into the receiver (inlet area) are essential. The ratio of the outlet to the inlet area should be increased as proposed by Maldonado Quinto (2016). The first benefit for system efficiency would be the potentially lower pressure drop. This effect is also exploited in the partial as well as external air return system. The second likely benefit arises from an increase in ARR. The return air is currently blown away from the receiver. The increase in the ARR is caused by the reduction of this return air velocity.

Currently two very promising ideas are being patented to realize a larger outlet to inlet area ratio. The first is increasing the size of the gaps between the absorber modules and inserting active absorber material in between the absorbers. The return air is blown out through this absorber material. (Maldonado Quinto, 2016) The second idea is to pass the return air through a certain fraction of dedicated absorbers instead of through the gap between the absorber modules (Tiddens et al., 2016a). Both of these ideas should be investigated in respect to the ARR with the developed measurement methods.

## 6 Conclusions

The main goal of this thesis was the development of measurement techniques for analysis of the open volumetric receiver concept in respect to the air return ratio (ARR). The ARR depends on many variables such as wind, geometry of the receiver design and operational mode. Its value was prior to this work unknown.

The first and main objective was the development of a measurement technique for the quantification of the ARR with maximum precision and its application at the solar tower Juelich (STJ). The ARR measurement technique was developed on a laboratory scale and applied to the STJ. For the laboratory scale a receiver model was constructed.

At the STJ surface temperatures of up to  $1000^{\circ}\text{C}$  can be measured. Due to the additionally large air mass flows of around  $10\text{ kg/s}$  it was decided to use a tracer gas method. Hereby a tracer gas is injected into the air flow. The ARR can be determined by measuring the reduction of the injected tracer occurring at the receiver front.

The harsh measurement environment at a solar receiver posed tough conditions on tracer gas candidates. Using helium as a tracer gas assured the application and made the measurement technique furthermore environmentally friendly. The amount of tracer was determined by extracting an air sample of the return air and measuring its helium mole fraction using a mass spectrometer. The extraction of the air samples was realized at two locations in the air circuit by individually constructed measuring probes. The first measuring point was located just before the air is blown out of the receiver, the second just after the air is sucked into the receiver.

In total three tracer gas measurement methods were developed at three development stages. The tracer gas helium is injected either continuously or intermittently into the system. During application of the static method, the tracer is injected continuously. The average helium mole fraction at both measuring points is recorded and the ARR is determined from these mean values. For the dynamic measurement the tracer is injected

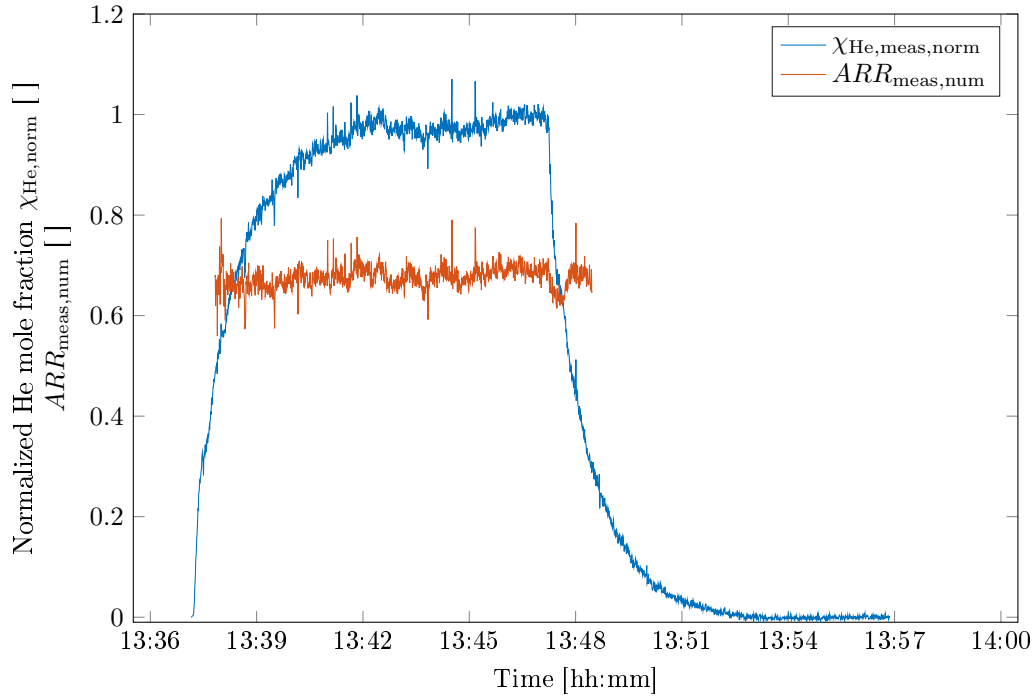


Figure 6.1: Helium mole fraction and ARR over time are shown for a measurement using the numeric method. The average ARR is found to be  $(67.6 \pm 0.4) \%$  compared with the result of the dynamic method  $(67.7 \pm 0.5) \%$ . The measurement was conducted without irradiation of the receiver. (same data as: Fig. 4.13)

intermittently. The ARR is extracted from fitting the helium mole fraction response of one measuring point. To achieve this, the circulation period must be determined. Further corrections had to be applied to the extracted ARR to correct for various errors. The third method allows measuring the ARR with a very high temporal resolution of 0.5 seconds per measurement. This method requires only helium mole fraction data from one measuring point. However an additional measurement using the vent of the STJ is required. All three methods were successfully validated with one another.

The ARR measurement was conducted at the STJ using both the dynamic as well as the numeric method. In Fig. 6.1 the numeric ARR result is given for a measurement without irradiation of the receiver. The average ARR is found to be  $(67.6 \pm 0.4) \%$  using the numeric method and  $(67.7 \pm 0.5) \%$  by applying the dynamic method without irradiation of the receiver. The high accuracy of these measurements is evident from the very small discrepancy between their results.

The ARR of the STJ was assumed to be 60%. The shown results indicate a significantly

higher ARR of nearly 70 %. The expected negative effect of irradiation on the ARR could not be found. The ARR of an irradiated receiver ( $68.6 \pm 0.7$  %) was even higher.

The newly developed measuring techniques were used to investigate the partial and external air return system. Hereby only a fraction ( $\Psi$ ) of the returned air is blown out through the gaps between the absorbers. When using a partial air return system the remaining fraction of air is blown away through a vent. A partial air return of  $\Psi = 0.9$  has no significant effect on the ARR. For an external air return, the separated fraction of the return air is brought in front of the receiver from the bottom and the sides. An external air return of  $\Psi = 0.52$  caused no significant increase in the ARR. This opposes the predicted increase to about 80 % by simulation (Maldonado Quinto, 2016).

The second objective was the visualization of the returned air to improve understanding of the occurring air flow phenomena. To achieve this, a novel visualization method was developed and applied to the STJ.

By adding carbon dioxide to the return air flow it becomes active in the infrared region. This return air can hence be visualized using an infrared camera. The developed method is therefore called Induced Infrared Thermography (IIT). It allows the visualization of the return air in front of the receiver. Due to the low signal to noise ratio advanced processing methods were necessary to isolate the wanted flow information. IIT was successfully applied to both examined receivers of the STJ. From the taken IIT images the upwards flow could clearly be visualized for the very first time.

A further novel method called Infrared Image Velocimetry (IRIV) was developed. Applying IRIV allows the deduction of the velocity of the examined air flows. For IRIV the occurring eddies are used as replacement for the particles used in Particle Image Velocimetry algorithms. IRIV is currently at a very early stage of development. The resulting IRIV vector fields are therefore treated as qualitatively flow visualizations. IRIV was successfully applied at the STJ, allowing the first comparison to a CFD simulation of four absorbers.





## 7 Outlook

To improve the open volumetric receiver concept, it is of vital importance to increase the ARR to reduce thermal losses. Therefore, the developed measurement techniques should henceforth be used in future to examine the influences of wind on the ARR.

The results should allow estimations on the influence of wind for a given tower height on the ARR. This is necessary to provide good estimations of annual efficiencies for potential power plant locations. Future optimizations of the STJ should be investigated in regard to the ARR. To improve the usability and to allow live monitoring, the tracer gas method should be integrated into the process control system of the STJ. Ideally the ARR measurement would be applicable for varying air mass flows.

To expand our knowledge about the flow field in front of the receiver, the developed IIT and IRIV measurement methods should be applied for a higher return air temperature. The infrared camera should be moved closer to the receiver to reduce absorption of the emitted signal in the atmosphere. Higher carbon dioxide concentrations would further improve the signal to noise ratio.



## Bibliography

- Nils Ahlbrink, Joel Andersson, Moritz Diehl, and Robert Pitz-Paal. Optimization of the Mass Flow Rate Distribution of an Open Volumetric Air Receiver. *Journal of Solar Energy Engineering*, 135(4):041003, 2013. doi: 10.1115/1.4024245.
- Felix Andlauer. KAMs CSP Technology - an Economic and Highly Flexible Solution Designed for Full Market Integration, 8 2015. URL [http://www.ka-muenchen.de/fileadmin/Downloads\\_D/Broschueren/CSP\\_brochure\\_Web.pdf](http://www.ka-muenchen.de/fileadmin/Downloads_D/Broschueren/CSP_brochure_Web.pdf).
- Antonio L Ávila-Marín. Volumetric receivers in solar thermal power plants with central receiver system technology: a review. *Solar Energy*, 85(5):891–910, 2011. URL <http://www.sciencedirect.com/science/article/pii/S0038092X11000302>.
- Alan C Bovik. *Handbook of image and video processing*. Academic press, 2010.
- Stefan Braemer. Experimentelle Untersuchungen mit einer neuartigen Tracergas-Messtechnik zur Bestimmung der Rueckfuhrtrate bei offenen volumetrischen Receivern. Master’s thesis, Rheinische Fachhochschule Koeln, 2014.
- DRK Brownrigg. The weighted median filter. *Communications of the ACM*, 27(8): 807–818, 1984. doi: 10.1145/358198.358222.
- Antoni Buades, Bartomeu Coll, and Jean-Michel Morel. A non-local algorithm for image denoising. In *Computer Vision and Pattern Recognition, 2005. CVPR 2005. IEEE Computer Society Conference on*, volume 2, pages 60–65. IEEE, 2005. doi: 10.1109/CVPR.2005.38.
- Gabriele Centi, Elsje Alessandra Quadrelli, and Siglinda Perathoner. Catalysis for CO<sub>2</sub> conversion: a key technology for rapid introduction of renewable energy in the value

chain of chemical industries. *Energy & Environmental Science*, 6(6):1711–1731, 2013. doi: 10.1039/C3EE00056G.

Shuqing Cui, Michaël Cohen, Pascal Stabat, and Dominique Marchio. CO<sub>2</sub> tracer gas concentration decay method for measuring air change rate. *Building and Environment*, 84:162–169, 2015. URL <http://www.sciencedirect.com/science/article/pii/S0360132314003606>.

Edward Lansing Cussler. *Diffusion: mass transfer in fluid systems*. Cambridge university press, 2009.

Kostadin Dabov, Alessandro Foi, Vladimir Katkovnik, and Karen Egiazarian. Image denoising by sparse 3-D transform-domain collaborative filtering. *Image Processing, IEEE Transactions on*, 16(8):2080–2095, 2007. doi: 10.1109/TIP.2007.901238.

Bureau International des Poids et Mesures, Commission électrotechnique internationale, and Organisation internationale de normalisation. *Guide to the Expression of Uncertainty in Measurement*. International Organization for Standardization, 1995. URL [http://www.iso.org/iso/home/store/catalogue\\_ics/catalogue\\_detail\\_ics.htm?csnumber=50461](http://www.iso.org/iso/home/store/catalogue_ics/catalogue_detail_ics.htm?csnumber=50461).

David L Donoho and Jain M Johnstone. Ideal spatial adaptation by wavelet shrinkage. *Biometrika*, 81(3):425–455, 1994. doi: doi:10.1093/biomet/81.3.425.

Berit Erlach, Benedikt Lunz, and Matthias Merzkirch. *Mit Energieszenarien gut beraten*. Deutsche Akademie der Technikwissenschaften e. V., 2015. URL [http://www.leopoldina.org/nc/de/publikationen/detailansicht/?publication\[publication\]=737](http://www.leopoldina.org/nc/de/publikationen/detailansicht/?publication[publication]=737).

Gereon Feckler, Thomas Fend, and Olena Smirnova. MetRec - Hocheffektive metallische Luftrezeiver fuer die Solare Turmtechnologie. In *18. Koelner Sonnenkolloquium*, 2015.

Piers Forster, Venkatachalam Ramaswamy, Paulo Artaxo, Terje Berntsen, Richard Betts, David W Fahey, James Haywood, Judith Lean, David C Lowe, Gunnar Myhre, et al. Changes in atmospheric constituents and in radiative forcing. Chapter 2. In *Climate Change 2007. The Physical Science Basis*. Teruyuki Nakajima, Veerabhadran

- Ramanathan, 2007. URL <http://www.ipcc.ch/pdf/assessment-report/ar4/wg1/ar4-wg1-chapter2.pdf>.
- Karl-Heinz Funken. The Juelich Solar Power Tower, 2013. URL [http://www.dlr.de/sf/en/Portaldata/73/Resources/dokumente/grossanlagen/juelich/Juelich\\_Solar\\_Power\\_Tower-EN.pdf](http://www.dlr.de/sf/en/Portaldata/73/Resources/dokumente/grossanlagen/juelich/Juelich_Solar_Power_Tower-EN.pdf).
- CJ Ghazi and JS Marshall. A CO<sub>2</sub> tracer-gas method for local air leakage detection and characterization. *Flow Measurement and Instrumentation*, 38:72–81, 2014. doi: 10.1016/j.flowmeasinst.2014.05.015.
- F Göhring, K Hennecke, B Hoffschmidt, M Schmitz, and P Schwarzbözl. 500kW-Forschungsplattform im Solarturm Jülich für Experimente mit hochkonzentrierter Solarstrahlung. In *12. Sonnenkolloquium: Qualifizierung solarthermischer Kraftwerke*, 2009. URL [http://elib.dlr.de/68859/1/4\\_G%C3%B6hring-Hennecke.pdf](http://elib.dlr.de/68859/1/4_G%C3%B6hring-Hennecke.pdf).
- P Goldsworthy, N Bignell, M Mason, M McCarthy, H Rogers, et al. The measurement of large ducted gas flows. In *Chemeca 90: The Eighteenth Australasian Chemical Engineering Conference; Processing Pacific Resources*, page 312. Chemical Engineering Group (New Zealand), 1990.
- DN Gordge and RH Page. Infrared imagery of an air/CO<sub>2</sub> axisymmetric jet. *Experiments in fluids*, 14(6):409–415, 1993. doi: 10.1007/BF00190195.
- David Griggs, Mark Stafford-Smith, Owen Gaffney, Johan Rockström, Marcus C Öhman, Priya Shyamsundar, Will Steffen, Gisbert Glaser, Norichika Kanie, and Ian Noble. Policy: Sustainable development goals for people and planet. *Nature*, 495(7441): 305–307, 2013. doi: 10.1038/495305a.
- Bernhard Hoffschmidt, Felix M Tellez, Antonio Valverde, Jesús Fernández, and Valerio Fernández. Performance evaluation of the 200-kWth HiTRec-II open volumetric air receiver. *Journal of Solar Energy Engineering*, 125(1):87–94, 2003. doi: 10.1115/1.1530627.
- ISO12569. Thermal performance of buildings and materials – Determination of specific airflow rate in buildings – Tracer gas dilution method. *International Organization for Standardization*, 2012. URL <https://www.iso.org/obp/ui/#iso:std:iso:12569>.

- Dennis R Jonassen, Gary S Settles, and Michael D Tronosky. Schlieren PIV for turbulent flows. *Optics and Lasers in Engineering*, 44(3):190–207, 2006. doi: 10.1016/j.optlaseng.2005.04.004.
- Les Kirkup and Robert B Frenkel. *An Introduction to Uncertainty in Measurement: Using the GUM (Guide to the Expression of Uncertainty in Measurement)*. Cambridge University Press, 2006.
- D Koch. SF6 properties, and use in MV and HV switchgear. *Cahier technique*, 2003.
- Gerrit Koll, Peter Schwarzboezl, Klaus Hennecke, Thomas Hartz, Mark Schmitz, and Bernhard Hoffschmidt. The Solar Tower Juelich-a research and demonstration plant for central receiver systems. *Proceedings SolarPACES*, 2009. URL <http://elib.dlr.de/60306/>.
- Jong-Sen Lee. Digital image smoothing and the sigma filter. *Computer Vision, Graphics, and Image Processing*, 24(2):255–269, 1983. doi: Digitalimagesmoothingandthesigmafilter.
- Mathieu Lepot, Adrien Momplot, Gislain Lipeme Kouyi, and Jean-Luc Bertrand-Krajewski. Rhodamine WT tracer experiments to check flow measurements in sewers. *Flow Measurement and Instrumentation*, 40:28–38, 2014.
- Daniel Maldonado Quinto. *Konvektive Verluste an offenen volumetrischen Solarstrahlungsempfaengern*. PhD thesis, RWTH Aachen University, 2016.
- V Narayanan, RH Page, and J Seyed-Yagoobi. Visualization of air flow using infrared thermography. *Experiments in fluids*, 34(2):275–284, 2003. doi: 10.1007/s00348-002-0557-x.
- Pietro Perona and Jitendra Malik. Scale-space and edge detection using anisotropic diffusion. *Pattern Analysis and Machine Intelligence, IEEE Transactions on*, 12(7): 629–639, 1990. doi: 10.1109/34.56205.
- David Pimentel, Alison Marklein, Megan A Toth, Marissa Karpoff, Gillian S Paul, Robert McCormack, Joanna Kyriazis, and Tim Krueger. Biofuel impacts on world food supply: use of fossil fuel, land and water resources. *Energies*, 1(2):41–78, 2008. doi: doi:10.3390/en1010041.

- Markus Raffel. Background-oriented schlieren (BOS) techniques. *Experiments in Fluids*, 56(3):1–17, 2015. doi: 10.1007/s00348-015-1927-5.
- Ali M Reza. Realization of the contrast limited adaptive histogram equalization (CLAHE) for real-time image enhancement. *Journal of VLSI signal processing systems for signal, image and video technology*, 38(1):35–44, 2004. doi: 10.1023/B:VLSI.0000028532.53893.82.
- William Hadley Richardson. Bayesian-Based Iterative Method of Image Restoration. *JOSA*, 62(1):55–59, 1972. doi: 10.1364/JOSA.62.000055.
- Jeremy Rifkin. The zero marginal cost society. *J. Rifkin, The Zero Marginal Cost Society*, page 356, 2014. URL <http://worldsustainabilityfund.nl/me/do/The%20Global%20Agenda%20Shift.pdf>.
- Kai Risthaus. Visualisierung der Rueckfuehrung bei offenen volumetrischen Receivern. Master’s thesis, RWTH Aachen University, 2015.
- Paul Robinson, Philipp Latzin, Sylvia Verbanck, Graham L Hall, Alexander Horsley, Monika Gappa, Cindy Thamrin, Hubertus GM Arets, Paul Aurora, S Fuchs, et al. Consensus statement for inert gas washout measurement using multiple and single breath tests. *European Respiratory Journal*, pages erj00697–2012, 2013. URL <http://www.ncbi.nlm.nih.gov/pubmed/23397305>.
- Manuel Romero and Aldo Steinfeld. Concentrating solar thermal power and thermochemical fuels. *Energy & Environmental Science*, 5(11):9234–9245, 2012. URL <http://dx.doi.org/10.1039/C2EE21275G>.
- Tobias Samus, Bastian Lang, and Holger Rohn. Assessing the natural resource use and the resource efficiency potential of the Desertec concept. *Solar Energy*, 87:176–183, 2013. doi: doi:10.1016/j.solener.2012.10.011.
- Ling Shao, Ruomei Yan, Xuelong Li, and Yan Liu. From heuristic optimization to dictionary learning: a review and comprehensive comparison of image denoising algorithms. *Cybernetics, IEEE Transactions on*, 44(7):1001–1013, 2014. doi: 10.1109/TCYB.2013.2278548.

- JW Tang, CJ Noakes, PV Nielsen, I Eames, A Nicolle, Y Li, and GS Settles. Observing and quantifying airflows in the infection control of aerosol- and airborne-transmitted diseases: an overview of approaches. *Journal of Hospital Infection*, 77(3):213–222, 2011. URL <http://www.ncbi.nlm.nih.gov/pubmed/21194796>.
- F Téllez, M. Romero, P. Heller, A. Valverde, J.F. Reche, S. Ulmer, and G Dibowski. Thermal Performance of “SolAir 3000 kWth” Ceramic Volumetric Solar Receiver. *12th International Symposium Solar Power and Chemical Energy Systems*, 2004. doi:10.1016/j.solener.2011.02.002.
- William Thielicke and Eize J Stamhuis. PIVlab—Towards user-friendly, affordable and accurate digital particle image velocimetry in MATLAB. *Journal of Open Research Software*, 2(1):e30, 2014. doi: <http://doi.org/10.5334/jors.bl>.
- A. Tiddens, D. Maldonado Quinto, and B Hoffschmidt. Receiver für Solarenergiegewinnungsanlagen. Patent pending - 10 2016 203 102.3, Februar 2016a.
- Arne Tiddens and Marc Röger. IR-basierte Geschwindigkeitsfeldbestimmung. Patent pending - 102015201337.5, 10 2015. Nationality German.
- Arne Tiddens, Marc Röger, Hannes Stadler, and Bernhard Hoffschmidt. A tracer gas leak rate measurement method for circular air circuits. *Flow Measurement and Instrumentation*, 47:45–53, 2016b.
- Arne Tiddens, Kai Risthaus, Marc Röger, Hannes Stadler, and Bernhard Hoffschmidt. Induced Infrared Thermography: Flow visualizations under the extreme conditions of an open volumetric receiver of a solar tower. *International Journal of Heat and Fluid Flow*, 65:105–113, Jun 2017a. ISSN 0142-727X. doi: 10.1016/j.ijheatfluidflow.2017.04.002. URL <http://dx.doi.org/10.1016/j.ijheatfluidflow.2017.04.002>.
- Arne Tiddens, Marc Röger, Hannes Stadler, and Bernhard Hoffschmidt. Air return ratio measurements at the solar tower Jülich using a tracer gas method. *Solar Energy*, 146:351–358, Apr 2017b. ISSN 0038-092X. doi: 10.1016/j.solener.2017.02.027. URL <http://dx.doi.org/10.1016/j.solener.2017.02.027>.
- Werner Vogel and Henry Kalb. *Large-scale solar thermal power: technologies, costs and development*. John Wiley & Sons, 2010.



- 
- Henrik von Storch, Hannes Stadler, Martin Roeb, and Bernhard Hoffschmidt. Efficiency potential of indirectly heated solar reforming with open volumetric solar receiver. *Applied Thermal Engineering*, 2015. ISSN 1359-4311. URL <http://dx.doi.org/10.1016/j.applthermaleng.2015.05.026>.
- Theo Wember. Technische Statistik und statistische Versuchsplanung, 2008.
- Hong Yang, Yuan Zhou, and Junguo Liu. Land and water requirements of biofuel and implications for food supply and the environment in China. *Energy Policy*, 37(5): 1876–1885, 2009. doi: [doi:10.1016/j.enpol.2009.01.035](https://doi.org/10.1016/j.enpol.2009.01.035).
- Howard W Yoon, Meredith H Brenner, Joseph P Rice, Nathaniel R Briggs, and Greg Gillen. Flow visualization of heated CO<sub>2</sub> gas using thermal imaging. In *Defense and Security Symposium*, pages 62050U–62050U. International Society for Optics and Photonics, 2006. doi: <http://dx.doi.org/10.1117/12.664991>.



## Acknowledgment

This work was carried out with financial support from the Ministry of Innovation, Science and Research of the State of North Rhine-Westphalia (MIWF NRW), Germany under contract 323-2010-006 (Start-SF).

My gratitude lies with Univ.-Prof. Dr.-Ing. Bernhard Hoffschmidt for supervising my work and taking great personal interest in my experiments. I am especially grateful to his contagious enthusiasm.

I furthermore honor the highly scientific contributions of Univ.-Prof. Dr.-Ing. Robert Pitz-Paal who supervised this work during the first year. I highly appreciate that he continued his support until the end of my thesis.

I would furthermore like to thank Univ.-Prof. Dr. rer. nat. Andreas Kemna for acting as the second examiner.

My utmost thanks goes to Dr.-Ing. Marc Röger for the extraordinary motivating support throughout my thesis. I am grateful for the countless innovative discussions as well as his encouragement. I could not have had a better supervisor and mentor!

I am very thankful for the scientific discourse with Dr.-Ing. Hannes Stadler, for his continuous support as well as for his constructive criticism which improved the work considerably. Debating with him was a pleasure.

I would furthermore like to thank my students Lukas Schenke, Matthias Offergeld, Stefan Brämer and Kai Risthaus. They all helped to move this thesis forward and were great sparing partners.

Many thanks go to all PhD students, especially to Daniel, Henrik, Friedemann, Jan, Matthias, Raffaele, Robert and Silvan. They provided such a welcoming and excellent atmosphere which reached beyond the workplace. A special thanks goes to Matthias. I

would like to thank him for his extensive corrections of this thesis. I am particularly grateful for sharing an office with him.

I am deeply grateful to my mother for infusing me with the power of strategic thinking and inner calm. I would further like to thank my father for infecting me with the love of experimenting and creativity. Paired with continuously love and support, these make up the foundation of my scientific work. Dear Brothers, we are... "so". I am incredibly grateful for this.

I am grateful to my wife Maria José Fabregat Salvador from the bottom of my heart. She is the most impressive person I can image. I am incredibly thankful for her love and support.

## Nomenclature

Term	Description	Units
$A$	amplitude	
$ARR$	substantial air return ratio	%
$ARR_{fit}$	air return ratio determined from fit	%
$ARR_{meas,dyn}$	measured air return ratio with dynamic method	%
$ARR_{meas,num}$	measured air return ratio with numeric method	%
$ARR_{meas,stat}$	measured air return ratio with static method	%
$ARR_{part}$	air return ratio of the air flow which is not separated	%
$ARR_{peri}$	air return ratio resulting from peripheral leakage	%
$ARR_{thermal}$	thermal air return ratio	%
$ARR_{true}$	air return ratio assuming an ideal transfer function	%
$b$	background of an infrared image	
$cor_{dyn}$	correction due to non ideal transfer function	
$cor_{peri}$	correction due to peripheral leakage	
$G$	transfer function	
$g$	infrared image	
$h$	specific enthalpy of the sucked in air	J/kg
$\mathcal{L}$	Laplace transform	
$M$	molar mass	kg/mol
$\dot{m}$	air mass flow which is sucked in	kg/s
$M_{out}$	molar mass of blow out air	kg/mol
$M_{return}$	molar mass of return air	kg/mol
$\dot{n}$	molar mass flow	mol/s
$n$	noise of an infrared image	
$\dot{n}_{amb}$	molar mass flow which is sucked in from the ambient	mol/s
$\dot{n}_{He,inj}$	molar mass flow of helium which is injected	mol/s
$\dot{n}_{in}$	molar mass flow which is sucked in	mol/s
$\dot{n}_{lost}$	molar mass flow which is lost	mol/s
$\dot{n}_{out}$	molar mass flow which is blown out	mol/s
$n_{pixel}$	number of pixel	

<b>Term</b>	<b>Description</b>	<b>Units</b>
$\dot{n}_{\text{return}}$	molar mass flow which is returned	mol/s
$O$	higher order terms	
$o$	offset of an infrared image	
$\Psi$	percentage of the air which is returned to the receiver	
$s$	complex number frequency	
$T$	temperature	°C
$T_{\text{amb}}$	ambient temperature	°C
$T_{\text{circ}}$	circulation period	s
$T_{\text{in,rec}}$	temperature of the sucked in air at the receiver front	°C
$T_{\text{out,rec}}$	temperature of the blow out air at the receiver front	°C
$T_{1,2}$	fitting parameter of transfer function	s
$\chi_{\text{He}}$	helium mole fraction	
$\chi_{\text{He,amb}}$	helium mole fraction of the ambient air	
$\chi_{\text{He,const}}$	constant helium mole fraction	
$\chi_{\text{He,fit,leading}}$	helium mole fraction of the applied fit of the leading edge	
$\chi_{\text{He,fit,trailing}}$	helium mole fraction of the applied fit of the trailing edge	
$\chi_{\text{He,in}}$	helium mole fraction of the sucked in air	
$\chi_{\text{He,inj}}$	helium mole fraction of the injection	
$\chi_{\text{He,meas}}$	measured helium mole fraction	
$\chi_{\text{He,meas,ARR}=0}$	measured helium mole fraction of a measurement with an ARR=0	
$\chi_{\text{He,meas,leading}}$	measured helium mole fraction of the leading edge	
$\chi_{\text{He,out}}$	helium mole fraction of the blown out air	
$\chi_{\text{He,return}}$	helium mole fraction of the returned air	
$\chi_{\text{He,step}}$	helium mole fraction response to a step function	
$\chi_{\text{He,step,norm}}$	normalized helium mole fraction response to a step function	
$\chi_{\text{He,true}}$	helium mole fraction without the distortion due to a non ideal transfer function	
$\chi_{\text{He,true,leading}}$	helium mole fraction without the distortion due to a non ideal transfer function of the leading edge	

## Acronyms

ARR	air return ratio.
BM3D	block matching 3 dimensional.
CO <sub>2</sub>	carbon dioxide.
DLR	German aerospace center.
He	helium.
IIT	induced infrared thermography.
IR	infra red.
IRIV	infrared image velocimetry.
MS	mass spectrometer.
NRMSD	normalized root-mean-squared deviation.
PIV	particle image velocimetry.
ROI	region of interest.
SF <sub>6</sub>	sulfur hexafluoride.
STJ	solar tower Juelich.





## List of Figures

1.1	Schematic of the STJ. The receiver is heated by a field of heliostats. Air is sucked through the receiver, heating up to about $680^{\circ}\text{C}$ and used to drive a water steam cycle or is stored in a thermal storage. The still warm air ( $< 300^{\circ}\text{C}$ ) is returned to the receiver for efficiency purposes. Based on Funken (2013).	2
1.2	Photos of the receiver of the solar tower Juelich, showing its modularity. (a) shows a close up of the absorber structure of the Hitrec-II absorber module, (b) individual absorber modules during maintenance which make up the main receiver of the solar tower Juelich (c). Based on Tiddens et al. (2017b).	3
1.3	A schematic of the air flow of the open volumetric receiver is shown. The air mass flows $\dot{m}$ and specific enthalpies $h$ are indicated. Based on Tiddens et al. (2016b).	4
1.4	The normalized system efficiency for different air return temperatures and ARRs is shown. It can be seen that an improvement from $ARR = 60\%$ to $ARR = 80\%$ leads to an increase in 8 percentage points of the normalized system efficiency. (Maldonado Quinto, 2016)	5
1.5	A schematic of the air flow within the open volumetric air receiver is shown. Based on Ahlbrink et al. (2013).	6
1.6	Measurements of the ARR at the SOLAIR 3000 receiver. Due to the heat flow between the return air and the outsides of the receiver modules (see Fig. 1.7), these measurements can only be seen as a rough estimate (see Eq. 1.4). (Télez et al., 2004)	7
1.7	A schematic of the air flow within the open volumetric air receiver is shown. The rate of flow of heat $\dot{Q}_{\text{abs},i}$ between the sucked in and blown out air is indicated. Based on Ahlbrink et al. (2013).	8

1.8	Simulated ARR of one absorber module for different percentages of the nominal mass flux. The simulated absorber module is irradiated and considered undisturbed by neighboring models and wind. The ARR decreases only very slightly with increasing mass flow of the system. Maldonado Quinto (2016) . . . . .	9
1.9	The simulated ARR for different percentages of partial air return $\Psi$ for one absorber module. The partial air return can be greater than one, since it is examined here on an absorber level. The simulations were conducted for one module. Based on Maldonado Quinto (2016). . . . .	10
1.10	The simulated air flow in front of four absorber modules is shown. The axis are hereby normalized by the absorber edge length $l$ . It can be observed, that for $x/l > 0.5$ the return air only moves further away from the receiver and upwards. The simulated ARR of the four modules was found to be 58 %, compared to the higher 63 % the for one absorber module. Based on Maldonado Quinto (2016). . . . .	11
2.1	Schematic diagram of the air circuit of open volumetric air receiver. Based on Tiddens et al. (2016b). . . . .	21
2.2	The theoretical helium mole fraction response of a circular air circuit with an $ARR = 0.6$ , ignoring the dispersion of helium in the system. Based on Tiddens et al. (2016b). . . . .	25
2.3	The theoretical helium mole fraction response of a circulation measurement of an air circuit with $ARR = 0.6$ , ignoring the dispersion of helium in the system. A circulation measurement can be seen in Fig. 4.4. . . . .	26
2.4	The correction due to diffusion of helium into the contact surface area is shown for a typical dynamic measurement. The measurement was conducted without irradiation with an air mass flow of $(9.96 \pm 0.04)$ kg/s. . . . .	27
2.5	The figure shows schematically the creation of a helium mole fraction step function at the inlet of the measuring probe. The indicated time corresponds to the time in Fig. 2.6. (Tiddens et al., 2016b) . . . . .	29
2.6	The figure shows an exemplary step response of the measurement setup compared to model responses of a $PT_1$ , $PT_2$ and $PT_3$ transmission element response. The normalized root-mean-square deviation (NRMSD) of the models are given. Based on Tiddens et al. (2016b). . . . .	30
2.7	The figure shows the general outline of the derivation measured mole fraction function $\chi_{\text{He,meas}}(t)$ . Whereby $\mathcal{L}$ is the Laplace transformation. . . . .	31

2.8	The measured mole fraction function $\chi_{\text{He, meas, leading}}(t)$ is plotted for $T_1 = 0.12$ s, $T_2 = 0.39$ s, $ARR_{\text{true}} = 0.6$ , $T_{\text{circ}} = 3$ s. The fit (Eq. 2.17) results in $ARR_{\text{fit}} = 0.6259$ and in $cor_{\text{dyn}} = 0.9586$ . . . . .	32
2.9	The figure shows the dynamic correction $cor_{\text{dyn}}$ at the receiver model for different circulation periods $T_{\text{circ}}$ and $ARR_{\text{fit}}$ for a fixed time constant of the transfer function $T_1 = 0.12$ s, $T_2 = 0.39$ s. . . . .	34
2.10	The dynamic correction $cor_{\text{dyn}}$ at the STJ is shown for different circulation periods $T_{\text{circ}}$ and measured $ARR_{\text{meas}}$ for a fixed time constant of the transfer function $T_1 = 0.42$ s, $T_2 = 0.19$ s. The scale of $cor_{\text{dyn}}$ is the same as in Fig. 2.9, for comparison. $ARR_{\text{meas}}$ and $T$ are chosen according to their occurrence at the STJ. . . . .	35
2.11	The helium mole fraction over time of a typical measurement is shown in the original irregular sampling frequency and compared to its resampled signal. . . . .	38
2.12	Transmission spectrum of the earth's atmosphere is shown. The spectral irradiance of a blackbody according to Planck's law is shown for three different temperatures. When examining concentrated solar radiation it can be seen that the sun's radiation dominates for all shown wavelengths when the transmission of the atmosphere is not close to zero. The region of interest (ROI) marks the carbon dioxide as well as the water vapor absorption band. Based on Tiddens et al. (2017a). . . . .	43
2.13	The effective spectral emissivity of carbon dioxide is shown for two different temperatures. The radiant flux is assumed to be emitted over a length of one meter by carbon dioxide at a mole fraction of 1500 ppm. It can be seen that the effective spectral emissivity peak is broader for higher temperatures. Based on Risthaus (2015). . . . .	44
2.14	Radiant flux emitted by carbon dioxide, received per unit solid angle, depending on the optical length, temperature and mole fraction of carbon dioxide. The radiant flux is assumed to be emitted over an optical path length of one meter, through a surface of one square meter. Based on Risthaus (2015). . . . .	46
2.15	The signal processing of the IIT is shown for a sample image of the Testreceiver at the STJ. The left image is the raw image. From it the background and offset is subtracted to yield the central image. The result of the noise removal can be seen on the right. The position of the viewing area of these IIT images is shown in Fig. 4.16. Based on Tiddens et al. (2017a). . . . .	52

2.16	An exemplary measured correlation matrix intensity (dots) is shown for one dimension, being fitted with Gaussian function (solid line). This is done for both axes independently, resulting in a peak location determination of sub pixel precision. Based on Thielicke and Stamhuis (2014) . . . . .	54
3.1	Photo of the measurement setup, showing: (1)helium, (2)mass flow controller, (3)mass spectrometer, (4)helium injection, (5)air mass flow meter, (6)receiver, (7)removable lid, (8)air return tubes, (9)measuring point 1, (10)fan, (11)measuring point 2. Based on Tiddens et al. (2016b). . . . .	56
3.2	Photo of the receiver model with a closed front and all 13 return tubes attached (Tiddens et al., 2016b). . . . .	57
3.3	Photo of one of the measuring probe used at the receiver model sampling the helium mole fraction at discrete points of the cross section of the piping to obtain the spatial distribution. . . . .	57
3.4	Photo of the STJ displaying the main receiver (1) at the top, the target for the calibration of heliostats (2), the Testreceiver (3) and the heliostats (4) at ground level. Based on Tiddens et al. (2017b). . . . .	58
3.5	The research platform of the STJ with the solar receiver (1), two gas measuring point (2,6), the gas cooler (3), the injection point (4) and the blower (5). . . . .	59
3.6	Photo of the research platform of the STJ from front and side perspective. Tiddens et al. (2017b) . . . . .	60
3.7	Schematic of the STJ. The receiver is heated by a field of heliostats. Air is sucked through the receiver, heating up to about 680 °C and used to drive a water steam cycle or is stored in a thermal storage. The still warm air (< 300 °C) is returned to the receiver for efficiency purposes. The location of the measuring points and helium injection for the tracergas method are indicated. Based on Funken (2013). . . . .	61
3.8	Photos of the main receiver of STJ from front and side perspective. The active absorber surface consists of 1080 absorber modules (1), surrounded by an irradiation shield (2). The modularity of the receiver can be seen in Fig. 1.2. At the sides and underneath the absorber there are outlets of the external air return system (3). Based on Tiddens et al. (2017b). . .	62

3.9	Schematic of the measurement probe of the measuring point 2 which incorporates the injection of helium. Showing the inner probe (1) which is held in place by the support structure (2,3). By moving the inner probe within the support structure, a sample can be extracted towards the mass spectrometer at discrete locations along the cross section of the piping of the STJ. Based on Tiddens et al. (2017b). . . . .	63
3.10	Schematic of the measuring point 2, with two measurement probes. The inner probes (1) are held in place by the support structure (2,3). By moving the inner probe within the support structure, a sample can be extracted towards the mass spectrometer at 15 discrete locations along the cross section of the piping of the STJ. The red probe (see Fig. 3.9) incorporates the injection of helium, which is facing downstream (blue arrow) to not influence the extracted probes. The designed probes furthermore contain mounts for the previously installed thermocouples (4). Based on Tiddens et al. (2017b). . . . .	64
3.11	Photo of the of the measuring point directly behind the receiver. The photo was taken from the inside of the piping at the STJ. The direction of air flow follows the line of sight. In the background the splitting towards emergency vent, storage and steam boiler (left to right) can be seen. . .	65
4.1	The helium mole fraction across the piping of the receiver model at measuring point 2 (see Fig. 3.1) is homogeneously distributed. The measurements show only small fluctuations with a standard deviation of 1.6 %. Based on Tiddens et al. (2016b). . . . .	68
4.2	The figure shows the normalized raw data of a helium injection of 50 std l/min for the static method with 8 of 13 attached air return tubes. Based on Tiddens et al. (2016b) . . . . .	70
4.3	The helium mole fraction across the piping of the STJ at measuring point 2, directly behind the receiver. The measurements show large fluctuations, with an standard deviation of 9.7 %. This inhibits single point measurements.	71
4.4	The helium mole fraction response due to the injection of two short helium peaks is shown. Each peak passes the measuring point four times, before the peaks become indistinguishable. The time between two peaks is the circulation period $T_{\text{circ}}$ , marked in red. Based on Tiddens et al. (2016b).	73
4.5	The helium mole fraction response due to the injection of three long helium peaks is shown. Based on Tiddens et al. (2016b). . . . .	74

- 
- 4.6 The ARR was measured using the static as well as the dynamic tracer gas measurement with a closed receiver configuration (see Fig. 3.2) for four different scenarios with a certain number of return tubes attached. The measurement was conducted with helium injection quantities of 25 std l/min and 50 std l/min. The uncertainties are presented with a 95 % level of confidence. Based on Tiddens et al. (2016b). . . . . 76
- 4.7 The normalized helium mole fraction is sampled along the cross section of the piping at measuring point 1 of the STJ. These measurements were performed with all return air being blown out through the vent, resulting in  $ARR = 0$ . The measurements show only minor fluctuations, with a standard deviation of 1.4 %. Based on Tiddens et al. (2017b). . . . . 78
- 4.8 A circulation period measurement at an air mass flow of  $\dot{m} = 5 \text{ kg/s}$ . A circulation period of  $T_{\text{circ}} = (52.5 \pm 2.5) \text{ s}$  was found by measuring the duration in between the peaks. Based on Tiddens et al. (2017b). . . . . 79
- 4.9 A circulation period measurement at an air mass flow of  $\dot{m} = 10 \text{ kg/s}$ . A circulation period of  $T_{\text{circ}} = (25.4 \pm 1.4) \text{ s}$  was found by measuring the duration in between the peaks. Based on Tiddens et al. (2017b). . . . . 79
- 4.10 Helium mole fraction over time is shown for a measurement using the dynamic method. The measurement was conducted without irradiation with an air mass flow of  $(9.96 \pm 0.04) \text{ kg/s}$ . Based on Tiddens et al. (2017b). 80
- 4.11 The helium mole fraction over time is shown for a measurement using the dynamic method. The measurement was conducted with an air mass flow of  $(4.96 \pm 0.07) \text{ kg/s}$  at an irradiated receiver. Large deviations from the fit within the time of measurement can be observed. Based on Tiddens et al. (2017b). . . . . 83
- 4.12 The helium mole fraction over time is shown for a measurement with an  $ARR = 0$ , achieved by blowing all return air through a vent instead of the receiver. The shown mole fraction data has been corrected for the diffusion of the helium  $\chi_{\text{He,diff}}$  according to Section 2.1.3. . . . . 84
- 4.13 Helium mole fraction and ARR over time are shown for a measurement using the numeric method. The average  $ARR_{\text{meas,num}}$  is found to be  $ARR_{\text{meas,dyn}} = (67.6 \pm 0.4) \%$  compared with the result of the dynamic method  $(67.7 \pm 0.5) \%$ . The measurement was conducted without irradiation with an air mass flow of  $(9.96 \pm 0.036) \text{ kg/s}$  (same data as used in Fig. 4.10). . . . . 85

- 4.14 Helium mole fraction and ARR over time is shown for a measurement using the numeric measurement. When regarding only the indicated central part, the average  $ARR_{\text{meas,num}}$  is found to be  $(54.32 \pm 9.1) \%$  compared with the result of the analytical method  $ARR_{\text{meas,dyn}} = (56.3 \pm 1.0) \%$ . The measurement was conducted without irradiation with an air mass flow of  $(4.96 \pm 0.07) \text{ kg/s}$  (same data as: Fig. 4.11). . . . . 86
- 4.15  $ARR_{\text{meas,num}}$ , azimuth wind speed  $v_{\phi,wind}$ , wind direction  $\phi_{wind}$  and elevation wind speed  $v_{wind,elev}$  are shown (same data as: Fig. 4.14). A negative  $v_{wind,elev}$  indicated a downwards wind,  $\phi_{wind} = 0$  indicates a wind from the north. No apparent correlation between  $ARR_{\text{meas,num}}$  and the other parameters can be observed. . . . . 87
- 4.16 A sectional CAD view of the Testreceiver is shown. The air flow as well as the position of the viewing area of the IIT images is indicated. Based on Tiddens et al. (2017a). . . . . 88
- 4.17 A typical sequence of four successive images has been taken at the research platform. It can be seen that the air flow moves upwards from image (a) to (d). Based on Risthaus (2015) . . . . . 89
- 4.18 Two IIT images showing an atypical flow are displayed. The return air is taken further away from the receiver in (a) and the direction of the flow is reversed in (b). (Risthaus, 2015) . . . . . 90
- 4.19 The vector field indicating the flow is superimposed on the average of the sequence's images. The examined sequence consists of 100 IIT images with a total duration of 4.5 seconds. Since this is the first application of IRIV and the first flow measurement at the Testreceiver, it should be treated as a qualitative measurement only. Based on Tiddens et al. (2017a). 91
- 4.20 A photo of the STJ from the perspective of the infrared camera. The section of the image seen by the infrared camera is indicated. . . . . 92
- 4.21 A typical sequence of four successive images taken at the main receiver is shown. It can be seen that the air flow moves upwards from image (a) to image (d). Based on Risthaus (2015). . . . . 93
- 4.22 The vector field indicating the flow is superimposed on the average image of the sequence of the main receiver of the STJ. The examined sequence consists of 100 IIT images of a total duration of 1.9 s seconds. Since this is the first application of IRIV and the first flow measurement at the main receiver, it should be treated as a qualitative measurement only. The conventional air return mechanism was used and an  $ARR_{\text{meas,dyn}} = (58.0 \pm 1.2) \%$  has been measured. Based on Tiddens et al. (2017a). . . 94

- 5.1 Helium mole fraction data around the time of the IIT (see Fig. 4.18 (a)). The anomaly was detected in front of the receiver at 15:21:52, corresponding to the helium mole fraction at around 15:22:30. . . . . 99
- 6.1 Helium mole fraction and ARR over time are shown for a measurement using the numeric method. The average ARR is found to be  $(67.6 \pm 0.4)\%$  compared with the result of the dynamic method  $(67.7 \pm 0.5)\%$ . The measurement was conducted without irradiation of the receiver. (same data as: Fig. 4.13) . . . . . 104